博士論文

Rheological studies on aqueous nanocellulose dispersions

（水系ナノセルロース分散液のレオロジー解析）

田仲　玲奈

Reina Tanaka

Table of Contents

Copyrights

1) Chapter 2

2) Chapter 3

Chapter 1

General Introduction

1.1. Cellulose

1.1.1. Cellulose

Cellulose is the most abundant polymer on earth. The estimated production of cellulose is ~7.5×10^{10} tonnes per year.[1] The main resources of cellulose to be used in our lives are produced from plant cell walls such as those of trees and cotton. These plant celluloses are isolated as pulp fibers after pulping and bleaching, and have been traditionally used as raw materials for paper, board and clothes. In recent years, cellulose has been also utilized as fibers, films, medical products, cosmetics, food additives, dialysis membranes, and liquid-crystal display panels via chemical modification and dissolution–regeneration processes.[2,3] Other resources of cellulose are bacteria, algae, fungi, and tunicates.[1]

The chemical structure of cellulose is shown in Figure 1.1. Cellulose is a linear homopolymer consisting of β-1,4-linked $_D$-glucopyranose units. The hydrophobic CH groups and hydrophilic OH groups of cellulose are positioned in the axial and equatorial directions, respectively.[2] In plant cell walls, dozens of extended and uniaxially-aligned cellulose chains are assembled by hydrogen bonds and van der Waals forces,[4,5] forming fibrillary crystallites with widths of 3–5 nm and lengths of 1–5 μm, called cellulose microfibrils.[5,6] Cellulose microfibrils have the crystal structure of cellulose I,[7–9] and have high aspect ratios (the ratios of length to width) of over 300, high crystal moduli of 110–150 GPa,[10–13] high strength of 2–3 GPa,[14] and low thermal expansion coefficients of 0–6 ppm K^{-1}.[13,15]

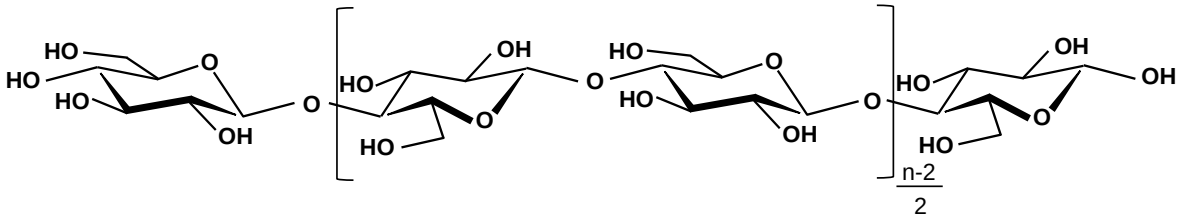

Figure 1.1. Chemical structure of cellulose. The *n* is the degree of polymerization.

1.1.2. Wood cellulose

In the primary cell walls, or the most outer layers of wood cell walls (thickness: ~0.1 μm), about 3 nm-wide cellulose microfibrils (30%) are embedded in matrix polysaccharides composed mainly of hemicelluloses (30%) and pectins (35%).[5,6] Hemicelluloses have heterogeneous chemical structures of β-1,4-linked backbones, and have relatively low molecular weights and low crystallites.[6] Pectins are complex polysaccharides including α-1,4-linked $_D$-polygalacturonic acid units.[16] The matrix polysaccharides are partly bound to the surfaces of cellulose microfibrils, and help to prevent microfibril aggregation in the cell wall, making the primary cell walls flexible.[6,17,18] The crystalline cellulose microfibrils surrounded by these matrix polysaccharides are regarded as native "core–shell" structures.[17, 19−24]

The secondary cell walls are composed of 50% cellulose, 20–30% hemicelluloses, and 30–20% lignin. [3] Lignin is a hydrophobic polymer consisting of phenylpropanoids, and act as a binder within or between the cell walls.[25] Cellulose microfibrils are hierarchically deposited in the secondary cell walls, and form three distinct layers, namely the S_1, S_2, and S_3 layers (from the outside to inside) (Figure 1.2).[25] Cellulose microfibrils in the S_1 and S_3 layers are oriented in the direction at angle 50–90 º to the cell axis, and those in the S_2 layer are almost parallel to the cell axis (5–30 º). The S_2 layer (thickness: ~2 μm) is much thicker than the other two layers (0.1–0.3 μm) and constitutes ~80% v/v of the cell walls. Therefore, the mechanical properties of the cell walls are dominated by the S_2 layer.

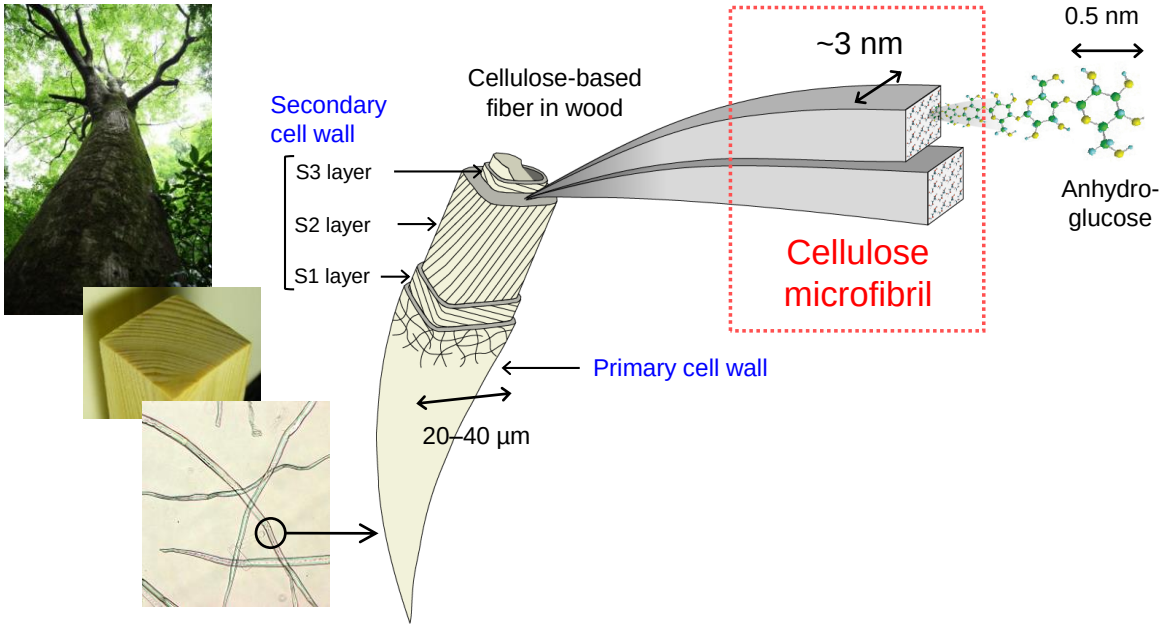

Figure 1.2. The hierarchical structure of wood cellulose.

1.2. Nanocellulose

1.2.1. Nanocrystalline celluloses (NCCs)

Nanocrystalline celluloses (NCCs) are rod-like cellulose nanoparticles with low aspect ratios, and prepared from native celluloses by acid hydrolysis with concentrated sulfuric or hydrochloric acid (Figure 1.3).[26–29] NCCs are also referred to as cellulose nanowhiskers (CNWs), cellulose nanocrystals (CNCs), and cellulose nanocrystallites.[27,30] Rånby and Ribi first reported the preparation of NCCs from wood and cotton celluloses by sulfuric acid hydrolysis.[31] The obtained NCCs had 5–10 nm in width and 50–60 nm in length. When native celluloses are hydrolyzed, the disordered regions of celluloses are preferentially hydrolyzed. In contrast, their crystalline regions show a high acid resistance and can remain as a solid residue even after hydrolysis. The degree of polymerization (DP) of the cellulose samples drastically decreases to 200–300 at the initial stage of acid hydrolysis and then reaches a plateau, namely the leveling-off degree of polymerization (LODP). When sulfuric acid is used in hydrolysis, anionic sulfate ester groups are randomly introduced on the surface of the NCC particles. Because of the surface negative charges, the obtained NCCs are well dispersed in water.[32] These NCC suspensions are characterized by formation of a

chiral nematic order in anisotropic liquid crystalline phases.[33] On the other hand, NCCs prepared in hydrochloric acid are less charged and thus easy to agglomerate in water.[34,35]

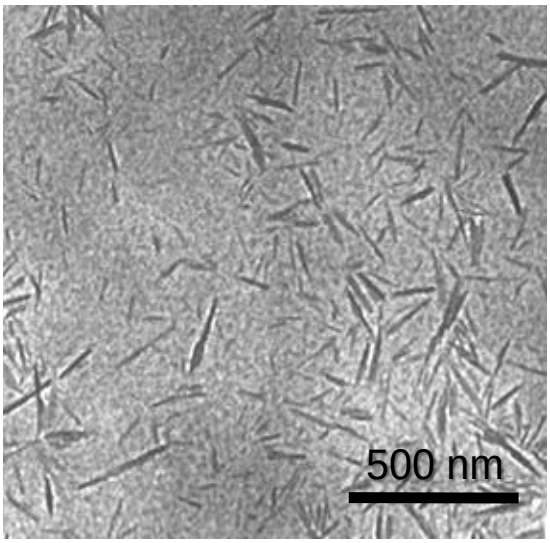

Figure 1.3. Transmission electron microscope (TEM) image of wood-derived NCC paticles.

1.2.2. Nanofibrillated celluloses (NFC)

Microfibrillated celluloses (MFCs) with high aspect ratios are prepared from native celluloses solely by harsh mechanical treatment in water.[36,37] Turbak et al. first reported the mechanical disintegration method of wood celluloses to prepare MFCs (Figure 1.4a).[38] When wood celluloses are subjected to mechanical treatments in water using high-pressure homogenizers[38–40] or a grinder,[41–43] MFCs with widths of 10–2000 nm and lengths of a few micrometers, consisting of microfibril bundles, are obtained.[44,45] The obtained MFCs have some unique characteristics such as high viscosity in suspensions,[38,39] and high mechanical strength as dried materials.[46,47] However, high energy consumption is required in the harsh mechanical treatment, which is a drawback when promoting the utilization of MFCs at the industrial level.[1,36,48]

Recently, pretreatments of wood celluloses such as enzymatic hydrolysis,[49,50] carboxymethylation,[51,52] acetylation,[53,54] and oxidation[44] have been reported as energy-efficient pretreatments to produce MFCs with much thinner widths of 3–60 nm, or so-called nanofibrillated celluloses (NFCs) (Figure 1.4b and

c).[36,48] The energy consumption in the NFC production can be reduced from 12000–70000 to 500 kWh t^{-1} in combination with such pretreatments.[48] In particular, a catalytic oxidation using 2,2,6,6-tetramethylpiperidine-1-oxyl (TEMPO) has attracted attention as a unique method to prepare NFCs consisting of individualized 3nm-wide microfibrils in high yields with high-energy efficiency.[44]

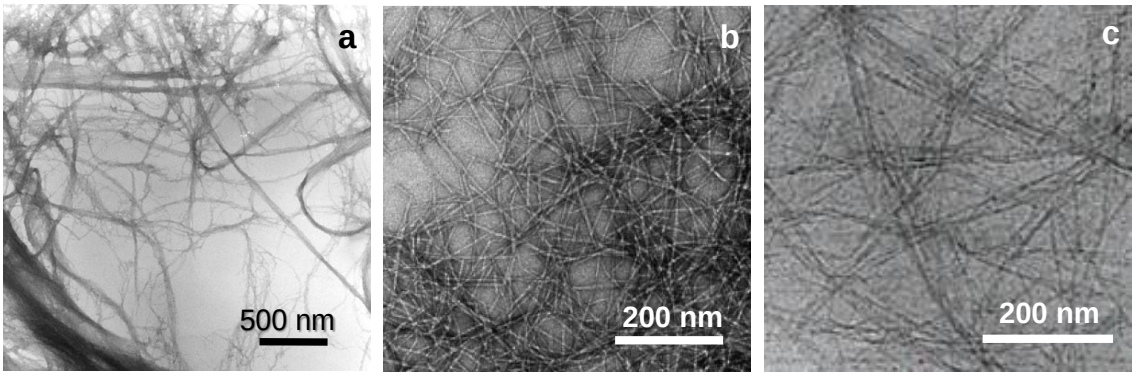

Figure 1.4. TEM images of (a) MFCs, (b) partially carboxymathlated NFCs,[51] and (c) enzymatically-prehydrolyzed NFCs.[49]

1.2.3. TEMPO-mediated oxidation as a pretreatment for NFC production

When native celluloses are subjected to TEMPO-mediated oxidation in water, the C6 primary hydroxyl groups exposed on the microfibril surfaces are resioselectively converted to carboxylate groups.[44,55] The fiber morphologies and crystal structures of the TEMPO-oxidized celluloses are almost similar to those of the original celluloses even after the oxidation. Since the surface carboxylate groups are dissociated in water, electric double layer repulsion is produced between the surface-carboxylated microfibrils. Completely isolated NFCs, or TEMPO-oxidized cellulose nanofibrils (TOCNs), are thus prepared by mild mechanical treatment in water. TOCNs prepared from wood celluloses have a uniform width of ~3 nm and long lengths of > 500 nm.

The TEMPO/NaBr/NaClO system under alkaline conditions (Figure 1.5) is a commonly used as the TEMPO-oxidation reaction.[55,56] However, in this system, remarkable depolymerization of celluloses during the oxidation at pH 9–11 is inevitable due to the following two reasons:[57–59] (1) β-elimination of

glycoside bonds at the C6-aldehyde groups produced as intermediates during the oxidation;[60] (2) attacking the glycoside bonds by active radical species formed in situ.[61]

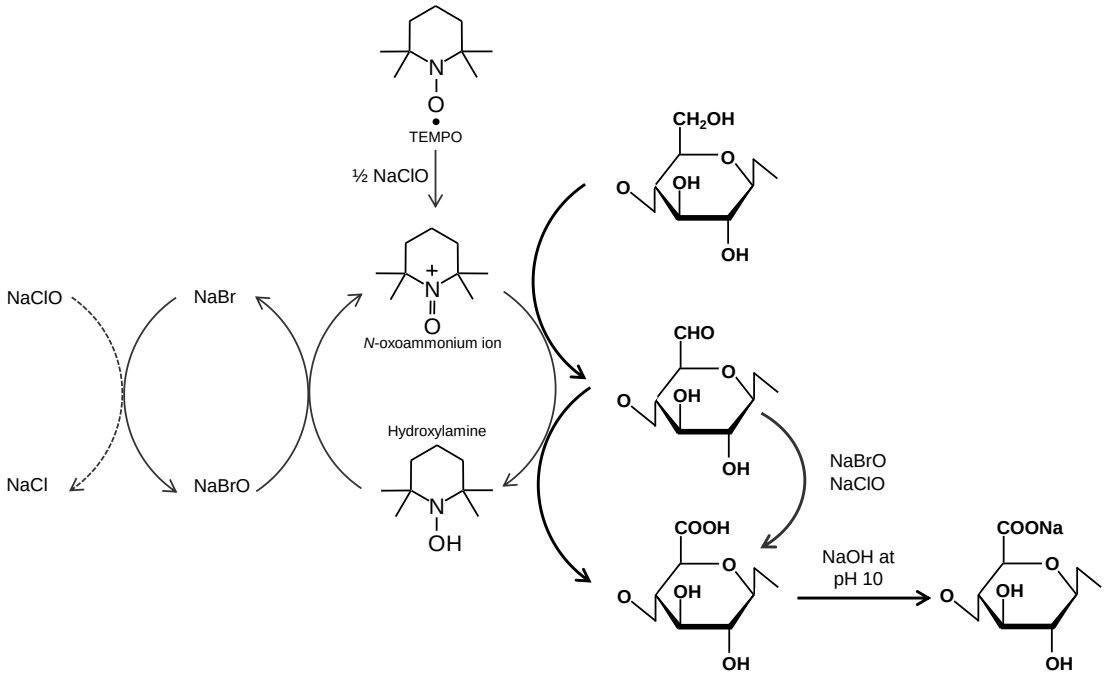

Figure 1.5. Oxidation of C6 primary hydroxyls to carboxylates by TEMPO/NaBr/NaClO system under alkaline conditions.

Recently, the TEMPO/NaClO/$NaClO_2$ system under weakly acidic or neutral conditions (Figure 1.6) has been reported as an effective TEMPO-oxidation method to control the depolymerization.[57–59] In this system, the obtained TEMPO-oxidized celluloses and TOCNs have no aldehyde groups, and thus depolymerization of celluloses caused by the β-elimination of glycoside bonds at the C6-aldehyde groups can be mostly avoided. TOCNs prepared from wood celluloses by this system have longer lengths than those prepared by the conventional TEMPO/NaBr/NaClO system.[58]

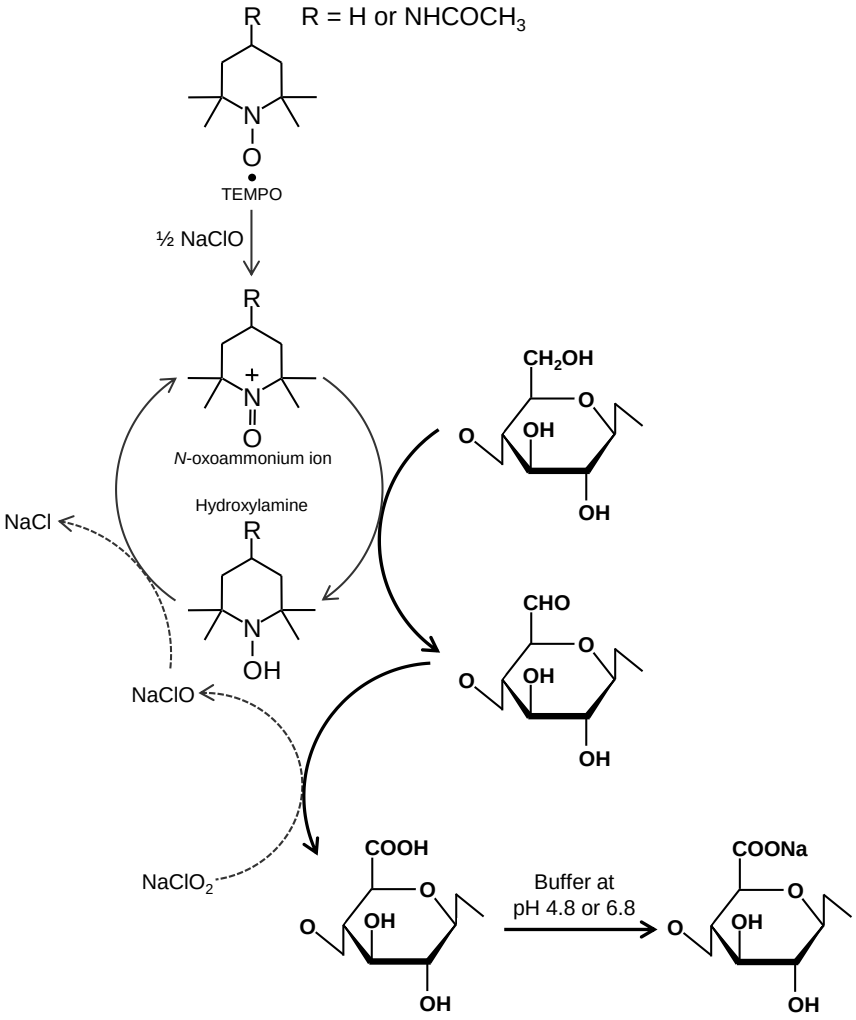

Figure 1.6. Oxidation of C6 primary hydroxyls to carboxylates by TEMPO/NaClO/$NaClO_2$ system under neutral and weakly acidic conditions. Reproduction of image with kind permission from Elsevier (© Elsevier 2012).

1.2.4. Application of nanocelluloses

Nanocelluloses, which inherit the outstanding characteristics of cellulose, have been applied to various materials: reinforcing fillers in polymer composites,[48,62] oxygen-barrier films,[63,64] substrates for electric devices,[65] heat insulators,[66] oil absorbents,[67] rheological modifiers,[38,39] and so on.[1,30,37,46,48] Nanocelluloses are prepared in common as dispersions in water. Therefore, it is particularly important to understand their rheological properties, or flow and viscoelastic properties, for producing

high-performance nanocellulose-based materials; processing or controlling nanocellulose/water dispersions is an initial and significant stage for their applications.

1.3. Rheological properties of cellulose suspensions and solutions

1.3.1. Pulp fiber suspensions

Studies on rheological properties of cellulosic fiber suspensions have been carried out in the field of papermaking over the years. The rheological properties of pulp fiber suspensions strongly depend on the fiber concentration and fiber morphology.[68] Mason first introduced the concept of the dilute region, in which fiber–fiber interactions are negligible, to the papermaking field.[69] He also defined the upper limit in the dilute region, namely critical concentration c^*, which is expressed using their aspect ratios p as $c^* = 3/(2p^2)$.[69] Kerekes et al. then refined the definition and found that the semi-dilute and concentrated regions depend on the numbers of contact per fiber, or the crowding number N.[68] The strength of the fiber network structures in the suspensions is estimated from the yield stresses of the pulp suspensions.[70–73] These yield stresses are characterized by a power-law dependence on their fiber concentrations. The rheological properties of the pulp fiber suspensions are also strongly influenced by fiber size/fiber size distribution, the stiffness of individual fibers, and the network structures formed by pulp fibers.[68,73,74]

1.3.2. Cellulose solutions

Rheological properties of molecularly-dispersed cellulose solutions have been well examined using various solvents as a function of concentration,[75,76] molecular weight,[75,76] and temperature.[77,78] Matsumoto and his co-authors reported fundamental rheological properties of various celluloses dissolved in a representative cellulose solvent, or LiCl/*N*,*N*-dimethylacetamide (DMAc)[75,76,79,80] They revealed that the shear viscosities η of the LiCl/DMAc solutions of cellulose show different solid-concentration dependences between the dilute and semi-dilute regimes. Their η values in the dilute region have a linear relationship to their concentrations c irrespective of the origins of the cellulose. Meanwhile, those in the

semi-dilute region, where intermolecular interactions become pronounced, are exponentially proportional to the c values; $\eta \propto c^{\alpha}$.[75,76] The similar tendencies are also observed for celluloses dissolved in other solvents, such as ionic liquids[81–84] and aqueous NaOH solutions.[77,78,81,85]

1.3.3. Nanocellulose dispersions

In rheological studies of nanocelluloses, NCCs and NFCs have been independently investigated as low-aspect-ratio rigid rods and high-aspect-ratio flexible fibers, respectively. The flow properties of NCCs, such as intrinsic viscosity [η] and maximum relaxation time τ, are well-described based on viscometric measurements of their dilute dispersions in terms of solid concentration,[86–90] hydrolysis conditions,[34,35] surface charge density,[34,35] and ionic strength.[87,91,92] Recently, shear viscosity measurements of dilute NCC dispersions have been studied to estimate the aspect ratios of well-dispersed, sulfate-estered NCC particles.[34,87]

For NFCs, because of their high viscoelasticity and thixotropy behavior of NFC dispersions, attention has focused on their application as thickeners and rheological modifiers,[38,39,49,93–96] and the flow properties of NFC dispersions in dilute systems are much less understood than those of NCCs. Fundamental understanding of NFC dispersions is difficult because of their tendency to form network structures in water.[97] Herrick first reported rheological properties of MFC dispersions,[39] followed by many studies on NFC dispersions, for example, in terms of disintegration conditions,[93,96,98] solid concentration,[49,94,95,97,99–105] ionic strength,[96,99,106–109] pH,[49,99,105,109,110] and temperature.[49,111] However, all these rheological studies were carried out in the semi-dilute or concentrated regions, in which the NFCs were dispersed as partially-agglomerated and entangled network-like structures. Therefore, comprehensive investigations of rheological properties of individualized NFC fibril/water dispersions are required. Since cellulose microfibrils are biosynthesized in water, findings for rheological properties of individualized NFC fibril/water dispersions would also contribute to a further understanding of cellulose microfibrils.

1.4. Research objectives

This study aims to reveal rheological properties of individualized NFC dispersions. Flow and viscoelastic properties of individualized NFC dispersions were comprehensively investigated in terms of length, width, surface charge density, flexibility, and concentration of the nanofibrils. The individually dispersed nanofibrils with surface carboxylate groups were prepared via TEMPO-mediated oxidation. The influences of the hemicelluloses adsorbed on the nanofibril surfaces were also assessed as a function of salt concentration and pH.

In chapter 2, influences of the length and surface charge density of individualized NFCs on flow properties of their dispersions were investigated. Ten types of NFCs with microscopy-determined average lengths of 270–980 nm and carboxylate contents of 1.2–1.8 mmol/g were used as samples. The maximum relaxation times τ of the NFC dispersions in dilute region were determined by shear viscosity measurement. Average lengths of the NFCs were evaluated by applying the τ values to a theoretical equation for rotational motions of rigid polymers, and then were compared with their microscopy-determined average lengths.

In chapter 3, influences of the width and flexibility of individualized NFCs on their flow properties were investigated. Four NFCs (width: 2.6 nm, aspect ratio: 103–376) and three NCCs (width: 3.8–14.4 nm, aspect ratio: 23–77) were used as samples. The maximum relaxation time τ and intrinsic viscosity $[\eta]$ of the NFC and NCC dispersions were investigated by experimental and theoretical aspects.

In chapter 4, viscoelastic properties of individualized NFCs in dispersion and wet film states were investigated in terms of solid concentrations, salt concentrations, and pH values. In addition to the highly charged, surface-carboxylated NFC with a low amount of hemicelluloses, core–shell-structured, hemicellulose-rich NFC with a low amount of surface-charged carboxylate groups was also used as a NFC sample.

1.5. References

1) Lindström, T.; Aulin, C.; Naderi, A.; Ankerfors, M. Microfibrillated cellulose. *Encyclopedia Of Polymer Science and Technology*: 2014.

2) 磯貝明, *セルロースの科学*; 朝倉書店: 2003.

3) 磯貝明, *セルロースの材料科学*; 東京大学出版会: 2001.

4) Saxena, I. M.; Brown Jr, R. M. Cellulose biosynthesis: current views and evolving concepts. *Ann. Bot.* **2005**, *96*, 9–21.

5) Cosgrove, D. J. Assembly and enlargement of the primary cell wall in plants. *Annu. Rev. Cell Dev. Biol.* **1997**, *13*, 171–201.

6) Cosgrove, D. J. Growth of the plant cell wall. *Nat. Rev. Mol. Cell Biol.* **2005**, *6*, 850–861.

7) Atalla, R. H.; Vanderheart, D. L. Native cellulose: a composite of two distinct crystalline forms. *Science* **1984**, *223*, 283–285.

8) VanderHart, D. L.; Atalla, R. Studies of microstructure in native celluloses using solid-state carbon-13 NMR. *Macromolecules* **1984**, *17*, 1465–1472.

9) Sugiyama, J.; Vuong, R.; Chanzy, H. Electron diffraction study on the two crystalline phases occurring in native cellulose from an algal cell wall. *Macromolecules* **1991**, *24*, 4168–4175.

10) Sakurada, I.; Nukushina, Y.; Ito, T. Experimental determination of the elastic modulus of crystalline regions in oriented polymers. *J. Polym. Sci.* **1962**, *57*, 651–660.

11) Šturcová, A.; Davies, G. R.; Eichhorn, S. J. Elastic modulus and stress-transfer properties of tunicate cellulose whiskers. *Biomacromolecules* **2005**, *6*, 1055–1061.

12) Iwamoto, S.; Kai, W.; Isogai, A.; Iwata, T. Elastic modulus of single cellulose microfibrils from tunicate measured by atomic force microscopy. *Biomacromolecules* **2009**, *10*, 2571–2576.

13) Wohlert, J.; Bergenstråhle-Wohlert, M.; Berglund, L. A. Deformation of cellulose nanocrystals: entropy, internal energy and temperature dependence. *Cellulose* **2012**, *19*, 1821–1836.

14) Saito, T.; Kuramae, R.; Wohlert, J.; Berglund, L. A.; Isogai, A. An ultrastrong nanofibrillar biomaterial: the strength of single cellulose nanofibrils revealed via sonication-induced fragmentation. *Biomacromolecules* **2013**, *14*, 248–253.

15) Hori, R.; Wada, M. The Thermal expansion of wood cellulose crystals. *Cellulose* **2005**, *12*, 479–484.

16) Ochoa-Villarreal, M.; Aispuro-Hernández, E.; Vargas-Arispuro, I.; Martínez-Téllez, M. Á., *Plant cell wall polymers: function, structure and biological activity of their derivatives;* INTECH Open Access Publisher: 2012.

17) Prakobna, K.; Galland, S.; Berglund, L. A. High-performance and moisture-stable cellulose–starch nanocomposites based on bioinspired core–shell nanofibers. *Biomacromolecules* **2015**, *16*, 904–912.

18) Whitney, S. E.; Gothard, M. G.; Mitchell, J. T.; Gidley, M. J. Roles of cellulose and xyloglucan in determining the mechanical properties of primary plant cell walls. *Plant Physiol.* **1999**, *121*, 657–664.

19) Sehaqui, H.; Zhou, Q.; Berglund, L. A. Nanostructured biocomposites of high toughness—a wood cellulose nanofiber network in ductile hydroxyethylcellulose matrix. *Soft Matter* **2011**, *7*, 7342–7350.

20) Larsson, P.; Berglund, L.; Wågberg, L. Highly ductile fibres and sheets by core-shell structuring of the cellulose nanofibrils. *Cellulose* **2014**, *21*, 323–333.

21) Larsson, P. A.; Berglund, L. A.; Wågberg, L. Ductile all-cellulose nanocomposite films fabricated from core–shell structured cellulose nanofibrils. *Biomacromolecules* **2014**, *15*, 2218–2223.

22) Prakobna, K.; Terenzi, C.; Zhou, Q.; Furó, I.; Berglund, L. A. Core–shell cellulose nanofibers for biocomposites – Nanostructural effects in hydrated state. *Carbohydr. Polym.* **2015**, *125*, 92–102.

23) Prakobna, K.; Kisonen, V.; Xu, C.; Berglund, L. A. Strong reinforcing effects from galactoglucomannan hemicellulose on mechanical behavior of wet cellulose nanofiber gels. *J. Mater. Sci.* **2015**, *50*, 7413–7423.

24) Galland, S.; Berthold, F.; Prakobna, K.; Berglund, L. A. Holocellulose nanofibers of high molar mass and small diameter for high-strength nanopaper. *Biomacromolecules* **2015**, *16*, 2427–2435.

25) Kollmann, F. F.; Côte Jr, W. A., *Principles of wood science and technology. vol. I. Solid Wood.;* Springer-Verlag: 1968.

26) Rånby, B. G. Cellulose and muscle-the colloidal properties of cellulose micelles. *Discuss. Faraday Soc.* **1951**, 158–164.

27) Habibi, Y.; Lucia, L. A.; Rojas, O. J. Cellulose nanocrystals: chemistry, self-assembly, and applications. *Chem. Rev.* **2010**, *110*, 3479–3500.

28) Eichhorn, S. J. Cellulose nanowhiskers: promising materials for advanced applications. *Soft Matter* **2011**, *7*, 303–315.

29) Araki, J. Electrostatic or steric? - preparations and characterizations of well-dispersed systems containing rod-like nanowhiskers of crystalline polysaccharides. *Soft Matter* **2013**, *9*, 4125–4141.

30) Azizi Samir, M. A. S.; Alloin, F.; Dufresne, A. Review of recent research into cellulosic whiskers, their properties and their application in nanocomposite field. *Biomacromolecules* **2005**, *6*, 612–626.

31) Rånby, B. G.; Ribi, E. Über den Feinbau der Zellulose. *Experientia* **1950**, *6*, 12–14.

32) Revol, J.-F.; Bradford, H.; Giasson, J.; Marchessault, R.; Gray, D. Helicoidal self-ordering of cellulose microfibrils in aqueous suspension. *Int. J. Biol. Macromol.* **1992**, *14*, 170–172.

33) Marchessault, R.; Morehead, F.; Walter, N. Liquid crystal systems from fibrillar polysaccharides. *Nature* **1959**, *184*, 632–633.

34) Araki, J.; Wada, M.; Kuga, S.; Okano, T. Flow properties of microcrystalline cellulose suspension prepared by acid treatment of native cellulose. *Colloids Surf., A* **1998**, *142*, 75–82.

35) Araki, J.; Wada, M.; Kuga, S.; Okano, T. Influence of surface charge on viscosity behavior of cellulose microcrystal suspension. *J. Wood Sci.* **1999**, *45*, 258–261.

36) Lavoine, N.; Desloges, I.; Dufresne, A.; Bras, J. Microfibrillated cellulose–Its barrier properties and applications in cellulosic materials: A review. *Carbohydr. Polym.* **2012**, *90*, 735–764.

37) Isogai, A. Wood nanocelluloses: fundamentals and applications as new bio-based nanomaterials. *J. Wood Sci.* **2013**, *59*, 449–459.

38) Turbak, A. F.; Snyder, F. W.; Sandberg, K. R. Microfibrillated cellulose, a new cellulose product: properties, uses, and commercial potential. *J. Appl. Polym. Sci. Appl. Polym. Symp.* **1983**, *37*, 815–827.

39) Herrick, F. W.; Casebier, R. L.; Hamilton, J. K.; Sandberg, K. R. In Microfibrillated cellulose: morphology and accessibility, *J. Appl. Polym. Sci.: Appl. Polym. Symp.*, 1983,*37*, 797–813.

40) Siqueira, G.; Bras, J.; Dufresne, A. Cellulosic bionanocomposites: a review of preparation, properties and applications. *Polymers* **2010**, *2*, 728–765.

41) Abe, K.; Iwamoto, S.; Yano, H. Obtaining cellulose nanofibers with a uniform width of 15 nm from wood. *Biomacromolecules* **2007**, *8*, 3276–3278.

42) Iwamoto, S.; Nakagaito, A.; Yano, H. Nano-fibrillation of pulp fibers for the processing of transparent nanocomposites. *Appl. Phys. A:* **2007**, *89*, 461–466.

43) Taniguchi, T.; Okamura, K. New films produced from microfibrillated natural fibres. *Polym. Int.* **1998**, *47*, 291–294.

44) Isogai, A.; Saito, T.; Fukuzumi, H. TEMPO-oxidized cellulose nanofibers. *Nanoscale* **2011**, *3*, 71–85.

45) Spence, K. L.; Venditti, R. A.; Rojas, O. J.; Habibi, Y.; Pawlak, J. J. A comparative study of energy consumption and physical properties of microfibrillated cellulose produced by different processing methods. *Cellulose* **2011**, *18*, 1097–1111.

46) Siró, I.; Plackett, D. Microfibrillated cellulose and new nanocomposite materials: a review. *Cellulose* **2010**, *17*, 459–494.

47) Nakagaito, A. N.; Yano, H. The effect of morphological changes from pulp fiber towards nano-scale fibrillated cellulose on the mechanical properties of high-strength plant fiber based composites. *Appl. Phys. A:* **2004**, *78*, 547–552.

48) Klemm, D.; Kramer, F.; Moritz, S.; Lindström, T.; Ankerfors, M.; Gray, D.; Dorris, A. Nanocelluloses: a new family of nature-based materials. *Angew. Chem. Int. Ed.* **2011**, *50*, 5438–5466.

49) Pääkkö, M.; Ankerfors, M.; Kosonen, H.; Nykänen, A.; Ahola, S.; Österberg, M.; Ruokolainen, J.; Laine, J.; Larsson, P. T.; Ikkala, O.; Lindström, T. Enzymatic hydrolysis combined with mechanical shearing and high-pressure homogenization for nanoscale cellulose fibrils and strong gels. *Biomacromolecules* **2007**, *8*, 1934–1941.

50) Henriksson, M.; Henriksson, G.; Berglund, L.; Lindström, T. An environmentally friendly method for enzyme-assisted preparation of microfibrillated cellulose (MFC) nanofibers. *Eur. Polym. J.* **2007**, *43*, 3434–3441.

51) Wågberg, L.; Decher, G.; Norgren, M.; Lindström, T.; Ankerfors, M.; Axnas, K. The Build-Up of polyelectrolyte multilayers of microfibrillated cellulose and cationic polyelectrolytes. *Langmuir* **2008**, *24*, 784–795.

52) Aulin, C.; Ahola, S.; Josefsson, P.; Nishino, T.; Hirose, Y.; Österberg, M.; Wågberg, L. Nanoscale Cellulose Films with Different Crystallinities and Mesostructures—Their surface properties and interaction with water. *Langmuir* **2009**, *25*, 7675–7685.

53) Tingaut, P.; Zimmermann, T.; Lopez-Suevos, F. Synthesis and Characterization of bionanocomposites with tunable properties from poly(lactic acid) and acetylated microfibrillated cellulose. *Biomacromolecules* **2010**, *11*, 454–464.

54) Rodionova, G.; Lenes, M.; Eriksen, Ø.; Gregersen, Ø. Surface chemical modification of microfibrillated cellulose: improvement of barrier properties for packaging applications. *Cellulose* **2011**, *18*, 127–134.

55) Saito, T.; Isogai, A. TEMPO-mediated oxidation of native cellulose. The effect of oxidation conditions on chemical and crystal structures of the water-insoluble fractions. *Biomacromolecules* **2004**, *5*, 1983–1989.

56) Saito, T.; Nishiyama, Y.; Putaux, J.-L.; Vignon, M.; Isogai, A. Homogeneous Suspensions of individualized microfibrils from TEMPO-catalyzed oxidation of native cellulose. *Biomacromolecules* **2006**, *7*, 1687–1691.

57) Saito, T.; Hirota, M.; Tamura, N.; Isogai, A. Oxidation of bleached wood pulp by TEMPO/NaClO/NaClO2 system: effect of the oxidation conditions on carboxylate content and degree of polymerization. *J. Wood Sci.* **2010**, *56*, 227–232.

58) Tanaka, R.; Saito, T.; Isogai, A. Cellulose nanofibrils prepared from softwood cellulose by TEMPO/NaClO/$NaClO_2$ systems in water at pH 4.8 or 6.8. *Int. J. Biol. Macromol.* **2012**, *51*, 228–234.

59) Saito, T.; Hirota, M.; Tamura, N.; Kimura, S.; Fukuzumi, H.; Heux, L.; Isogai, A. Individualization of nano-sized plant cellulose fibrils by direct surface carboxylation using TEMPO catalyst under neutral conditions. *Biomacromolecules* **2009**, *10*, 1992–1996.

60) De Nooy, A.; Besemer, A.; Van Bekkum, H.; Van Dijk, J.; Smit, J. TEMPO-mediated oxidation of pullulan and influence of ionic strength and linear charge density on the dimensions of the obtained polyelectrolyte chains. *Macromolecules* **1996**, *29*, 6541–6547.

61) Shibata, I.; Isogai, A. Depolymerization of cellouronic acid during TEMPO-mediated oxidation. *Cellulose* **2003**, *10*, 151–158.

62) Eichhorn, S. J.; Dufresne, A.; Aranguren, M.; Marcovich, N. E.; Capadona, J. R.; Rowan, S. J.; Weder, C.; Thielemans, W.; Roman, M.; Renneckar, S.; Gindl, W.; Veigel, S.; Keckes, J.; Yano, H.; Abe, K.; Nogi, M.; Nakagaito, A. N.; Mangalam, A.; Simonsen, J.; Benight, A. S.; Bismarck, A.; Berglund, L. A.; Peijs, T. Review: current international research into cellulose nanofibres and nanocomposites. *J. Mater. Sci.* **2010**, *45*, 1–33.

63) Syverud, K.; Stenius, P. Strength and barrier properties of MFC films. *Cellulose* **2009**, *16*, 75–85.

64) Fukuzumi, H.; Saito, T.; Iwata, T.; Kumamoto, Y.; Isogai, A. Transparent and high gas barrier films of cellulose nanofibers prepared by TEMPO-mediated oxidation. *Biomacromolecules* **2009**, *10*, 162–165.

65) Koga, H.; Saito, T.; Kitaoka, T.; Nogi, M.; Suganuma, K.; Isogai, A. Transparent, conductive, and printable composites consisting of TEMPO-oxidized nanocellulose and carbon nanotube. *Biomacromolecules* **2013**, *14*, 1160–1165.

66) Kobayashi, Y.; Saito, T.; Isogai, A. Aerogels with 3D ordered nanofiber skeletons of liquid-crystalline nanocellulose derivatives as tough and transparent insulators. *Angew. Chem. Int. Ed.* **2014**, *53*, 10394–10397.

67) Korhonen, J. T.; Kettunen, M.; Ras, R. H. A.; Ikkala, O. Hydrophobic nanocellulose aerogels as floating, sustainable, reusable, and recyclable oil absorbents. *ACS Appl. Mater. Interfaces* **2011**, *3*, 1813–1816.

68) Kerekes, R. J. Rheology of suspensions-Pitch and deposits-rheology of fibre suspensions in papermaking: An overview of recent research. *Nord. Pulp Pap. Res. J.* **2006**, *21*, 598–612.

69) Mason, S. G. The motion of fibres in flowing liquids. *Pulp Pap. Mag. Can.* **1950**, *51*, 93–100.

70) Swerin, A.; Powell, R.; Ödberg, L. Linear and nonlinear dynamic viscoelasticity of pulp fiber suspensions. *Nord. Pulp Pap. Res. J.* **1992**, *7*, 126–133.

71) Wikström, T.; Rasmuson, A. The yield stress of pulp suspensions-The influence of fibre properties and processing conditions. *Nordic Pulp&Paper Research J.* **1998**, *13*, 78–85.

72) Horvath, A. E.; Lindström, T. The influence of colloidal interactions on fiber network strength. *J. Colloid Interface Sci.* **2007**, *309*, 511–517.

73) Derakhshandeh, B.; Kerekes, R.; Hatzikiriakos, S.; Bennington, C. Rheology of pulp fibre suspensions: A critical review. *Chem. Eng. Sci.* **2011**, *66*, 3460–3470.

74) Switzer III, L. H.; Klingenberg, D. J. Rheology of sheared flexible fiber suspensions via fiber-level simulations. *J. Rheol.* **2003**, *47*, 759–778.

75) Matsumoto, T.; Tatsumi, D.; Tamai, N.; Takaki, T. Solution properties of celluloses from different biological origins in LiCl· DMAc. *Cellulose* **2001**, *8*, 275–282.

76) Tamai, N.; Aono, H.; Tatsumi, D.; Matsumoto, T. Differences in rheological properties of solutions of plant and bacterial cellulose in LiCl/N, N-dimethylacetamide. *Nihon Reoroji Gakk.* **2003**, *31*, 119–130.

77) Budtova, T.; Navard, P. Cellulose in NaOH–water based solvents: a review. *Cellulose* **2015**, 1–51.

78) Budtova, T.; Navard, P. Viscosity-temperature dependence and activation energy of cellulose solutions. *Nord. Pulp Pap. Res. J.* **2015**, *30*, 99–104.

79) Tamai, N.; Tatsumi, D.; Matsumoto, T. Rheological properties and molecular structure of tunicate cellulose in LiCl/1, 3-dimethyl-2-imidazolidinone. *Biomacromolecules* **2004**, *5*, 422–432.

80) Aono, H.; Tamai, N.; Tatsumi, D.; Matsumoto, T. Aggregate structure and rheological properties of mercerized cellulose/LiCI DMAc solution. *Nihon Reoroji Gakk.* **2004**, *32*, 169–177.

81) Gericke, M.; Schlufter, K.; Liebert, T.; Heinze, T.; Budtova, T. Rheological properties of cellulose/ionic liquid solutions: from dilute to concentrated states. *Biomacromolecules* **2009**, *10*, 1188–1194.

82) Haward, S. J.; Sharma, V.; Butts, C. P.; McKinley, G. H.; Rahatekar, S. S. Shear and extensional rheology of cellulose/ionic liquid solutions. *Biomacromolecules* **2012**, *13*, 1688–1699.

83) Kosan, B.; Michels, C.; Meister, F. Dissolution and forming of cellulose with ionic liquids. *Cellulose* **2008**, *15*, 59–66.

84) Kuang, Q.-L.; Zhao, J.-C.; Niu, Y.-H.; Zhang, J.; Wang, Z.-G. Celluloses in an ionic liquid: the rheological properties of the solutions spanning the dilute and semidilute regimes. *J. Phys. Chem. B* **2008**, *112*, 10234–10240.

85) Roy, C.; Budtova, T.; Navard, P. Rheological properties and gelation of aqueous cellulose−NaOH solutions. *Biomacromolecules* **2003**, *4*, 259–264.

86) Marchessault, R.; Morehead, F.; Koch, M. J. Some hydrodynamic properties of neutral suspensions of cellulose crystallites as related to size and shape. *J. Colloid Sci.* **1961**, *16*, 327–344.

87) Boluk, Y.; Lahiji, R.; Zhao, L.; McDermott, M. T. Suspension viscosities and shape parameter of cellulose nanocrystals (CNC). *Colloids Surf., A* **2011**, *377*, 297–303.

88) Bercea, M.; Navard, P. Shear dynamics of aqueous suspensions of cellulose whiskers. *Macromolecules* **2000**, *33*, 6011–6016.

89) Lu, A.; Hemraz, U.; Khalili, Z.; Boluk, Y. Unique viscoelastic behaviors of colloidal nanocrystalline cellulose aqueous suspensions. *Cellulose* **2014**, *21*, 1239–1250.

90) González-Labrada, E.; Gray, D. G. Viscosity measurements of dilute aqueous suspensions of cellulose nanocrystals using a rolling ball viscometer. *Cellulose* **2012**, *19*, 1557–1565.

91) Lenfant, G.; Heuzey, M.; van de Ven, T.; Carreau, P. Intrinsic viscosity of suspensions of electrosterically stabilized nanocrystals of cellulose. *Cellulose* **2015**, *22*, 1109–1122.

92) Shafiei-Sabet, S.; Hamad, W.; Hatzikiriakos, S. Ionic strength effects on the microstructure and shear rheology of cellulose nanocrystal suspensions. *Cellulose* **2014**, *21*, 3347–3359.

93) Lasseuguette, E.; Roux, D.; Nishiyama, Y. Rheological properties of microfibrillar suspension of TEMPO-oxidized pulp. *Cellulose* **2008**, *15*, 425–433.

94) Naderi, A.; Lindström, T.; Sundström, J. Carboxymethylated nanofibrillated cellulose: rheological studies. *Cellulose* **2014**, *21*, 1561–1571.

95) Naderi, A.; Lindström, T.; Pettersson, T. The state of carboxymethylated nanofibrils after homogenization-aided dilution from concentrated suspensions: a rheological perspective. *Cellulose* **2014**, *21*, 2357–2368.

96) Naderi, A.; Lindström, T. Carboxymethylated nanofibrillated cellulose: effect of monovalent electrolytes on the rheological properties. *Cellulose* **2014**, *21*, 3507–3514.

97) Li, M.; Wu, Q.; Song, K.; Lee, S.; Qing, Y.; Wu, Y. Cellulose Nanoparticles: structure-morphology-rheology relationship. *ACS Sustainable Chem. Eng.* **2015**, *3*, 821–832.

98) Naderi, A.; Lindström, T.; Sundström, J. Repeated homogenization, a route for decreasing the energy consumption in the manufacturing process of carboxymethylated nanofibrillated cellulose? *Cellulose* **2015**, *22*, 1147–1157.

99) Agoda-Tandjawa, G.; Durand, S.; Berot, S.; Blassel, C.; Gaillard, C.; Garnier, C.; Doublier, J.-L. Rheological characterization of microfibrillated cellulose suspensions after freezing. *Carbohydr. Polym.* **2010**, *80*, 677–686.

100) Jowkarderis, L.; van de Ven, T. G. Rheology of semi-dilute suspensions of carboxylated cellulose nanofibrils. *Carbohydr. Polym.* **2015**, *123*, 416–423.

101) Nechyporchuk, O.; Belgacem, M. N.; Pignon, F. Concentration effect of TEMPO-oxidized nanofibrillated cellulose aqueous suspensions on the flow instabilities and small-angle X-ray scattering structural characterization. *Cellulose* **2015**, *22*, 2197–2210.

102) Tatsumi, D.; Ishioka, S.; Matsumoto, T. Effect of Fiber Concentration and axial ratio on the rheological properties of cellulose fiber suspensions. *Nihon Reoroji Gakk.* **2002**, *30*, 27–32.

103) Nechyporchuk, O.; Belgacem, M. N.; Pignon, F. Rheological properties of micro-/nanofibrillated cellulose suspensions: wall-slip and shear banding phenomena. *Carbohydr. Polym.* **2014**, *112*, 432–439.

104) Dimic-Misic, K.; Puisto, A.; Gane, P.; Nieminen, K.; Alava, M.; Paltakari, J.; Maloney, T. The role of MFC/NFC swelling in the rheological behavior and dewatering of high consistency furnishes. *Cellulose* **2013**, *20*, 2847–2861.

105) Saito, T.; Uematsu, T.; Kimura, S.; Enomae, T.; Isogai, A. Self-aligned integration of native cellulose nanofibrils towards producing diverse bulk materials. *Soft Matter* **2011**, *7*, 8804–8809.

106) Tatsumi, D.; Ishioka, S.; Matsumoto, T. Effect of particle and salt concentrations on the rheological properties of cellulose fibrous suspensions. *Nihon Reoroji Gakk.* **1999**, *27*, 243–248.

107) Sim, K.; Lee, J.; Lee, H.; Youn, H. Flocculation behavior of cellulose nanofibrils under different salt conditions and its impact on network strength and dewatering ability. *Cellulose* **2015**, *22*, 3689–3700.

108) Lowys, M. P.; Desbrières, J.; Rinaudo, M. Rheological characterization of cellulosic microfibril suspensions. Role of polymeric additives. *Food Hydrocolloids* **2001**, *15*, 25–32.

109) Jowkarderis, L.; van de Ven, T. G. Intrinsic viscosity of aqueous suspensions of cellulose nanofibrils. *Cellulose* **2014**, *21*, 2511–2517.

110) Way, A. E.; Hsu, L.; Shanmuganathan, K.; Weder, C.; Rowan, S. J. pH-Responsive cellulose nanocrystal gels and nanocomposites. *ACS Macro Lett.* **2012**, *1*, 1001–1006.

111) Iotti, M.; Gregersen, Ø. W.; Moe, S.; Lenes, M. Rheological studies of microfibrillar cellulose water dispersions. *J. Polym. Environ.* **2011**, *19*, 137–145.

Chapter 2

Influences of lengths and surface charge densities of nanocelluloses on the flow properties of their aqueous dispersions

2.1. Introduction

Investigations of the relationships between rheological properties of NFC dispersions and their lengths have recently been attempted. Dynamic viscoelastic measurements have been performed on NFC dispersions to estimate average lengths of NFC fibrils dispersed in water.[1,2] However, the average length measured by this method was ~12 μm even after corrected calculation, which is one order of magnitude higher than that measured by microscopy (~1 μm). This large discrepancy is probably because the NFC fibrils used in the dynamic viscoelastic measurements were not completely isolated but partially aggregated in water; the length of 12 μm might have been an overestimate for partially aggregated nanofibril networks. Therefore, dilute dispersions, in which nanofibrils do not interact with each other, should be used for dynamic viscoelastic measurements to evaluate the length of individual cellulose nanofibrils. However, dilute dispersions of individualized cellulose nanofibrils show extremely low viscoelasticities, or storage moduli, and loss moduli, which makes length evaluation almost impossible. Thus, the average lengths of individualized cellulose nanofibrils should be evaluated based on shear viscosity measurements that can measure minute changes in the viscosity of dilute fluids under shear flow.

Evaluation of the length of short whisker-shaped nanocrystalline celluloses (NCCs) by shear viscosity measurements has already been reported.[3,4] However, the lengths of such NCCs are very short at ~100 nm on average, which can be easily measured by microscopic observation using a transmission electron microscope (TEM) or an atomic force microscope (AFM). In addition, these NCCs are also not individualized but partially aggregated.

In the present section, the influences of lengths and surface charge densities of individualized NFCs on flow properties of their dilute dispersions were examined by evaluating their average lengths using shear viscosity measurements. Aqueous dispersions of individualized, long NFC fibrils with a uniform width of ~3 nm were prepared from wood cellulose by TEMPO-mediated oxidation and successive mechanical treatment in water. We prepared 10 types of TEMPO-oxidized cellulose nanofibrils (TOCNs) with different average lengths by controlling the conditions of the oxidation reaction or mechanical treatment. The average lengths of the TOCNs were evaluated using the equation for the flow behavior of rod-like polymer molecules in the dilute region defined by Doi and Edwards.[5] This equation has previously been used in the calculation of the average lengths of single-walled carbon nanotubes.[6]

2.2. Materials and methods

2.2.1. Materials

Softwood bleached kraft pulp, used as a cellulose sample, was supplied by Nippon Paper Industries Co. Ltd., Japan, in a never-dried state with a water content of 80%. For demineralization, the pulp was soaked in dilute HCl at pH 2.5 and room temperature for 0.5 h and repeatedly washed with deionized water by filtration. TEMPO, 4-acetamido-TEMPO (4-AcNH-TEMPO), sodium bromide, sodium chlorite, sodium chloride, sodium hydroxide, and sodium hypochlorite solution were of laboratory grade (Wako Pure Chemicals, Japan) and used without further purification.

2.2.2. Preparation of aqueous TOCN dispersions and those with NaCl

Ten TOCN dispersions (from A to J) were prepared following the previously reported methods.[7,8] The oxidation conditions of each of the dispersions are shown in Table 2.A1 in Appendix. TEMPO-mediated oxidation under alkaline conditions was conducted as follows.[7] Softwood cellulose (1 g) was suspended in water (100 mL) containing TEMPO (0.1 mmol) and sodium bromide (1 mmol). The TEMPO-mediated

oxidation was started by adding 1.8 M NaClO (10, 5, and 3.8 mmol g^{-1}–cellulose) to the cellulose slurry. The pH of the slurry was maintained at 10 by adding 0.5 M NaOH using a pH stat (AUT-501, TOADKK, Japan) at room temperature. After a designated time (1–5 h), the oxidized celluloses were thoroughly washed with water by filtration, and further treated with 1% $NaClO_2$ (100 mL) at pH 4.8 and room temperature for 2 days to oxidize residual C6-aldehydes to carboxyls. The fully-oxidized celluloses were thoroughly washed with distilled water. A 0.1% w/v slurry of the oxidized cellulose was sonicated using a Nihon Seiki US-300T (300 W, 19.5 kHz) ultrasonic homogenizer for 8–80 min. The unfibrillated fraction was then removed by centrifugation at 12000 × *g* for 20 min to yield four transparent aqueous TOCN dispersions (A, B, C, and D). 10 mM NaCl solution was added to the aqueous 0.1 % w/v TOCN-A and TOCN-D dispersions to produce dispersions having NaCl concentrations of 0, 0.5, 1, 2, and 5 mM. The dispersions were shaken at 150 rpm overnight using an automatic rotary shaker (ROTAMAX 120, Heidolph, Germany).

TEMPO-mediated oxidation under neutral or weakly acidic conditions was conducted as follows.[8] Softwood cellulose (1 g) was suspended in 0.1 M sodium phosphate buffer (100 mL, pH 6.8) or 0.1 M acetate buffer (100 mL, pH 4.8) containing 4-AcNH-TEMPO (0.1 mmol) and $NaClO_2$ (10 mmol) in an airtight flask. 1.8 M NaClO (0.5 mL, 1.0 mmol) was added to the flask in one step. The flask was immediately stoppered, and the slurry was stirred at 40 °C for a designated time (48–120 h). After cooling the slurry to room temperature, the oxidized celluloses were thoroughly washed with distilled water by filtration. A 0.1% w/v slurry of the oxidized cellulose was sonicated using the Nihon Seiki US-300T (300 W, 19.5 kHz) for 8–80 min. Centrifugation of the dispersions at 12000 × *g* for 20 min to remove unfibrillated fractions yielded six transparent aqueous TOCN dispersions (E, F, G, H, I, and J).

Excluding the TOCN-B and TOCN-H dispersions, the 0.1% w/v TOCN dispersions and the 0.1% w/v TOCN-A and TOCN-D dispersions with NaCl were diluted to 0.006–0.09% w/v by adding distilled water. The TOCN-B and TOCN-H dispersions were carefully concentrated to 0.6% w/v using a rotary evaporator

(Rotavapor R-210, BUCHI Labortechnil AG, Switzerland) and then diluted to 0.11–0.55% w/v by adding distilled water.

2.2.3. Analyses

The carboxylate contents of the oxidized celluloses were determined using an electric conductivity titration method (Table. 2.1).[9] The ζ-potentials of TOCN-A and TOCN-D in the 0.03% w/v dispersions were measured at 25 ºC using a particle analyzer (Delsa Nano HC, Beckman Coulter Inc., USA) based on electrophoretic light scattering.[4] The turbidity of the 0.1% w/v TOCN dispersions at 0–5 mM NaCl was measured using a V-670 spectrophotometer (JASCO Co., Japan) at wavelengths of 300–800 nm, for which the dispersions were placed in a disposable poly(methyl methacrylate) cuvette.

A capillary viscometer was used to obtain the intrinsic viscosities of freeze-dried TOCNs (0.04 g) dissolved in 0.5 M cupriethylene diamine (cuen) for 5 min. The obtained values were converted to viscosity-average degrees of polymerization DP_v using a previously reported equation, $[\eta] = 0.57 \times DP_v$.[7]

Transmission electron microscopy (TEM) observations were performed using a JEOL JEM-2000EX microscope operated at an accelerating voltage of 200 kV. A 10 μL aliquot of 0.0001% w/v TOCN dispersion was mounted on a glow-discharged carbon-coated Cu grid. The excess liquid was absorbed by a filter paper, and one drop of 2% uranyl acetate was added as a negative stain for the TOCNs. Excess solution was blotted out with a filter paper, and the grid was allowed to dry by evaporation. The sample grid was observed using TEM in the bright-field mode. Lengths of ~200 isolated TOCNs were measured on the TEM images using an image processing software (Image-J version 1.45). Kinks in the TOCNs were ignored; each length was measured as for one connected TOCN, even if it had kinks. The arithmetic mean length L_a and the weighted mean length L_w of all the TOCNs were determined following the previously reported method (the details of which are written in the Appendix).[7] The polydispersity index of the length distributions was calculated by dividing L_w by L_a.[10]

The shear viscosities of the TOCN dispersions were measured at 25 ºC using a stress-controlled rheometer (MCR 302, Anton Paar GmbH., Graz, Austria). The TOCN dispersions were left at rest for ~30 min before measurement. For the TOCN-B and TOCN-H dispersions with extremely low viscosities, the shear viscosities were measured using a cone-plate geometry (plate diameter of 49.975 mm and angle of 1.986°) that is suitable for the measurement at high shear rates (> 50 s^{-1}). The other dispersions (TOCNs-A, -C, -D, -E, -F, -G, -I, and -J) were tested using a double cylinder fixture (cup 28.934 mm, bob: 26.657 mm) that is suitable for the measurement at the low shear rates (1–10 s^{-1}). A vapor trap was used to prevent the dispersion from evaporating during the measurement. It took ~40 min to measure shear viscosities of one TOCN dispersion sample at each concentration. The shear rate ($\dot{\gamma}$) was set in the range of 1–1000 s^{-1} and increased logarithmically.

2.3. Results and discussion

2.3.1. Length evaluation method

The ten types of TOCNs prepared in the present study (from A to J) had a uniform width of ~3 nm and different average lengths (Figure 2.1). The weighted mean lengths L_w of the TOCNs observed by TEM were in the range of ~300–1,000 nm (Table 2.1). We evaluated the viscosity-average lengths L_{visc} of the TOCNs using the following equation for the rotational motions of rigid rod-like particles in the dilute region,[5]

$$\tau = \frac{1}{6D_r} = \frac{\pi\eta_s L^3}{18k_B T\left(\ln\left(L/d\right) - 0.8\right)} \quad (2.1)$$

where τ *is* the maximum relaxation time, D_r is the rotational diffusion constant, d is the diameter of the rod-like particle or TOCN, T is the absolute temperature, η_s is the solvent viscosity, and k_B is the Boltzmann constant.

Because the diameter *d* can be substituted with the width ~3 nm of the TOCNs,[11] the L_{visc} of TOCNs depend only on the maximum relaxation time τ. τ corresponds to the inverse of the critical shear rate $\dot{\gamma}_{crit}$, and the value of $\dot{\gamma}_{crit}$ can be determined by shear viscosity measurement.

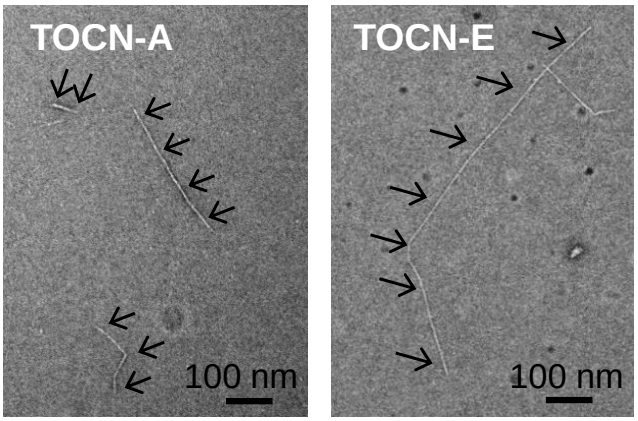

Figure 2.1. TEM images of TOCN-A and TOCN-E. Reproduction of image with kind permission from Springer Science (© Springer 2014) and Business Media.

Table 2.1. Summary of arithmetic mean length L_a, weighted mean length L_w, polydispersity index L_w/L_a, carboxylate content, and critical concentration c^{*a} of the TOCNs. Reproduction of table with kind permission from Springer Science (© Springer 2014) and Business Media.

	Arithmetic mean length, L_a (nm)	Weighted mean length, L_w (nm)	Polydispersity index, L_w/L_a	Carboxylate content (mmol g^{-1})	Critical concentration, c^* (% w/v)
A	370 ± 168	440	1.19	1.8	0.060
B	208 ± 111	270	1.30	1.8	0.260
C	440 ± 246	570	1.30	1.5	0.030
D	560 ± 251	670	1.2	1.2	0.022
E	720 ± 433	980	1.36	1.3	0.010
F	560 ± 317	740	1.32	1.3	0.022
G	440± 224	550	1.25	1.3	0.050
H	262 ± 136	330	1.26	1.3	0.140
I	580 ± 311	750	1.29	1.5	0.020
J	703 ± 436	970	1.38	1.3	0.014

[a] Boundary concentration between dilute and semi-dilute region (see text)

2.3.2. Influence of electric double-layer on shear viscosity

The influences of the electric double-layers of TOCNs in water on the shear viscosities of the TOCNs were investigated. An electric double-layer surrounds a TOCN that has a significant amount of anionic carboxylate groups on the surface.[12] The thickness of the electric double-layer is referred as a Debye length κ^{-1} and is defined by the following equation,

$$\kappa^{-1} = \left(\sqrt{\frac{2\pi n z^2 e^2}{\varepsilon_0 \varepsilon_r k_B T}} \right)^{-1} \quad (2.2)$$

where n is the concentration of the electrolyte, z is the valance of the electrolyte, e is the elementary charge, ε_0 is the absolute permittivity, ε_r is the dielectric constant, k_B is the Boltzmann constant, and T is the absolute temperature.[13,14] As shown in Figure 2.2a, the theoretical κ^{-1} values hyperbolically decrease with increasing NaCl concentration in the dispersion medium. Thus, the κ^{-1} values of TOCNs dispersed in pure water are much larger than those dispersed in NaCl solutions.

To estimate the change in κ^{-1} values of TOCNs with salt concentration, the ζ-potentials of TOCN-A and TOCN-D dispersed in NaCl solution were measured. TOCN-A and TOCN-D had carboxylate contents of 1.8 and 1.2 mmol g^{-1}, respectively. Figure 2.2b shows the ζ-potentials of the TOCN-A and TOCN-D in water as a function of NaCl concentration. Although there is a significant difference in carboxylate content between TOCN-A and TOCN-D, both TOCNs had ζ-potentials of about –60 mV in pure water. The ζ-potentials of TOCN-A and TOCN-D similarly decreased to –45 mV, when the NaCl concentration was increased to 5 mM. This result indicates that the electric double-layers of TOCN-A and TOCN-D were similarly compressed with increasing NaCl concentration; the decrease in κ^{-1} of TOCNs by salt concentration is independent of their carboxylate contents of TOCNs.[13]

The dispersibility of the TOCNs in salt solution was investigated by turbidity measurement. Figure 2.2c shows the turbidity of 0.1% w/v TOCN-A dispersions containing different amounts of NaCl. The turbidity curve of the TOCN dispersion with 0.5 mM NaCl was completely overlapped with that without NaCl, showing that the TOCNs were as fully dispersed in 0.5 mM NaCl solution as those in pure water. However, the turbidity of dispersions with more than 1 mM NaCl became greater with NaCl concentration, showing that TOCNs aggregate at NaCl concentrations higher than 1 mM. It is known that the turbidity of a rod-like particle dispersion has a linear correlation to the square of the width of the rod-like particles.[15] Therefore, the dispersions with lower than 0.5 mM NaCl should be used for the length evaluation of individual TOCNs by shear viscosity measurement.

The influence of κ^{-1} on the length evaluation using Eq. 2.1 was investigated by comparing the critical shear rates $\dot{\gamma}_{crit}$ of the TOCN-A dispersions at 0 and 0.5 mM NaCl. Figure 2.2d shows the reduced viscosity, η_{red}, of the TOCN dispersions as a function of shear rate. The $\dot{\gamma}_{crit}$ values were determined as the shear rate at the beginning of shear-thinning and were 30 s^{-1} for both the 0 and 0.5 mM NaCl-TOCN dispersions. The viscosity-average lengths L_{visc} were calculated by substituting the $\dot{\gamma}_{crit}$ values into Eq. 2.1; the L_{visc} of the TOCNs in pure water and those in 0.5 mM NaCl solution were the same. This is because very dilute dispersions of 0.055% w/v were used in the shear viscosity measurements (see Appendix for details); in such dilute dispersions, interactions between TOCN elements are negligible regardless of the NaCl concentration. As a result, the influence of the electric double-layer thickness κ^{-1} on the length evaluation was negligible. Thus, the evaluation of TOCN length in the present study was performed by measuring the shear viscosities of TOCN dispersions without NaCl.

In the present study, the contributions of the water bound on the TOCN surfaces to the shear viscosity were ignored, assuming that (1) there are no interactions between the TOCNs covered with the bound water in dilute dispersions, and (2) TOCNs are stiff and rod-like particles and thus the bound water is supposed to have no contributions to expanding the TOCN elements in dilute dispersions. For thick TOCN dispersions (> 1% w/v), the contributions of the bound water should be taken into account.[16]

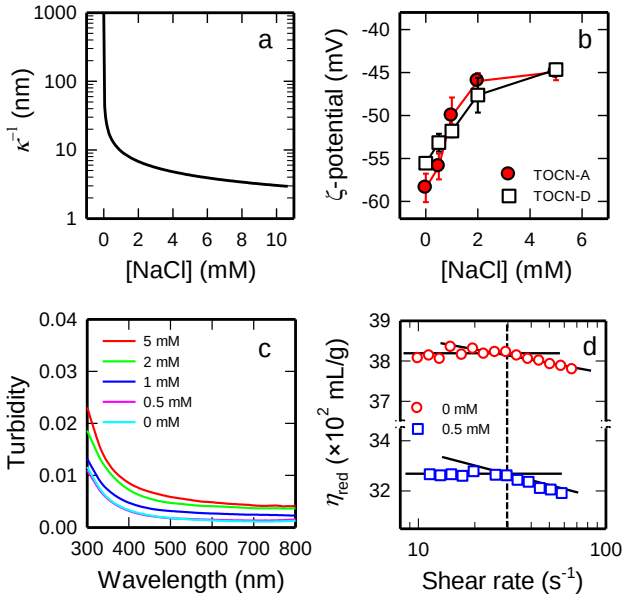

Figure 2.2. Influence of TOCN electric double-layer on length evaluation based on shear viscosity measurements: (a) Debye length as a function of NaCl concentration, (b) ζ-Potentials of TOCN-A and TOCN-D as a function of NaCl concentration, (c) turbidity of 0.1% w/v TOCN-A dispersion at 0–5 mM NaCl, and (d) reduced viscosity η_{red} of TOCN-A dispersion at 0 or 0.5 mM NaCl. Reproduction of image with kind permission from Springer Science (© Springer 2014) and Business Media.

2.3.3. Determination of dilute region

Dilute dispersions, in which interactions between polymer molecules are negligible, should be used when evaluating the length of rod-like polymer molecules by shear viscosity. The dilute region of a dispersion is determined by investigating changes in specific viscosity η_{sp} as a function of dispersion concentration.[17,18] Figure 2.3 shows the η_{sp} of the TOCN-H dispersion. A linear region was observed in the dilute region at low concentrations up to 0.14% w/v; a power-law scaling region was then observed in the semi-dilute region of more than 0.14% w/v. The critical concentration c^*, or a boundary concentration between the dilute and semi-dilute region, of the TOCN-H dispersion was determined to be 0.14% w/v. The c^* values of the other TOCN dispersions were also determined in the same way (Table 2.1).

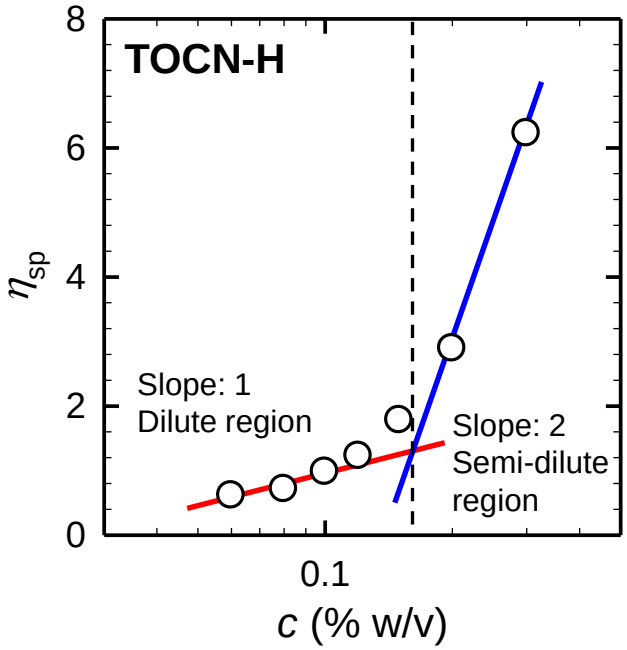

Figure 2.3. Specific viscosity η_{sp} of TOCN-H dispersions as a function of TOCN concentration c.

Mason calculated a relationship between c^* and the aspect ratio p of rigid-rod fibers, assuming independent-fiber motion in a one-dimensional shear field;[19] $c^* = 3/(2p^2)$. In the present study, the following relationship between c^* and p of the TOCNs was found,

$$c^* = \frac{18}{p^2} \tag{2.3}$$

where p is the ratio of the weighted mean length L_w to the width of the TOCNs (Figure 2.4). The coefficient 18 in Eq. 2.3 was much greater than that of Mason's estimation, 3/2. This is probably because the p values of the TOCNs, 90–330, were much greater than those that Mason assumed, 20–60.[19] The shear viscosity behavior in the dilute region of the TOCN dispersions was hereafter investigated.

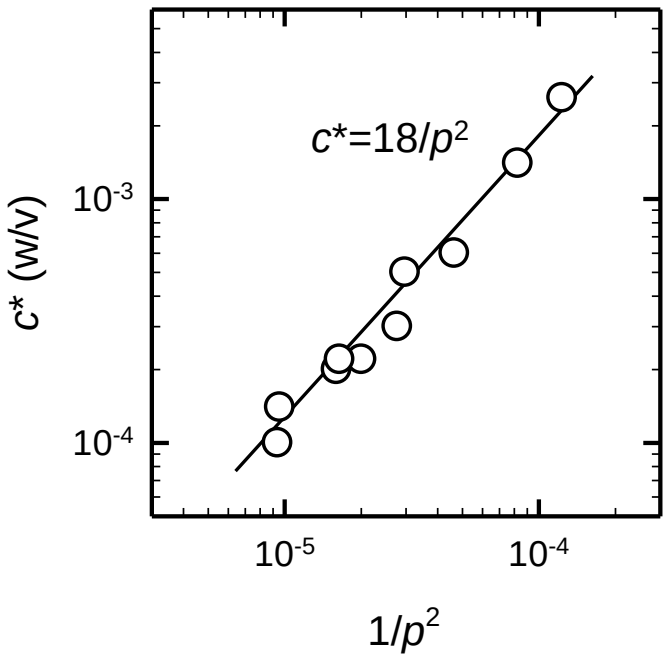

Figure 2.4. Critical concentration c^* as a function of the inverse square of the aspect ratio $1/p^2$.

2.3.4. Length evaluation by shear viscosity

The average lengths of the ten types of TOCNs were evaluated based on shear viscosity measurements. Figure 2.5 shows the reduced viscosity η_{red} of the dispersions in the dilute region as a function of shear rate. All the TOCN dispersions showed shear-thinning behavior. The critical shear rates $\dot{\gamma}_{crit}$, or the shear rates at the beginning of shear-thinning, of the TOCN dispersions were inversely proportional to the L_w values (Figure 2.A2 in Appendix). The viscosity-average lengths L_{visc} were calculated by substituting the inverse of $\dot{\gamma}_{crit}$ into Eq. 2.1. The obtained L_{visc} values ranged widely from ~1,100 to 2,500 nm and were greater than the L_w values (~300–1,000 nm). This is probably because TOCNs in real systems are semi-flexible rather than completely rigid rods.[20]

The following linear relationship between the L_{visc} and L_w values of all the TOCNs existed (Figure 2.6);

$$L_{visc} = 1.764 \times L_w + 764 \quad (2.4)$$

Although the carboxylate contents of TOCNs (A and B) were significantly different from those of the other TOCNs (E, F, G, and H), the L_{visc} of these six types of TOCNs are placed in the same straight line described by Eq. 2.4 (the carboxylate contents of the TOCNs are shown in Table 2.1). This result indicates that the influence of the surface-carboxylate content of the TOCNs on the length evaluation was negligible; interactions between TOCNs in the dilute dispersions were negligible, irrespective of their carboxylate contents.

Furthermore, a linear relationship between the L_{visc} values and the viscosity-average degrees of polymerization DP_v of the TOCNs was found (Figure 2.7). It is significant that the fibrillar dispersions and molecular solutions of cellulose showed a correlation in viscosity measurements, indicating that the lengths of the cellulose nanofibrils are correlated to those of their cellulose molecules.

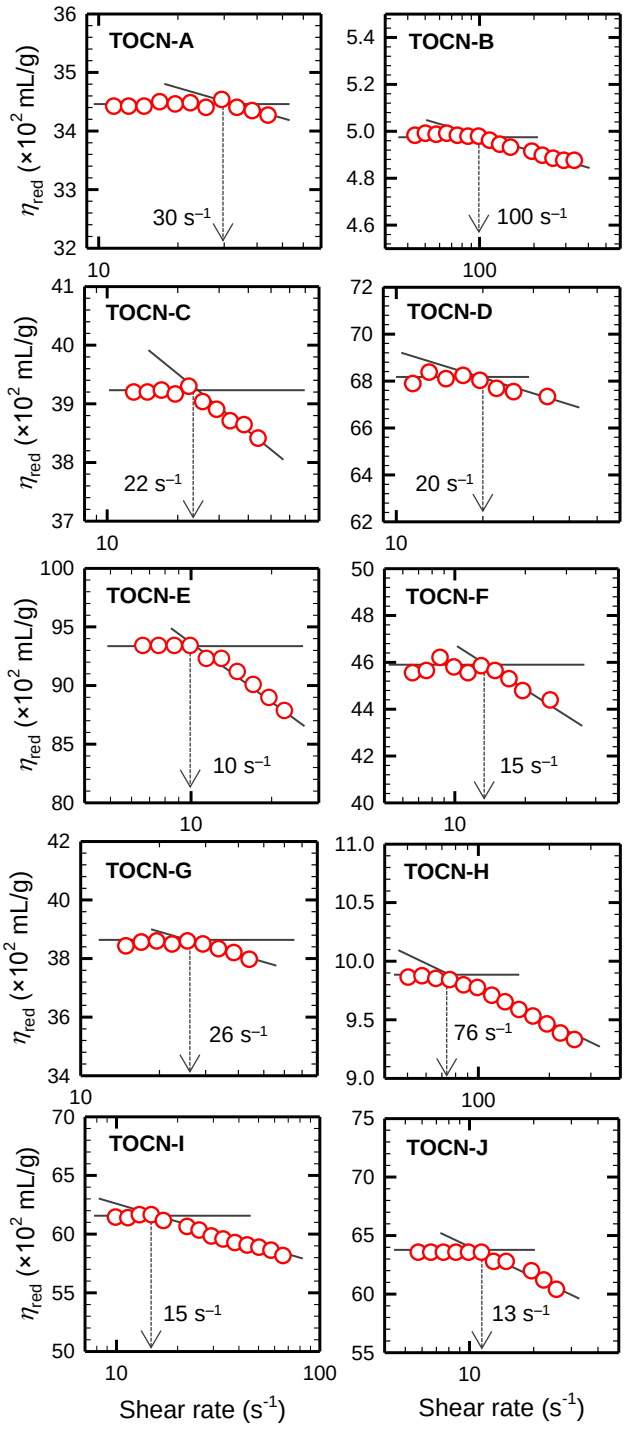

Figure 2.5. Reduced viscosity η_{red} of the TOCN dispersions as a function of shear rate. Reproduction of image with kind permission from Springer Sience (© Springer 2014) and Business Media.

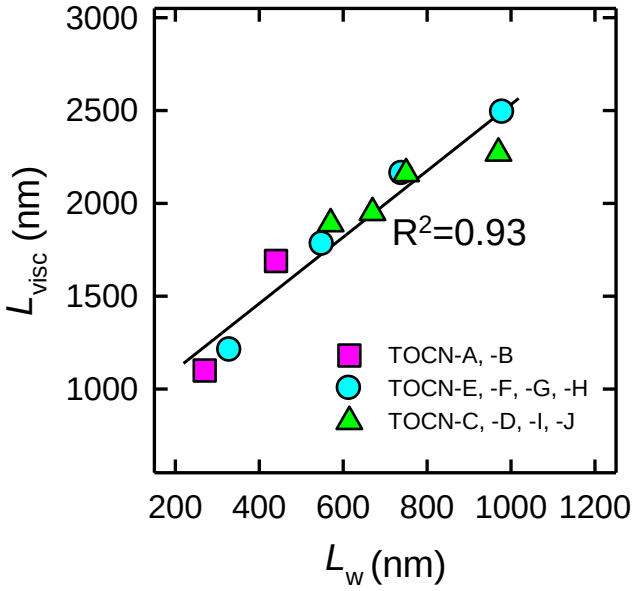

Figure 2.6. Relationship between weighted mean lengths L_w and viscosity-average lengths L_{visc} of the TOCNs. Carboxylate contents of TOCNs *A* and *B* were 1.8 mmol g^{-1}, those of TOCNs *E*–*H* were 1.3 mmol g^{-1}, and those of TOCNs *C*, *D*, *I*, and *J* were 1.2–1.5 mmol g^{-1}. Reproduction of image with kind permission from Springer Science (© Springer 2014) and Business Media.

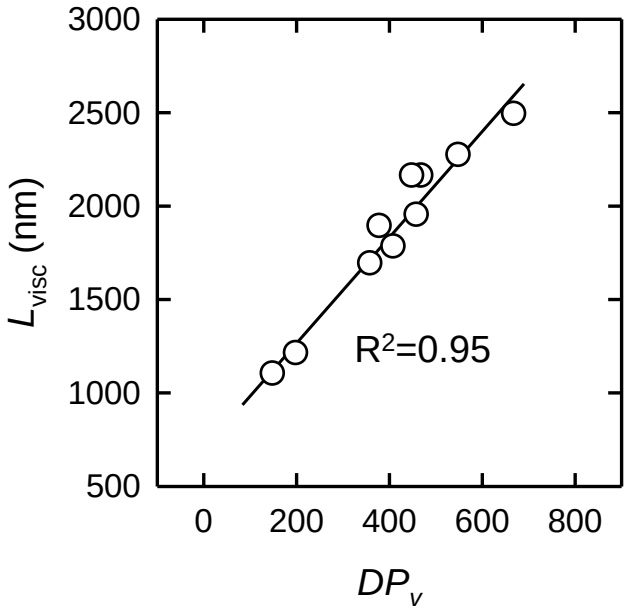

Figure 2.7. Relationship between viscosity-average degrees of polymerization DP_v and viscosity-average lengths L_{visc} of TOCNs. Reproduction of image with kind permission from Springer Science (© Springer 2014) and Business Media.

2.4. Conclusions

The average lengths of individualized NFC fibrils with a uniform width (~3 nm) were determined by a shear viscosity method for dilute TOCN dispersions. The resulting viscosity-average lengths L_{vsic} of the TOCNs ranged from ~1,100 nm to 2,500 nm. There was a linear relationship between the L_{vsic} values and L_w values obtained by TEM observation of the TOCNs, which is described as $L_{visc} = 1.764 \times L_w + 764$. Furthermore, the L_{vsic} values were also proportional to the DP_v values of molecular solutions of the TOCNs. Influences of the Debye length and surface-charge contents of the TOCNs on the length evaluation were negligible under the conditions used in this study. The critical concentration c^* of the TOCN dispersions, below which interactions between the nanofibrils are negligible, is described as $c^* = 18/p^2$ using the aspect ratios p of the nanofibrils.

2.5. Appendix

2.5.1. Oxidation conditions, carboxylate content, and viscosity-average degree of polymerization DP_v of the TOCNs

Table 2.A1. Summary of oxidation conditions (pH, NaClO added, and reaction time), carboxylate content and viscosity-average degree of polymerization DP_v of the TOCNs. Reproduction of table with kind permission from Springer Science (© Springer 2014) and Business Media.

	TEMPO/NaBr/NaClO system				TEMPO/NaClO/$NaClO_2$ system					
	A	B	C	D	E	F	G	H	I	J
pH	10	10	10	10	4.8	4.8	4.8	4.8	6.8	4.8
NaClO added (mmol g^{-1})	10	10	5	3.8	1	1	1	1	1	1
Reaction time (h)	5	5	2	1	72	72	72	72	120	48
Carboxylate content (mmol g^{-1})	1.8	1.8	1.5	1.2	1.3	1.3	1.3	1.3	1.5	1.3
DP_v	330	150	350	410	580	450	410	200	420	490

2.5.2. Length distribution histograms of TOCNs

The arithmetic mean length L_a and weighted mean length L_w of all the TOCNs were determined using the following equations.

$$L_a = \frac{\sum n_i l_i}{\sum n_i} \quad (2.A1)$$

$$L_w = \frac{\sum n_i {l_i}^2}{\sum n_i l_i} \quad (2.A2)$$

where l is the length of the TOCNs, and n is the number of TOCNs. The length distribution histograms of each TOCN as obtained by TEM observations are shown in Figure 2.A1. The polydispersity indices of the TOCNs were in the range of 1.2–1.4 and were lower than that reported in a previous study.[7]

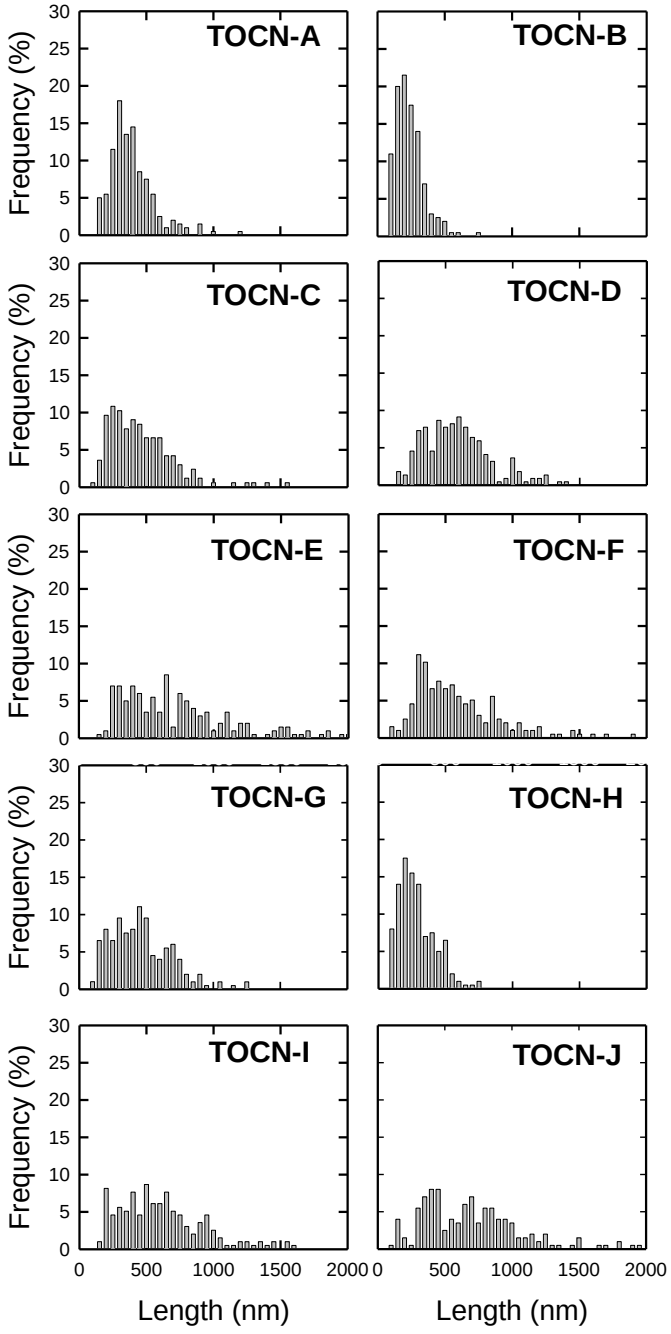

Figure 2.A1. Length distribution histograms of the TOCNs. Reproduction of image with kind permission from Springer Science (© Springer 2014) and Business Media.

2.5.3. Critical concentration *c** of TOCN-A dispersions at 0 and 0.5 mM NaCl

The critical concentrations *c** of TOCN-A dispersions at 0 and 0.5 mM NaCl were 0.07 and 0.085% w/v, respectively. The *c** values were determined following the previously reported method.[17,18]

2.5.4. Relationship between maximum relaxation time τ and weighted mean length L_w

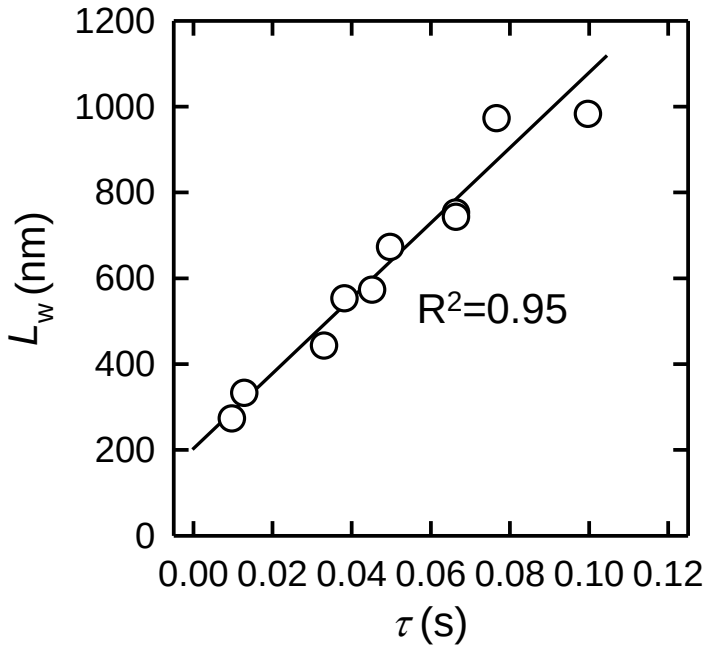

Figure 2.A2. Weighted mean length of TOCNs L_w as a function of maximum relaxation time τ. Reproduction of image with kind permission from Springer Science (© Springer 2014) and Business Media.

2.6. References

1) Ishii, D.; Saito, T.; Isogai, A. Viscoelastic Evaluation of Average Length of Cellulose Nanofibers Prepared by TEMPO-Mediated Oxidation. *Biomacromolecules* **2011**, *12*, 548–550.

2) Ishii, D.; Saito, T.; Isogai, A. Correction to viscoelastic evaluation of average length of cellulose nanofibers prepared by TEMPO-mediated oxidation. *Biomacromolecules* **2012**, *13*, 1706–1706.

3) Araki, J.; Wada, M.; Kuga, S.; Okano, T. Flow properties of microcrystalline cellulose suspension prepared by acid treatment of native cellulose. *Colloids Surf., A* **1998**, *142*, 75–82.

4) Boluk, Y.; Lahiji, R.; Zhao, L.; McDermott, M. T. Suspension viscosities and shape parameter of cellulose nanocrystals (CNC). *Colloids Surf., A* **2011**, *377*, 297–303.

5) Doi, M.; Edwards, S. F., *The theory of polymer dynamics;* Oxford University Press New York, 1986.

6) Parra-Vasquez, A. N. G.; Stepanek, I.; Davis, V. A.; Moore, V. C.; Haroz, E. H.; Shaver, J.; Hauge, R. H.; Smalley, R. E.; Pasquali, M. Simple Length Determination of Single-Walled Carbon Nanotubes by Viscosity Measurements in Dilute Suspensions. *Macromolecules* **2007**, *40*, 4043–4047.

7) Shinoda, R.; Saito, T.; Okita, Y.; Isogai, A. Relationship between Length and Degree of Polymerization of TEMPO-Oxidized Cellulose Nanofibrils. *Biomacromolecules* **2012**, *13*, 842–849.

8) Tanaka, R.; Saito, T.; Isogai, A. Cellulose nanofibrils prepared from softwood cellulose by TEMPO/NaClO/$NaClO_2$ systems in water at pH 4.8 or 6.8. *Int. J. Biol. Macromol.* **2012**, *51*, 228–234.

9) Saito, T.; Isogai, A. TEMPO-mediated oxidation of native cellulose. The effect of oxidation conditions on chemical and crystal structures of the water-insoluble fractions. *Biomacromolecules* **2004**, *5*, 1983–1989.

10) Elazzouzi-Hafraoui, S.; Nishiyama, Y.; Putaux, J.-L.; Heux, L.; Dubreuil, F.; Rochas, C. The Shape and Size Distribution of Crystalline Nanoparticles Prepared by Acid Hydrolysis of Native Cellulose. *Biomacromolecules* **2007**, *9*, 57–65.

11) Saito, T.; Kuramae, R.; Wohlert, J.; Berglund, L. A.; Isogai, A. An ultrastrong nanofibrillar biomaterial: the strength of single cellulose nanofibrils revealed via sonication-induced fragmentation. *Biomacromolecules* **2013**, *14*, 248–253.

12) Okita, Y.; Saito, T.; Isogai, A. Entire surface oxidation of various cellulose microfibrils by TEMPO-mediated oxidation. *Biomacromolecules* **2010**, *11*, 1696–1700.

13) Israelachvili, J. N., *Intermolecular and surface forces: revised third edition;* Academic press: 2011.

14) Araki, J. Electrostatic or steric? - preparations and characterizations of well-dispersed systems containing rod-like nanowhiskers of crystalline polysaccharides. *Soft Matter* **2013**, *9*, 4125–4141.

15) Carr Jr, M. E.; Hermans, J. Size and density of fibrin fibers from turbidity. *Macromolecules* **1978**, *11*, 46–50.

16) Dimic-Misic, K.; Puisto, A.; Gane, P.; Nieminen, K.; Alava, M.; Paltakari, J.; Maloney, T. The role of MFC/NFC swelling in the rheological behavior and dewatering of high consistency furnishes. *Cellulose* **2013**, *20*, 2847–2861.

17) Gericke, M.; Schlufter, K.; Liebert, T.; Heinze, T.; Budtova, T. Rheological properties of cellulose/ionic liquid solutions: from dilute to concentrated states. *Biomacromolecules* **2009**, *10*, 1188–1194.

18) Haward, S. J.; Sharma, V.; Butts, C. P.; McKinley, G. H.; Rahatekar, S. S. Shear and extensional rheology of cellulose/ionic liquid solutions. *Biomacromolecules* **2012**, *13*, 1688–1699.

19) Mason, S. G. The motion of fibres in flowing liquids. *Pulp Pap. Mag. Can.* **1950**, *51*, 93–100.

20) Iwamoto, S.; Lee, S.-H.; Endo, T. Relationship between aspect ratio and suspension viscosity of wood cellulose nanofibers. *Polymer Journal* **2014**, *46*, 73–76.

Chapter 3

Influence of flexibility and dimensions of nanocelluloses on the flow properties of their aqueous dispersions

3.1. Introduction

In the previous section, the maximum relaxation times τ of dilute dispersions of individualized NFCs with a uniform width of ~3 nm were investigated as a function of either surface-charge content or the length of the nanocelluloses.[1] This study revealed that the influence of the surface-charge content on the τ values is negligible in dilute systems, and the τ values show a linear relationship with the length when the width is constant. However, the lengths estimated from the τ values based on a theoretical equation for rotational motions of rigid rod-like polymers were much larger than those measured by microscopic observation. This discrepancy is likely to be caused by the flexibility of NFCs in water. Furthermore, the theoretical equation is defined assuming rigid polymer chains dissolved in liquid,[2] and the volume of solid rods or fibrils are thus not taken into account, which might also cause the discrepancy.

In the present section, the influence of the flexibility and dimensions of nanocelluloses on the flow properties of their dilute dispersions were investigated. The prepared nanocellulose samples were three NCCs (width: 3.8–14.4 nm, aspect ratio: 23–77) and four NFCs (width: 2.6 nm, aspect ratio: 103–376). In addition to the τ values, intrinsic viscosities [η], which are theoretically expressed as a function of volume (and width) of solid rods, of the nanocellulose dispersions were also examined. These seven nanocelluloses, dispersed in water or a water/glycerol mixture, were subjected to shear viscosity measurement to determine the intrinsic viscosity [η] and the maximum relaxation time τ. The experimental values of [η] and τ were then compared with their theoretical values calculated using two equations for the rotational motions of

rigid rods or polymer chains, so that the contributions of the flexibility and dimensions of the nanocelluloses to the flow properties could be assessed.

3. 2. Materials and methods

3.2.1. Materials

Three cellulose samples were used as starting materials: cotton linters, softwood bleached kraft pulp (SBKP), and algal cellulose (*Cladophora* sp.). The cotton linters cellulose was supplied by Advantec Tokyo Co. Ltd., Tokyo, Japan. A never-dried SBKP with a water content of 80% was supplied by Nippon Paper Industries Co. Ltd., Tokyo, Japan. The *Cladophora* fiber was cut into small pieces with scissors and purified according to a previously reported method.[3] Other chemicals of laboratory grade were purchased from Wako Pure Chemicals, Tokyo, Japan and used without further purification.

3.2.2. Preparation of nanocellulose dispersions

All of the nanocellulose dispersions were prepared from the native celluloses via TEMPO-mediated oxidation. Four TEMPO-oxidized cellulose nanofibrils (TOCN-D, -E, -F, and -G) with different average lengths and a nearly uniform width were prepared from SBKP with the TEMPO/NaBr/NaClO system in water at pH 10 or the TEMPO/NaClO/$NaClO_2$ system in water at pH 5 according to a previously reported method,[1] and used as NFCs. Three NCCs were prepared from cotton linters, SBKP, and *Cladophora* cellulose by TEMPO-mediated oxidation and subsequent hydrolysis with hydrochloric acid.[4] First, these starting materials were oxidized with the TEMPO/NaBr/NaClO system in water at pH 10 with 10 mmol NaClO per gram of cellulose. The oxidized celluloses were then hydrolyzed in 2.5 M HCl at 105 °C for 4 h, and centrifuged at 12,000 *g* for 5 min to yield the hydrolysates. After dialysis of the hydrolysates for 5 days, the purified products were sonicated in distilled water at 0.1% w/v for 1–8 min using a Nihon Seiki US-300T ultrasonic homogenizer (300W, 19.5 kHz) at about 10% output power. The resulting NCC dispersions from cotton linters, SBKP, and *Cladophora* cellulose are called acid-hydrolyzed TOCN

(AhTOCN)-A, -B, and -C, respectively. The concentrations of these NCC samples were adjusted to 0.005%–5% w/v by dilution with distilled water and/or condensation using a rotary evaporator. Because the shear viscosities of the AhTOCN-C dispersions were too low to be accurately detected, glycerol was added to the dispersions at a 1:1 ratio by weight to increase their viscosities.[5] The glycerol-mixed AhTOCN-C dispersions were well-homogenized in an ultrasonic bath for 1 min, and then shaken at 150 rpm overnight using a rotary shaker (see Figure 3.A1 in the Appendix for the dispersibility of AhTOCN-C in the water/glycerol mixture). The density and viscosity of the water/glycerol mixture at 25 °C were 1.14 g/mL and 4.44 mPa s, respectively.

3.2.3. Length and width of nanocelluloses

The lengths of isolated ~200 nanocellulose elements were measured using a transmission electron microscope (TEM) (JEOL JEM 2000-EXII, Tokyo, Japan) at an accelerating voltage of 200 kV.[1] The weighted mean length L_w values of the nanocelluloses were calculated from their length distribution histograms (see Eq. 3.A1 and Figure 3.A2 in the Appendix). Then, the widths of isolated ~30 nanocellulose elements were measured by atomic force microscopy (AFM) according to a previously reported method (see Appendix, Figure 3.A3),[6] and the weighted mean width d_w values of the nanocelluloses were calculated in a similar manner to the L_w values.

3.2.4. Shear viscosity measurement

Shear viscosity measurements of the dilute nanocellulose dispersions were conducted at 25 °C using a rheometer (MCR 302, Anton Paar GmbH, Graz, Austria) according to a previously reported method (see Table 3.A1 in the Appendix for their critical concentration c^*, or the boundary concentration between the dilute and semi-dilute regime).[1] The shear viscosities were measured using a cone-plate geometry (plate diameter: 50 mm, angle: 2°) at a shear rate $\dot{\gamma}$ from 1 to 1000 s^{-1}. The experimental maximum relaxation time τ_e of the dispersions was determined as the inverse of the critical shear rate $\dot{\gamma}_{crit}$, or the shear rate at

the beginning of shear-thinning (see Appendix, Figure 3.A4).[7,8] The experimental intrinsic viscosity $[\eta]_e$ was determined by applying the relative viscosity (the ratio of shear viscosity to solvent viscosity) to the Fedors plot given by

$$\frac{1}{2(\eta_{rel}{}^{1/2}-1)} = \frac{1}{[\eta]_e}\left(\frac{1}{c}-\frac{1}{c_m}\right) \tag{3.1}$$

where η_{rel} is the relative viscosity, c is the solid concentration, and c_m is the maximum packing density (see Appendix, Figure 3.A5 and Table 3.A2).[9,10]

3.2.5. Theoretical equation for maximum relaxation time

The theoretical maximum relaxation time τ_t was calculated by inserting the L_w and d_w values of the nanocellulose into the following equation for the rotational motions of rigid rod-like polymers in dilute region:[2]

$$\tau_t = \frac{1}{6D_r} = \frac{\pi\eta_s L^3}{18k_B T\left[\ln\left(L/d\right)-\gamma\right]} \tag{3.2}$$

where D_r is the rotational diffusion constant, T is the absolute temperature, η_s is the solvent viscosity, and k_B is the Boltzmann constant. The γ value is derived from the hydrodynamic interaction assuming rotational motions of rigid rods in the dilute region, and defined as follows:[11]

$$\gamma = 1.57 - 7\left(\frac{1}{\ln\left(L/R\right)}-0.28\right)^2 \tag{3.3}$$

where R is the radius (d/2) of the rod or nanocellulose.

3.2.6. Theoretical equation for intrinsic viscosity

The theoretical intrinsic viscosity $[\eta]_t$ was calculated by inserting the L_w and d_w values of the nanocellulose into the following equation for the rotational motions of rigid rods in the dilute region:[2,7]

$$[\eta]_t = \frac{2\pi L^3}{45\left(\ln\left(L/d\right)-\gamma\right)}\frac{1}{\rho\pi R^2 L} \tag{3.4}$$

where ρ is the density of the rod or the nanocellulose (1.6 g/cm^3). In Eq. 3.4, the volume of the rod ($\pi R^2 L$) is taken into account, which is a significant difference to Eq. 3.2.

3.3. Results and discussion

3.3.1. Dimensions of nanocelluloses

The three NCCs (AhTOCN-A, -B, and -C) had different average lengths and widths depending on the starting material (Table 3.1). The average lengths and widths of the AhTOCNs were L_w = 138–1105 nm and d_w = 3.8–14.4 nm. The TEM images of these AhTOCNs show straight rod-like morphologies (Figure 3.1). The four NFCs (TOCN-D, -E, -F, and -G) had different average lengths of 267–977 nm and a uniform width of 2.6 nm.[6] In the TEM images (Figure 3.1), the fibers of the longer TOCNs, such as TOCN-G, are curved and contain kinks.

Table 3.1. Summary of the average length L_w, average width d_w, and aspect ratio p of the nanocelluloses. Reproduced with kind permission from American Chemical Society (© American Chemical Society 2015).

		starting material	L_w (nm)	d_w (nm)	p
AhTOCN	A	cotton linters	138	6.1	23
	B	SBKP	168	3.8	45
	C	*Cladophora*	1105	14.4	77
TOCN	D	SBKP	267	2.6	103
	E	SBKP	333	2.6	128
	F	SBKP	551	2.6	212
	G	SBKP	977	2.6	376

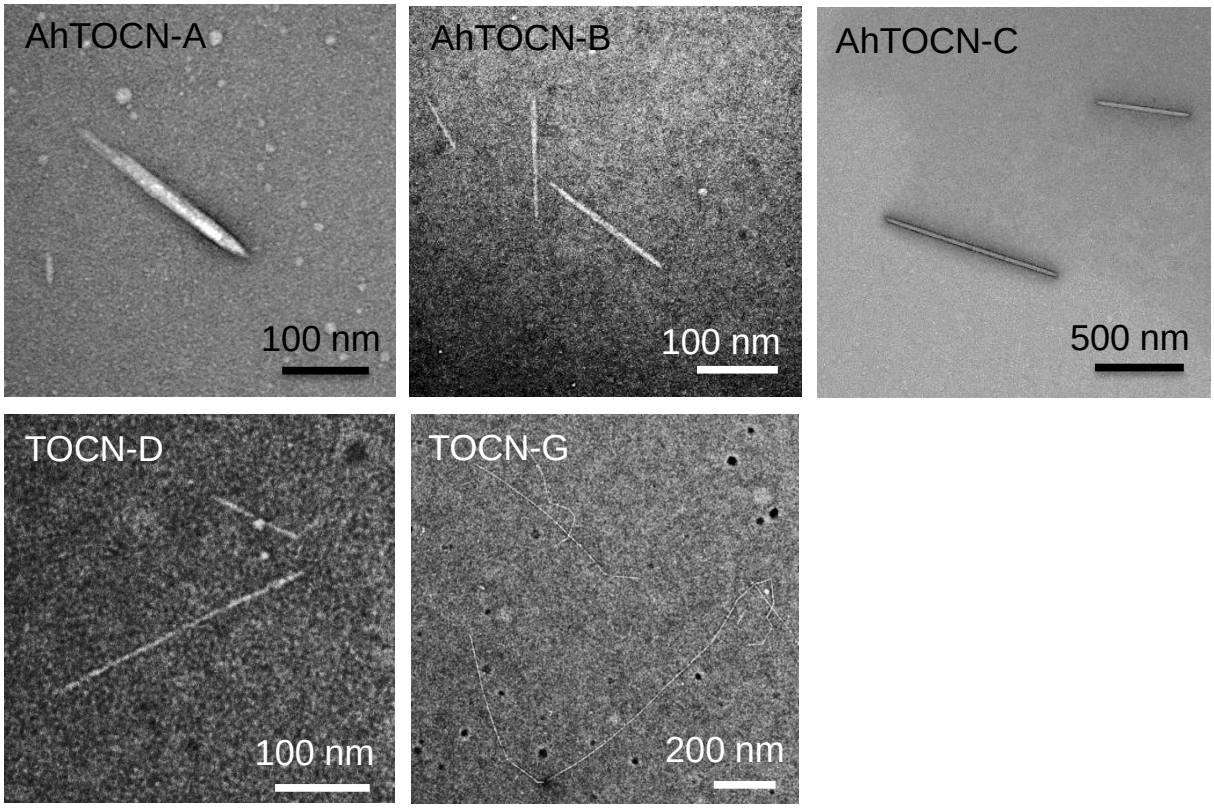

Figure 3.1. TEM images of the nanocelluloses. Reproduced with kind permission from American Chemical Society (© American Chemical Society 2015).

3.3.2. Maximum relaxation time of nanocellulose dispersions

The experimental maximum relaxation time τ_e of the nanocellulose dispersions was determined by shear viscosity measurement, and compared with their theoretical maximum relaxation time τ_t calculated using Eq. 3.2 for rotational motions of rod-like polymers. The τ_e values were obtained as the inverse of the critical shear rates $\dot{\gamma}_{crit}$ (the shear rate at the beginning of shear-thinning) (see Figure 3.A4).[1]

Figure 3.2 shows the relationship between τ_e and τ_t of the nanocellulose dispersions. The τ_e values of the TOCNs with a uniform width of 2.6 nm showed a linear relationship with τ_t values.[1] However, the τ_e values of 0.01–0.1 s for the TOCNs (d_w = 2.6 nm) were much larger than their τ_t values of 0.00024–0.008 s. This discrepancy between the τ_e and τ_t values is probably caused by the length distributions of the TOCNs (see Figure. 3.A2).[1] Parra-Vasquez *et al.* reported that the length distributions of rods influence the shear viscosities of their dilute dispersions,[5] because longer rods begin to align with the shear flow at low shear

rate, and dispersions of rods with a range of lengths show a broad transition from the Newtonian region to shear-thinning. Thus, the estimated τ_e values of TOCN dispersions with a range of fiber lengths are likely to be larger than the τ_t values.

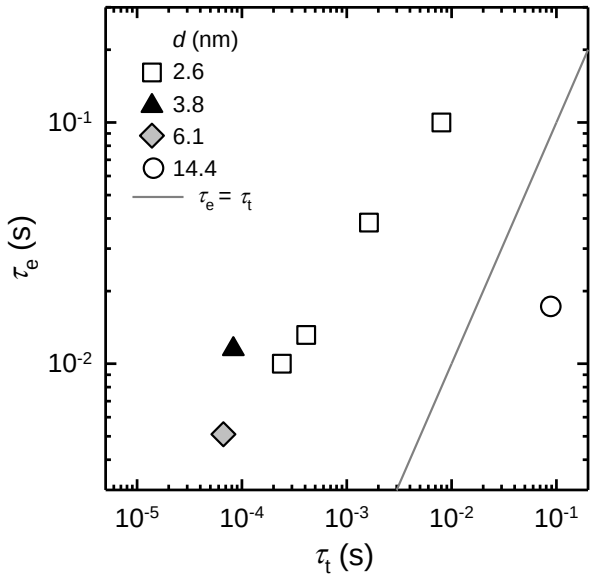

Figure 3.2. Relationship between experimental maximum relaxation time τ_e and theoretical maximum relaxation time τ_t of the nanocellulose dispersions. Reproduced with kind permission from American Chemical Society (© American Chemical Society 2015).

The τ_e values of the AhTOCN dispersions (d_w = 3.8–14.4 nm) showed a different trend to those for the TOCN dispersions (Figure 3.2). In particular, the τ_e value of the AhTOCN-C dispersion (d_w = 14.4 nm) was very far from the linear relationship determined for the TOCNs. This is probably because the fibrils of AhTOCN-C had extremely thicker widths and larger volumes than the other nanocelluloses (Table 3.1), and the volumes of the nanocelluloses are not taken into account in Eq. 3.2 used for the calculation of the τ_t value. These results suggest that the maximum relaxation times of nanocellulose dispersions are strongly influenced by the dimensions of the nanocellulose fibrils.

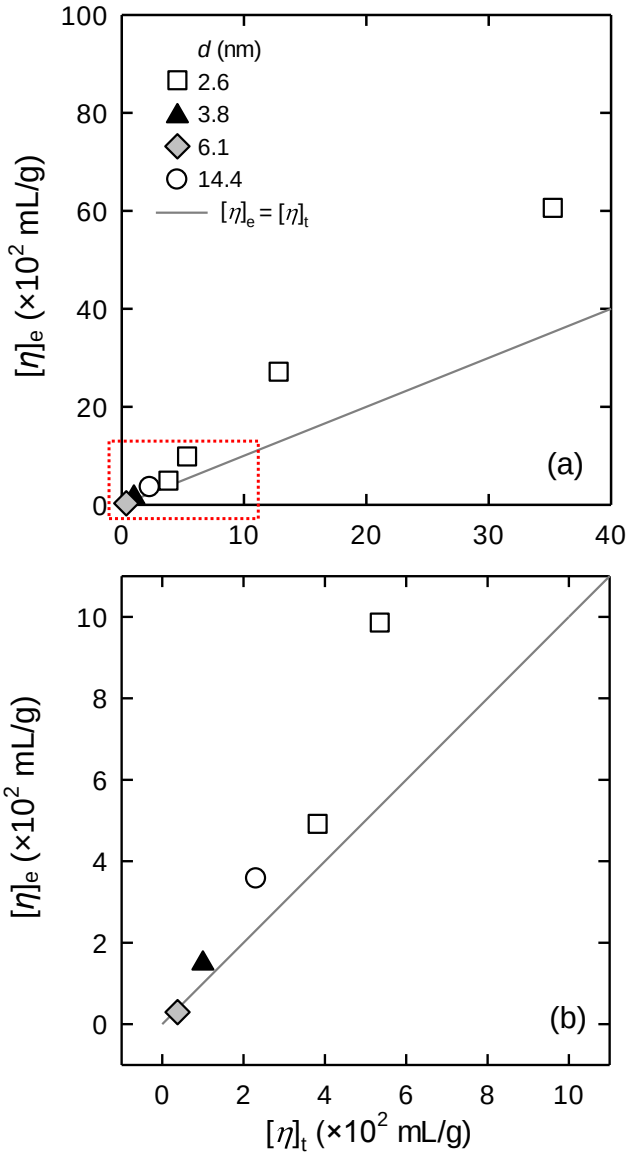

Figure 3.3. (a) Relationship between experimental intrinsic viscosity $[\eta]_e$ and theoretical intrinsic viscosity $[\eta]_t$ of the nanocellulose dispersions and (b) enlarged portion of the figure indicated by the red dotted rectangle in (a). Reproduced with kind permission from American Chemical Society (© American Chemical Society 2015).

3.3.3. Intrinsic viscosity of nanocellulose dispersions

The experimental intrinsic viscosities of the nanocellulose dispersions were determined by applying the relative viscosities to the Fedors plot (Figure 3.A5 and Table 3.A2) and compared with their theoretical intrinsic viscosities calculated using Eq. 3.4. It should be noted that, in contrast to Eq. 3.2, Eq. 3.4 takes

into account the volume of the nanocellulose (the parameter $\pi R^2 L$, see Materials and Methods section). Figure 3.3a shows the relationship between $[\eta]_e$ and $[\eta]_t$. In the case of the nanocelluloses with low aspect ratios of 23–103 (see Table 3.1, AhTOCNs and TOCN-D), their $[\eta]_e$ values (29–492 mL/g, see Table 3.A2) are in good agreement with their $[\eta]_t$ values (38–382 mL/g) irrespective of their widths (Figure 3.3b). This result shows that under shear flow the nanocelluloses with low aspect ratios of 23–103 actually behave like rigid rods, as observed in the TEM images (Figure 3.1).

The $[\eta]_e$ values for high-aspect-ratio nanocelluloses (TOCN-E, F, G) ranged from 986 to 6060 mL/g (see Table 3.A2), which are larger than their $[\eta]_t$ values of 535–3524 mL/g (Figure 3.3a). This discrepancy between the $[\eta]_e$ and $[\eta]_t$ values can be explained based on the curves and kinks of the fibrils, that is, the flexibility of the high-aspect-ratio nanocelluloses, as described in the following two paragraphs:

(1) Aspect ratios versus flexibility. Switzer and Klingenberg reported that the fiber flexibility under shear flow can be described as the effective stiffness S_e:[12]

$$S_e = E_Y I / \eta_s \dot{\gamma} L^4 \tag{3.5}$$

where E_Y is Young's modulus of the fiber and I is the cross-sectional second moment of the area of the fiber ($\pi d^4/64$). Equation 3.5 is thus expressed using the fiber width d as follows:

$$S_e = \frac{E_Y \pi}{64 \eta_s \dot{\gamma}} \left(\frac{d}{L}\right)^4 \tag{3.6}$$

According to Eq. 3.6, the S_e value is exponentially proportional to the inverse of the aspect ratio. Thus, as the aspect ratio increases, the S_e value decreases, or the fiber becomes flexible.

(2) Flexibility versus intrinsic viscosity. The flexibility of fibers contributes to an increase in the intrinsic viscosity of the fiber suspensions.[12,13] Because flexible fibers in suspension under shear flow produce stronger hydrodynamic forces than rigid fibers, flexible-fiber suspensions show higher intrinsic viscosities than rigid-fiber suspensions.

Therefore, high-aspect-ratio fibers with flexibility have higher intrinsic viscosity in dispersion than low-aspect-ratio fibers with rigidity. This explains why the $[\eta]_e$ values of TOCN-E, -F, and -G with high

aspect ratios of 128–376 (see Table 3.1) were estimated to be larger than their $[\eta]_t$ values calculated assuming rigid rods.

3.3.4. Relationship between intrinsic viscosity and aspect ratio

To take the flexibility of the nanocellulose into account for the intrinsic viscosity, the $[\eta]_e$ values were plotted as a function of their aspect ratio p (Figure 3.4). The $[\eta]_e$ values are exponentially proportional to the p values, and the linear relationship in the log–log plot is

$$\rho[\eta]_e = 0.15 \times p^{1.9} \tag{3.7}$$

where the density of the nanocellulose ρ is involved to make the intrinsic viscosity $[\eta]_e$ dimensionless. In this empirical equation, the flexibility of the nanocellulose should correspond to the exponent 1.9, considering the following general description of intrinsic viscosity $[\eta]$ for polymer solutions:

$$[\eta] = KM^a \tag{3.8}$$

where M is the molecular weight, K is a constant, and a is a parameter that reflects chain expansion. This is well known as the Mark–Houwink–Sakurada equation. The exponent a for semi-flexible polymers appears to be greater than 1.2, and asymptotically approaches 2 with increasing rigidity of the polymers.[14]

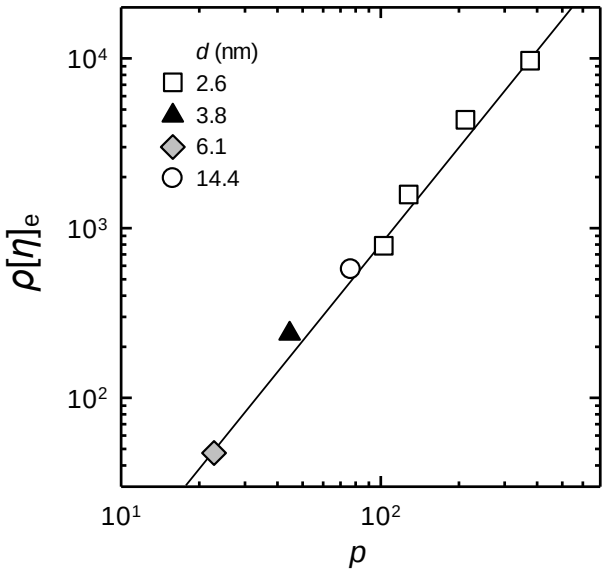

Figure 3.4. Experimental intrinsic viscosity $[\eta]_e$ of the nanocellulose dispersions as a function of aspect ratio p. ρ is the density of the nanocellulose. Reproduced with kind permission from American Chemical Society (© American Chemical Society 2015).

3.4. Conclusions

The influence of the flexibility and dimensions of nanocelluloses on the flow properties of their dilute dispersions was investigated by experimental and theoretical approaches using rod-like NCCs and spaghetti-like NFCs. The maximum relaxation time τ of the nanocellulose dispersions was strongly influenced by their dimensions, such as widths and length distributions. Thus, the experimentally determined τ values for the solid nanocelluloses did not agree with the theoretically calculated values assuming rotational motions of monodisperse rigid polymers dissolved in liquid. The intrinsic viscosities of the nanocelluloses with low aspect ratios were in good agreement with the theoretically predicted values assuming solid rigid rods. However, the $[\eta]$ values for high-aspect-ratio nanocelluloses were larger than the theoretical values. This discrepancy for the high-aspect-ratio nanocelluloses can be explained based on the flexibility of the nanocelluloses; as the aspect ratios of nanocelluloses increase, they become more flexible and their dispersions have higher intrinsic viscosity. When the $[\eta]$ values were plotted against

aspect ratio p of the nanocelluloses to take into account the flexibility, the relationship between $[\eta]$ and p values was $\rho[\eta] = 0.15 \times p^{1.9}$ irrespective of the flexibility and dimensions of the nanocelluloses. Thus, the average lengths of nanocelluloses, including NCCs and NFCs, can be simply determined using this empirical equation by measuring the $[\eta]$ values of their dispersions.

3.5. Appendix

3.5.1. Dispersibility of AhTOCN-C in water/glycerol mixture

The dispersibility of AhTOCN-C in a water/glycerol mixture was evaluated by birefringence and turbidity measurements of the dispersion. The 0.11% w/v AhTOCN-C dispersion in water/glycerol mixture showed clear birefringence at rest, similar to pure water (Figure 3.A1a). In addition, the turbidity of the water/glycerol dispersion was almost the same as that of the water dispersion (Figure 3.A1b). These results show that AhTOCN-C was dispersed without agglomeration even in the water/glycerol mixture.

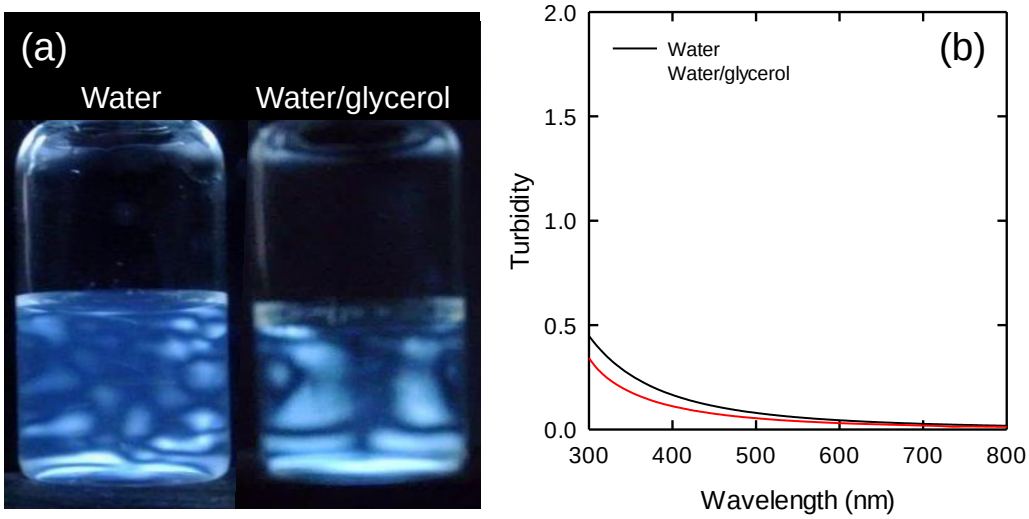

Figure 3.A1. (a) Birefringence images and (b) turbidity of 0.11% w/v AhTOCN-C dispersions taken between crossed polarizers. Reproduced with kind permission from American Chemical Society (© American Chemical Society 2015).

3.5.2. Weighted mean length L_w, weighted mean width d_w, and length distribution histogram

The weighted mean length L_w values of the nanocelluloses were calculated using the following equation:

$$L_w = \frac{\sum n_i {l_i}^2}{\sum n_i l_i} \qquad (3.A1)$$

where l_i is the length of nanocellulose and n_i is its number. The weighted mean width d_w values were calculated in the same way. The length and width values of the AhTOCNs were measured in the TEM and AFM images, respectively (Figures 3.A2 and 3.A3). The values of the TOCNs were taken from previously reported papers by our group.[1,6]

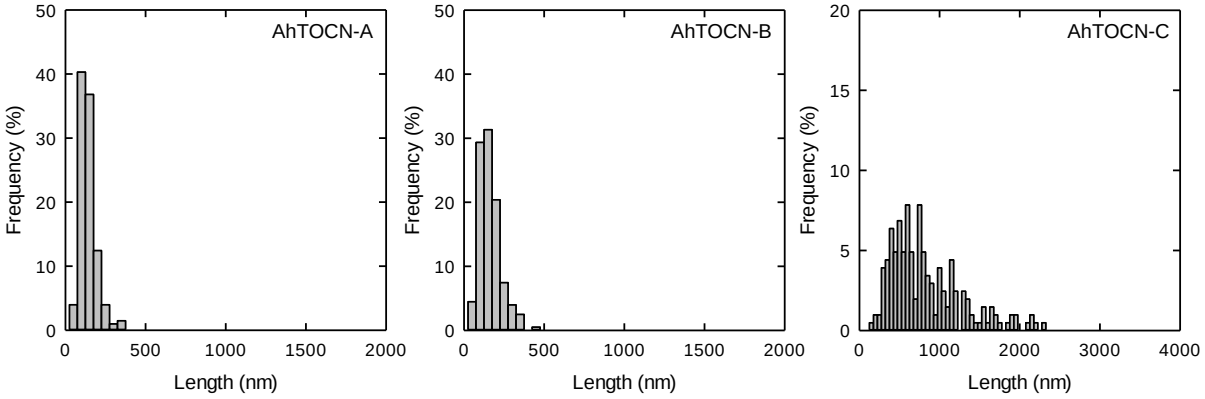

Figure 3.A2. Length distribution histograms for AhTOCNs. Reproduced with kind permission from American Chemical Society (© American Chemical Society 2015).

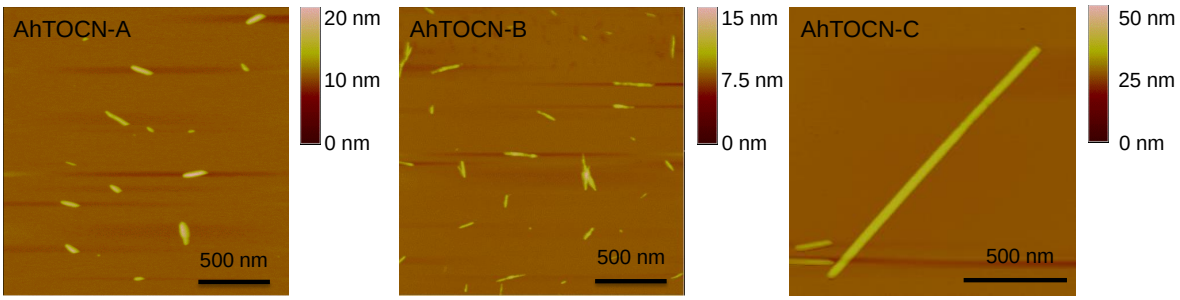

Figure 3.A3. AFM images of AhTOCNs. Reproduced with kind permission from American Chemical Society (© American Chemical Society 2015).

3.5.3. Determination of critical concentration *c** and experimental maximum relaxation time τ_e of nanocellulose dispersions

The critical concentration *c**, or the boundary concentration between the dilute and semi-dilute regions of the nanocellulose dispersions, was determined according to a previously reported method (Table 3.A1).[1] Then, the τ_e values of the nanocellulose dispersions at concentrations less than *c** were obtained as the inverse of the critical shear rate $\dot{\gamma}_{crit}$, or the shear rate at the beginning of shear-thinning.

Table 3.A1. Critical concentration *c** of the nanocellulose dispersions. Reproduced with kind permission from American Chemical Society (© American Chemical Society 2015).

	AhTOCN			TOCN			
	A	B	C	D	E	F	G
*c** (% w/v)	4.40	0.74	0.10	0.26	0.14	0.04	0.01

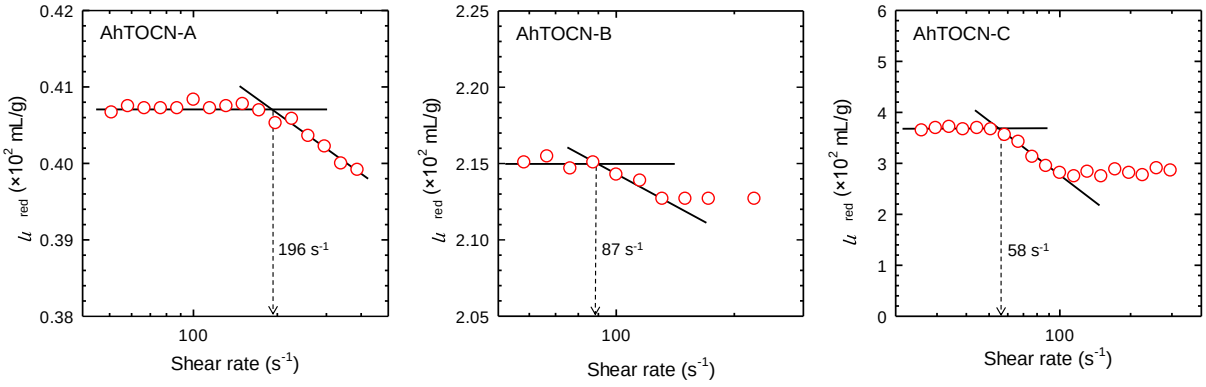

Figure 3.A4. Reduced viscosity η_{red} of the AhTOCN dispersions as a function of shear rate. The values of the TOCN dispersions were taken from our previous paper.[1] Reproduced with kind permission from American Chemical Society (© American Chemical Society 2015).

3.5.4. Determination of experimental intrinsic viscosity $[\eta]_e$

The experimental intrinsic viscosities of the dilute nanocellulose dispersions were calculated by applying their relative viscosities obtained by shear viscosity measurement to the Fedors plot (Figure 3.A5 and Table 3.A2). The intrinsic viscosity corresponds to the inverse of the slope of the Fedors plot.

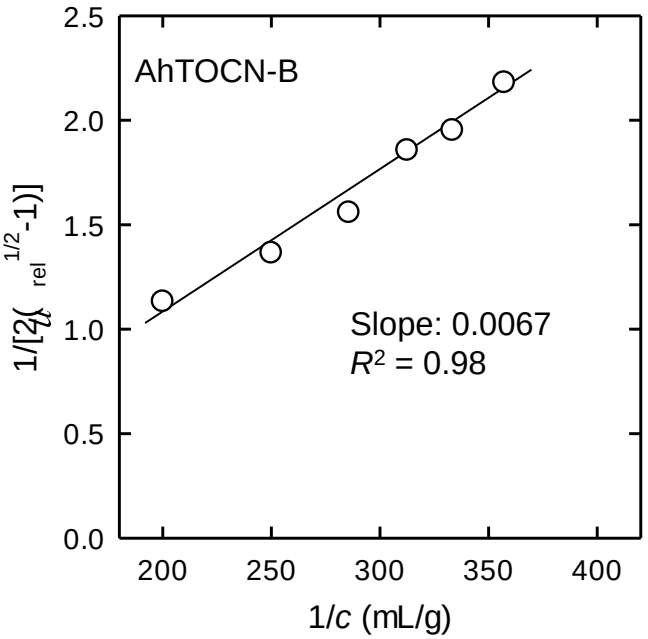

Figure 3.A5. Typical Fedors plot of one of the nanocellulose dispersions. Reproduced with kind permission from American Chemical Society (© American Chemical Society 2015).

Table 3.A2. Experimental intrinsic viscosity $[\eta]_e$ values of the nanocellulose dispersions. Reproduced with kind permission from American Chemical Society (© American Chemical Society 2015).

	AhTOCN			TOCN			
	A	B	C	D	E	F	G
$[\eta]_e$ (mL/g)	29	150	357	492	986	2717	6060

3.6. References

1) Tanaka, R.; Saito, T.; Ishii, D.; Isogai, A. Determination of nanocellulose fibril length by shear viscosity measurement. *Cellulose* **2014**, *21*, 1581–1589.

2) Doi, M.; Edwards, S. F., *The theory of polymer dynamics;* Oxford University Press New York, 1986.

3) Okita, Y.; Saito, T.; Isogai, A. Entire surface oxidation of various cellulose microfibrils by TEMPO-mediated oxidation. *Biomacromolecules* **2010**, *11*, 1696–1700.

4) Salajková, M.; Berglund, L. A.; Zhou, Q. Hydrophobic cellulose nanocrystals modified with quaternary ammonium salts. *J. Mater. Chem.* **2012**, *22*, 19798–19805.

5) Parra-Vasquez, A. N. G.; Duque, J. G.; Green, M. J.; Pasquali, M. Assessment of length and bundle distribution of dilute single‐walled carbon nanotubes by viscosity measurements. *AIChE J.* **2014**, *60*, 1499–1508.

6) Saito, T.; Kuramae, R.; Wohlert, J.; Berglund, L. A.; Isogai, A. An ultrastrong nanofibrillar biomaterial: the strength of single cellulose nanofibrils revealed via sonication-induced fragmentation. *Biomacromolecules* **2013**, *14*, 248–253.

7) Parra-Vasquez, A. N. G.; Stepanek, I.; Davis, V. A.; Moore, V. C.; Haroz, E. H.; Shaver, J.; Hauge, R. H.; Smalley, R. E.; Pasquali, M. Simple length determination of single-walled carbon nanotubes by viscosity measurements in dilute suspensions. *Macromolecules* **2007**, *40*, 4043–4047.

8) Kulicke, W.-M.; Kniewske, R. The shear viscosity dependence on concentration, molecular weight, and shear rate of polystyrene solutions. *Rheol. acta* **1984**, *23*, 75–83.

9) Bercea, M.; Navard, P. Shear dynamics of aqueous suspensions of cellulose whiskers. *Macromolecules* **2000**, *33*, 6011–6016.

10) Fedors, R. F. An equation suitable for describing the viscosity of dilute to moderately concentrated polymer solutions. *Polymer* **1979**, *20*, 225–228.

11) Broersma, S. Rotational diffusion constant of a cylindrical particle. *J. Chem. Phys.* **1960**, *32*, 1626–1631.

12) Switzer III, L. H.; Klingenberg, D. J. Rheology of sheared flexible fiber suspensions via fiber-level simulations. *J. Rheol.* **2003**, *47*, 759–778.

13) Tozzi, E. J.; Klingenberg, D. J.; Scott, C. T. Correlation of fiber shape measures with dilute suspension properties. *Nord. Pulp Pap. Res. J.* **2008**, *23*, 369–373.

14) Mansfield, M. L.; Douglas, J. F. Transport properties of rodlike particles. *Macromolecules* **2008**, *41*, 5422–5432.

Chapter 4
Viscoelastic properties of core–shell-structured, hemicellulose-rich nanofibrillated cellulose in dispersion and wet film states

4.1. Introduction

Bioinspired core–shell-structured NFCs have attracted much attention for the production of high-performance NFC-based materials. Core–shell-structured NFCs are mainly prepared from bleached wood pulps by mechanical disintegration treatments in water using enzymatic or chemical pretreatments,[1,2] followed by adsorption of polysaccharides such as hemicelluloses,[3–5] starches,[6] and cellulose derivatives.[7–9] The core and shell structures of these NFCs correspond to dispersed cellulose fibrils and swollen soft polysaccharides, respectively. These core–shell-structured NFCs have better hygromechanical properties[2,3,4,6] and oxygen-barrier properties[2] than neat NFCs.

Core–shell-structured and neat NFCs are both prepared as water dispersions. An understanding of their rheological properties is therefore important in the production of NFC-based materials. Many studies of the rheological properties of neat NFC dispersions, in terms of aspect ratio,[10–12] disintegration conditions,[11,13,14] solid concentration,[15–23] ionic strength,[17,18,23–26] pH,[15,17,21,26,27] and temperature,[15,28] have been performed. However, the rheological properties of the core–shell-structured NFC dispersions are not yet fully understood.[29] Core-shell-structured NFCs have surface layers of swollen soft polysaccharides, therefore their rheological properties differ substantially from those of neat NFCs.

In the present study, the viscoelastic properties of bulk core–shell-structured, hemicellulose-rich NFC dispersions were investigated, and correlated with the solid-state viscoelastic behaviors of wet thin NFC films. A hemicellulose-rich NFC with a low amount of surface charged groups (hemicellulose neutral sugars 23% w/w, carboxylate 0.2 mmol g^{-1}) was isolated from Japanese persimmons. Its behavior was

compared with that of a highly charged carboxylate-rich NFC with a low amount of hemicelluloses (hemicellulose neutral sugars 7% w/w, carboxylate 0.9 mmol g^{-1}), which was prepared from softwood bleached kraft pulp (SBKP) by 2,2,6,6-tetramethylpiperidine-1-oxyl (TEMPO)-mediated oxidation. The bulk dynamic viscoelastic properties of these two NFC dispersions were compared, using a stress-controlled rheometer, at a range of solid concentrations, salt concentrations, and pH values. The swelling behaviors[30,31] and changes in the solid-state rheologies[32,33] of wet NFC films were also assessed as a function of salt concentration and pH, using a quartz-crystal microbalance with dissipation (QCM-D).

4.2. Materials and Methods

4.2.1. Materials

Japanese persimmons (*Dirospyros kaki*) were purchased at a local grocery store, and processed using a blender for 1 min. Pectin was removed by adjusting the pH of the resulting persimmon suspension (500 mL) to ~3 by dropwise addition of 6 M hydrochloric acid solution, heating at 105 °C for 1.5 h, and washing with distilled water by centrifugation.[34] The persimmon sample was stirred in a 90% v/v acetone/water mixture (1 L) at room temperature for 2 d, bleached with 0.7% $NaClO_2$ solution at pH 4.5 and 75 °C for 2 h,[35] and washed well with distilled water. A never-dried SBKP with an 80% water content was supplied by Nippon Paper Industries (Tokyo, Japan). Other chemical reagents, purchased from Wako Pure Chemical Industries Ltd. (Tokyo, Japan) and the Sigma-Aldrich Co. (St. Louis, MO, USA), were laboratory grade.

4.2.2. Preparation of hemicellulose-rich and carboxylate-rich NFCs

Hemicellulose-rich NFC was prepared from the purified persimmon sample by sonication in distilled water for 4 min at a solid content of 0.1%. Carboxylate-rich NFC was prepared from SBKP by TEMPO-mediated oxidation and subsequent sonication. The SBKP oxidation was conducted at pH 5 and 40 °C, according to a previously reported method,[36] and the oxidized pulp was sonicated in distilled water

for 4 min at a solid content of 0.1%. After centrifugation, the carboxylate-rich NFC dispersion was collected as the supernatant. NFC dispersions (0.05–1.4% w/w) were prepared by dilution or by condensation in a glass or perfluoroalkoxy copolymer resin (Teflon® PFA) recovery flask using a rotary evaporator. NFC dispersions containing 0–100 mM NaCl were prepared by adding 0.25 M NaCl solution to samples of both types of NFC, followed by homogenization in an ultrasonic bath for 4 min. The pH values of some of the NFC dispersions were changed using 0.01 M HCl or 0.5 M NaOH solution.[21]

4.2.3. Dynamic viscoelastic measurement

Dynamic viscoelastic measurements were performed on the NFC dispersions, using a stress-controlled rheometer (MCR 302, Anton Paar GmbH, Graz, Austria), at 25 °C. The dynamic viscoelasticities of the 0.25–0.4% w/w dispersions were determined using a cone-plate geometry (plate diameter 50 mm, angle 2°), and those of the 0.6–1.4% w/w dispersions were determined using a parallel-plate geometry (plate diameter 25 mm). Strain sweep measurements were performed at a strain γ of 0.01–1000% and frequency 1 Hz; the γ values used in the subsequent frequency sweep measurements were determined to 1% and 0.5% for the 0.25–0.4% w/w and 0.6–1.4% w/w NFC dispersions, respectively (see Appendix, Figure 4.A1). Frequency sweep measurements were then conducted at an angular frequency ω of 0.1–100 rad s^{-1}.

4.2.4. Quartz Crystal Microbalance with Dissipation (QCM-D) measurement

The swelling and the water uptake abilities of thin NFC films were studied, using a Q-Sense E4 instrument (Q-Sense AB., Göthenburg, Sweden) at 25 °C. The mass changes at the solid/liquid interface caused by factors such as swelling or de-swelling were measured *in situ* using the QCM-D technique. The general interpretation of QCM-D data is described in the literature.[37–39] AT-cut quartz crystals coated with silica (fundamental resonance frequency f_0 = 5 MHz) were used as QCM-D sensors. The neat QCM-D sensors were cleaned with UV/ozone and soaked in a 0.1 wt% polyethylene-imine (PEI) solution (30 wt%,

M_w = 70 000 g mol^{-1}) for 30 min.[40] The 0.05% w/w hemicellulose-rich or 0.1% w/w carboxylate-rich NFC dispersion was spin-coated on the PEI-adsorbed QCM-D sensor at 3000 rpm for 45 s,[30] and dried in an oven at 80 °C for 10 min, resulting in the formation of a thin and homogeneous NFC film on the QCM-D sensor [see Appendix, Figure 4.A2 for atomic force microscopy (AFM) images of the QCM-D sensor surfaces]. The NFC-coated QCM-D sensors were placed in the flow modules of the Q-Sense E4 instrument; 10–100 mM citrate, phosphate, or bicarbonate–carbonate buffers (pH 3–10) were injected into the flow modules at a flow rate of 100 µL min^{-1}. The changes in frequency Δf and dissipation ΔD of the QCM-D sensors at f_0 = 5 MHz (n = 1) and six different overtones of 15, 25, 35, 45, 55, and 65 MHz (n = 3, 5, 7, 9, 11, and 13, respectively), were monitored for 120 min using QSoft 401 software. The obtained Δf and ΔD curves for multiple overtones (15, 25, and 35 MHz; 25, 35, and 45 MHz; 35, 45, and 55 MHz) were fitted to a Voigt-based viscoelastic model,[41] using Q-Tools ver. 3 software, and the shear modulus μ_f and hydrodynamic thickness h_f of the wet NFC film at the end of the measurements were estimated.[32,33,42] The fitting parameters of the fluid density ρ_0, fluid viscosity η_0, and layer density ρ_f were assumed to be 1000 kg m^{-3}, 0.001 kg m^{-1} s^{-1}, and 1200 kg m^{-3}, respectively.[33,42]

4.2.5. Analyses

The carboxylate contents of the NFC samples were determined using an electric conductivity titration method.[43] The lengths of ~100 fibrils for each NFC were measured using a transmission electron microscope (TEM), and the arithmetic mean lengths L_a and the weighted mean lengths L_w of the NFCs were calculated as follows:

$$L_a = \frac{\sum_{i=1}^{n} l_i}{n} \tag{4.1}$$

$$L_w = \frac{\sum_{i=1}^{n} {l_i}^2}{\sum_{i=1}^{n} l_i} \tag{4.2}$$

where l_i is the fibril length. The thicknesses of ~40 fibrils for each NFC were measured by AFM, using a NanoScope V MultiMode 8 (Bruker Nano Inc., Santa Barbara, CA, USA) instrument equipped with a

Bruker ScanAsyst-Fluid+ tip, in PeakForce quantitative nanomechanical mapping mode in water. The NFC specimens were prepared by deposition of 0.1% w/v poly-L-lysine solution (20 μL) on freshly exfoliated mica plates for 3 min, followed by deposition of 0.0005% NFC dispersions (20 μL) for 1 min, and observed by AFM without drying. The largest thickness along each individual fibril was taken as the true fibril thickness,[44] and the arithmetic mean thicknesses d_a and weighted mean thicknesses d_w of the NFCs were then calculated in the same way as the L_a and L_w values, respectively. The neutral sugar compositions of the NFC samples were determined using a high-performance liquid chromatography system at 50 °C.[45] The X-ray diffraction (XRD) patterns of the NFC samples were recorded by the reflection method using a Rigaku RINT 2000 instrument with monochromator-filtered Cu Kα radiation (λ = 0.15418 nm) at 40 kV and 40 mA,[8] and the crystal thicknesses d_c of the (2 0 0) plane were calculated using Scherrer's equation.[46]

4.3. Results and Discussion

4.3.1. Characterization of the NFCs

Neutral sugar composition analysis showed that the hemicellulose neutral sugar contents of the hemicellulose-rich and carboxylate-rich NFC samples were 23% w/w and 7% w/w, respectively (Table 4.1, and Appendix, Table 4.A1). Their carboxylate contents were 0.2 and 0.9 mmol g^{-1}, respectively. The hemicellulose-rich and carboxylate-rich NFCs were both well dispersed as individual fibrils (Figure 4.1a and 4.1c), and had weighted mean lengths L_w of 1526 and 1050 nm, respectively.

The weighted mean fibril thickness d_w of the hemicellulose-rich NFC, determined by AFM, was 4.2 nm, and was significantly larger than that of the carboxylate-rich NFC (3.3 nm) (Table 4.1, and Figure 4.1b and 4.1d). The crystallite thickness d_c, or the average size of the crystalline core parts of the fibrils, of the hemicellulose-rich NFC (2.3 nm) was almost the same as that of the carboxylate-rich NFC (2.5 nm) (Table 4.1, and Appendix, Figure 4.A3). These results show that the fibril surfaces of the hemicellulose-rich NFC were surrounded by a soft hemicellulose layer, as reported in the literature.[4,5,46]

The dispersion of carboxylate-rich NFCs is kinetically stabilized by electric double-layer repulsion between the fibrils,[47] whereas the contribution of steric repulsion between the surface hemicelluloses to the colloidal stability of hemicellulose-rich NFC dispersions is significant.[48] It has been reported that NFCs with low amounts of both carboxylate groups and hemicelluloses are not dispersed as individual fibrils.[49]

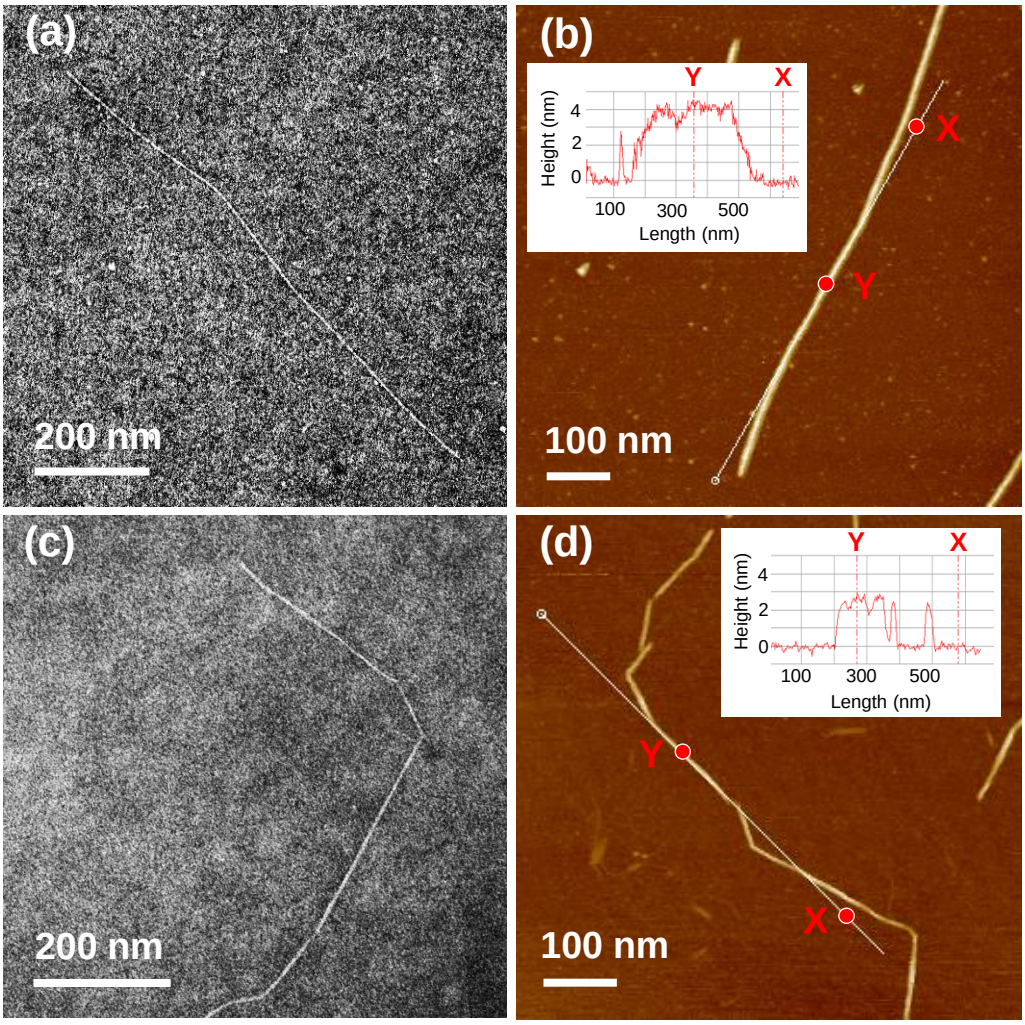

Figure 4.1. TEM images and height AFM images of (a, b) hemicellulose-rich and (c, d) carboxylate-rich NFCs.

Table 1. Summary of properties of hemicellulose-rich and carboxylate-rich NFCs.

	L_w [A] (nm)	L_a [B] (nm)	d_c [C] (nm)	d_w [D] (nm)	d_a [E] (nm)	Content of hemicellulose neutral sugars (%)	Carboxylate content (mmol g^{-1})
Hemicelulose-rich NFCs	1526	1262±580	2.3	4.2	4.2±0.3	23	0.2
Carboxylate-rich NFCs	1050	796±451	2.5	3.3	3.3±0.3	7	0.9

[A] Weighted mean length; [B] arithmetic mean length; [C] crystallite thickness; [D] weighted mean thickness; [E] arithmetic mean thickness.

4.3.2. Influences of solid concentration

The dynamic viscoelastic properties of the two NFC dispersions with different solid concentrations were assessed. The NFC dispersions both showed elastic gel-like behaviors at all solid concentrations (see Appendix Figure 4.A4). Their storage moduli G' (10–1000 Pa) were one order of magnitude higher than their loss moduli G'' (1–100 Pa), and were almost constant across the entire range of ω values, or showed plateau moduli G_p'.[21] The G_p' values of both the NFC dispersions increased with increasing solid concentration, and had a power-law dependence on the solid concentration c, as previously reported (Figure 4.2).[10,15–17,19,21] The relationship between G_p' and c is given by Eq 4.3:

$$G_p' = Ac^{\alpha} \tag{4.3}$$

where A is a front factor related to individual-fiber characteristics such as aspect ratio and elastic modulus, and α is an exponent that reflects the fiber network structure.[10,21] The α value of the hemicellulose-rich NFC dispersion (2.7) was smaller than that of the carboxylate-rich NFC dispersion (3.0), i.e., the concentration dependence of the G_p' value of the carboxylate-rich NFC dispersion was stronger than that for the hemicellulose-rich NFC. This indicates that the interfibrillar interactions of the carboxylate-rich NFC, which is stabilized by electric double-layer repulsion, are stronger than those of the

hemicellulose-rich NFCs, for which there is a significant contribution from hemicellulose-induced steric repulsion in addition to electric double-layer repulsion from the small amount of carboxylate groups.

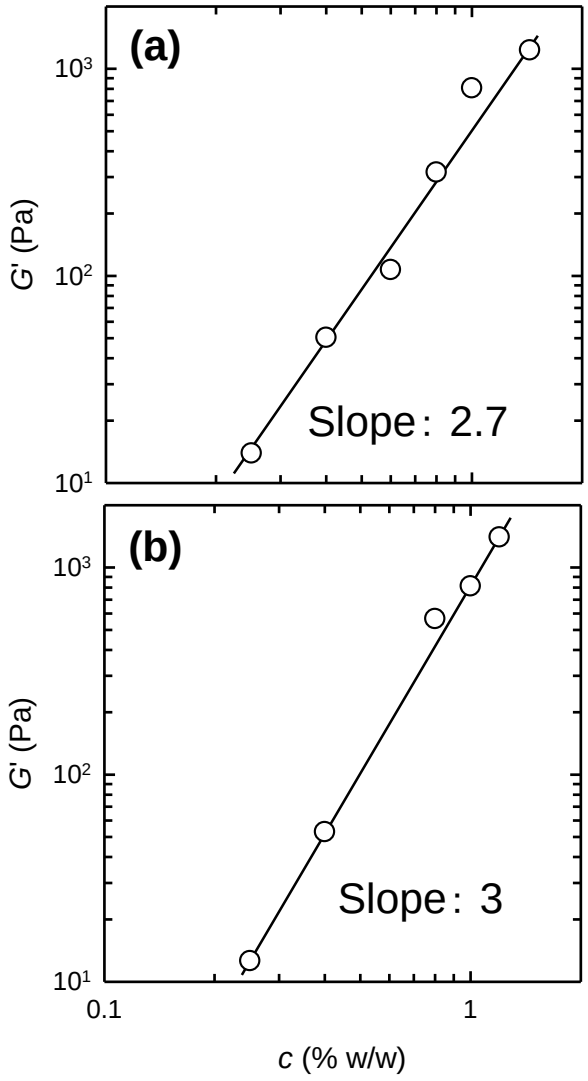

Figure 4.2. Storage moduli G' at 6.66 rad s^{-1} of (a) hemicellulose-rich and (b) carboxylate-rich NFC dispersions as function of solid concentration c.

4.3.3. Influences of salt concentration

Figure 4.3a shows the G' values of the NFC dispersions at 6.66 rad s^{-1} as a function of NaCl concentration (see Appendix, Figure 4.A5 for the G' and G'' values across the entire ω range). The G' value of the carboxylate-rich NFC dispersion increased moderately up to ~500 Pa as the salt concentration was increased from 0 to 100 mM. The G' value of the hemicellulose-rich NFC dispersion clearly increased at a

low salt concentration of 10 mM, but then reached a plateau, at a smaller G' value of ~200 Pa. The difference between the responses of the G' values of the two NFC dispersions to low salt concentrations, up to 10 mM, is probably related to their carboxylate contents; the electric double-layer repulsions between fibrils with carboxylate groups weaken with increasing salt concentration, and the NFCs start to flocculate.

The apparent yield stresses τ_a, or the stresses at which the G' and G'' values begin to transition from the linear to nonlinear viscoelastic region, of the dispersions were determined to evaluate the network strengths of the salt-added NFC dispersions (see Appendix, Figure 4.A1 for the determination of τ_a values).[50–52] The τ_a values of a 0.25% w/w NFC dispersion as a function of salt concentration are shown in Figure 4.3b. The τ_a values of the carboxylate-rich NFC dispersion increased to over 50 Pa with increasing salt concentration. The τ_a values of the hemicellulose-rich NFC dispersion stayed at ~10 Pa, even at the highest salt concentration, i.e., 100 mM.

All these results for the G' and τ_a values indicate that the hemicellulose-rich NFC was loosely flocculated at high salt concentrations and began to flow at small stresses, compared with the carboxylate-rich NFC. This loose flocculation is attributed to the hemicelluloses on the fibril surfaces. A similar tendency has been reported in the literature.[53]

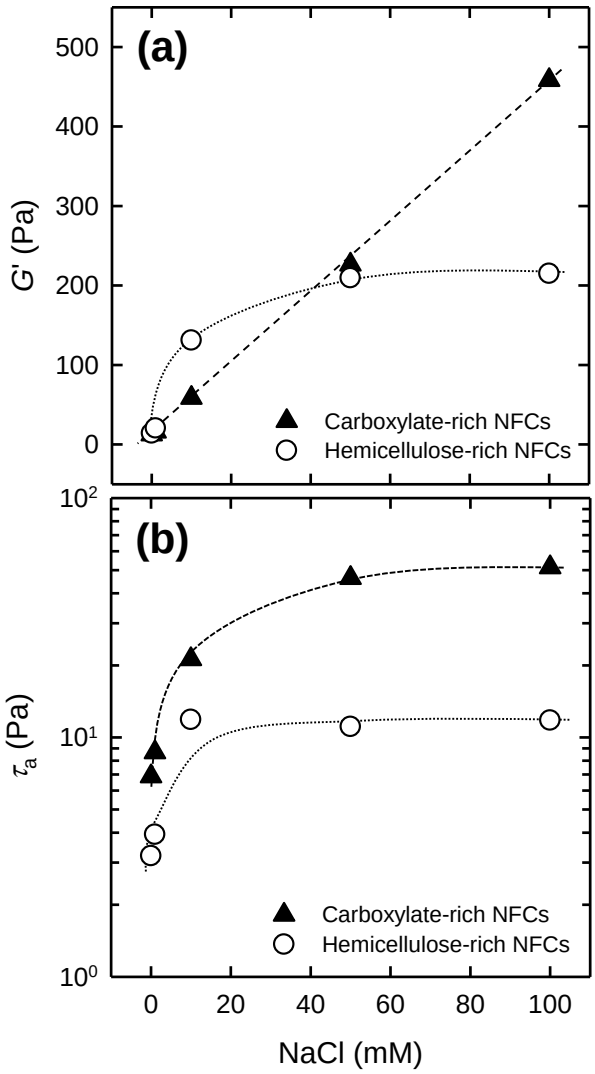

Figure 4.3. (a) Storage moduli G' at 6.66 rad s^{-1} and (b) apparent yield stresses τ_a of 0.25% w/w NFC dispersions as function of NaCl concentration.

This explanation is supported by QCM-D measurements of the wet thin NFC films in phosphate buffers of different concentrations at pH 7 (Figure 4.4 and Appendix, Figures 4.A6 and 4.A7 for the ΔD and Δf curves). The slopes k of the ΔD vs Δf plots reflect how soft or rigid the films on the QCM-D sensors became during the measurements.[54] The steeper the slope, the more dissipative the layer, i.e., the more energy is bound per frequency change unit; a steeper slope indicates that the NFC layer becomes softer and more mobile, whereas more packing of the NFC film structure (rigid film) is reflected by a decreasing k value. The k values of the hemicellulose-rich and carboxylate-rich NFC films in 10 mM

buffer at pH 7 were similar, i.e., 0.18 $\times 10^{-6}$ and 0.21 $\times$ 10^{-6} Hz^{-1}, respectively. However, a significant difference was found in 100 mM buffer. The *k* value of the carboxylate-rich NFC film in 100 mM buffer at pH 7 (0.06 $\times$ 10^{-6} Hz^{-1}) was significantly smaller than that in 10 mM buffer (0.21 $\times$ 10^{-6} Hz^{-1}). The carboxylate-rich NFC film became more rigid with increasing buffer concentration from 10 to 100 mM. The *k* values of the hemicellulose-rich NFC films in 10 and 100 mM buffers were 0.18 $\times$ 10^{-6} and 0.12 $\times$ 10^{-6} Hz^{-1}, respectively. The stiffness of the wet hemicellulose-rich NFC film is therefore less affected by the buffer concentration.

The shear moduli μ_f and hydrodynamic thicknesses h_f of these wet NFC films, which were estimated from their ΔD and Δf curves (see Appendix, Figures 4.A6 and 4.A7), showed similar trends to the *k* values (Figure 4.5). When the buffer concentration was changed from 10 to 100 mM, the μ_f value of the carboxylate-rich NFC film almost doubled, and the h_f values decreased from 7.7 to 2.8 nm. The increase in the μ_f value of the hemicellulose-rich NFC film was more moderate, and the h_f value in 100 mM buffer (6.7 nm) was almost the same as that in 10 mM buffer (6.6 nm). These results show that the hemicellulose-rich NFC films were swollen and softer, even at a high buffer concentration of 100 mM.

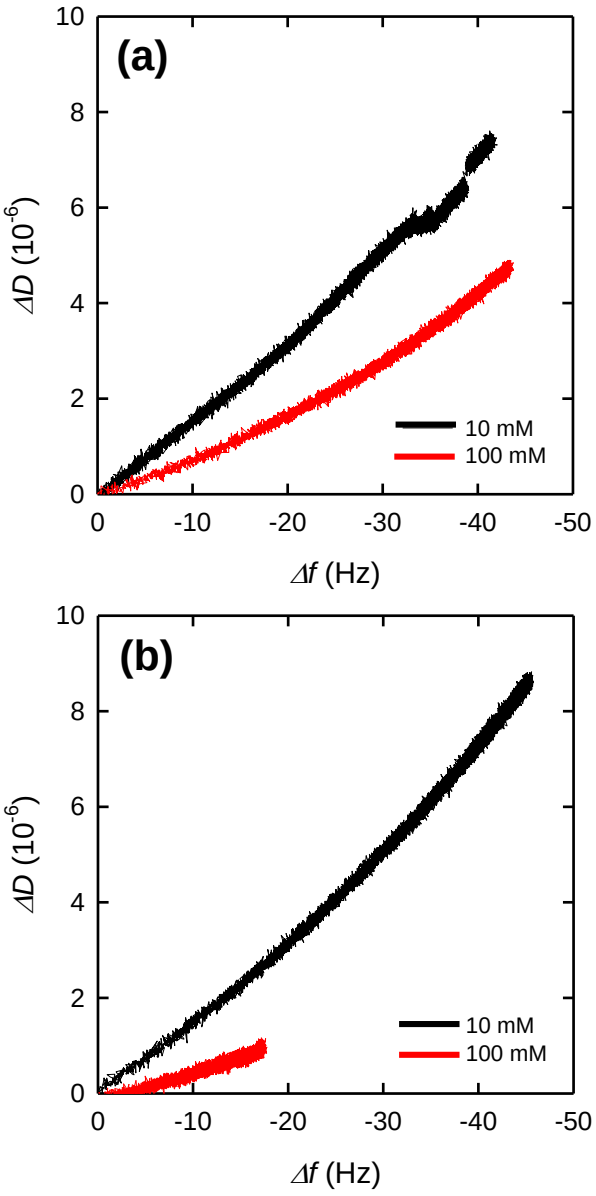

Figure 4.4. Changes in dissipation (ΔD) as a function of changes in frequency (Δf) for (a) hemicellulose-rich and (b) carboxylate-rich NFC films immersed in 10 or 100 mM buffer at pH 7 (f_0 = 5 MHz, n = 3, f_3/n, monitoring time t = 120 min).

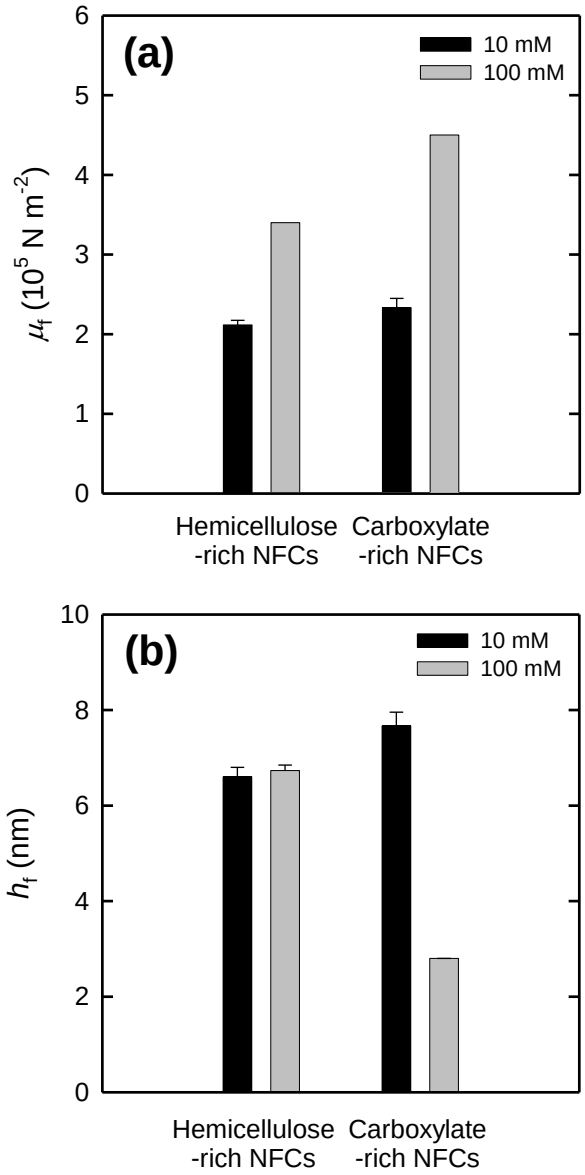

Figure 4.5. (a) Shear moduli μ_f and (b) hydrodynamic thicknesses h_f of NFC films immersed in 10 or 100 mM buffer at pH 7, at end of measurements (Voigt model, assumed layer density ρ_f =1200 kg m^{-3}).

4.3.4. Influences of pH

The effects of pH on the *G*' values are shown in Figure 4.6 (see Appendix, Figure 4.A8 for the *G*' and *G*" values across the entire ω range). At pH less than 3, most of the carboxylate groups with a pK_a value of 3.6 are not dissociated; the almost non-charged NFC agglomerates and forms self-standing stiff gels (see Appendix, Figure 4.A9 for the changes in turbidity with decreasing pH from ~7 to 2).[21] When the pH

values of the NFC dispersions were decreased from the neutral region, i.e., 6–7, to 2, the *G*' values of the hemicellulose-rich and carboxylate-rich NFC dispersions increased approximately from 10 to 400 and 1400 Pa, respectively. The difference between these *G*' values at pH 2 can be explained by the contribution of the soft hemicellulose layers. When the pH was increased to 10, the *G*' value of the carboxylate-rich NFC dispersion decreased, as reported in the literature.[27] In contrast, the *G*' value of the hemicellulose-rich NFC dispersion increased slightly at pH 10. This is probably the result of alkali-induced gelation of the glucomannan fraction in the hemicelluloses (see Appendix, Table 4.A1 and Figure 4.A9 for the changes in turbidity with increasing pH from ~7 to 10).[55,56]

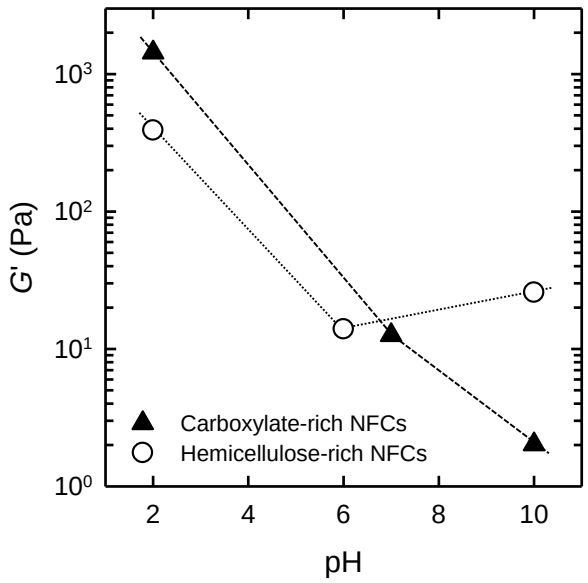

Figure 4.6. Storage moduli *G*' at 6.66 rad s^{-1} of 0.25% w/w NFC dispersions as function of pH.

The viscoelastic properties of wet thin NFC films in 10 mM buffers at pH 3, 5, and 7 were investigated using QCM-D. The values for the pH 10 buffer could not be measured because significant amounts of the NFCs became detached from the QCM-D sensor surfaces during the measurements (see Appendix, Figures 4.A6 and 4.A7). At pH 3–7, the hemicellulose-rich NFC films were swollen, and their slopes became steeper with increasing pH, i.e., the films became softer (Figure 4.7a). The ΔD vs Δf plots of the carboxylate-rich NFC film immersed in pH 3 buffer showed the opposite trend to those for the other

films, and showed de-swelling behavior (Figure 4.7b).[30] The μ_f and h_f values of these wet NFC films, estimated from their ΔD and Δf curves, show similar trends to the k values (Figure 4.8).

The μ_f values of the hemicellulose-rich and carboxylate-rich NFC films both decreased, and their h_f values increased; the wet films became softer because of induction of electric double-layer repulsion at higher pH values. At pH 3, the carboxylate-rich film showed negligibly small ΔD values, i.e., less than 1.0 $\times$ 10^{-6} (see Appendix, Figure 4.A7), and is therefore assumed to be highly elastic and rigid. Accordingly, the ΔD and Δf curves did not fit the Voigt-based viscoelastic model.[53]

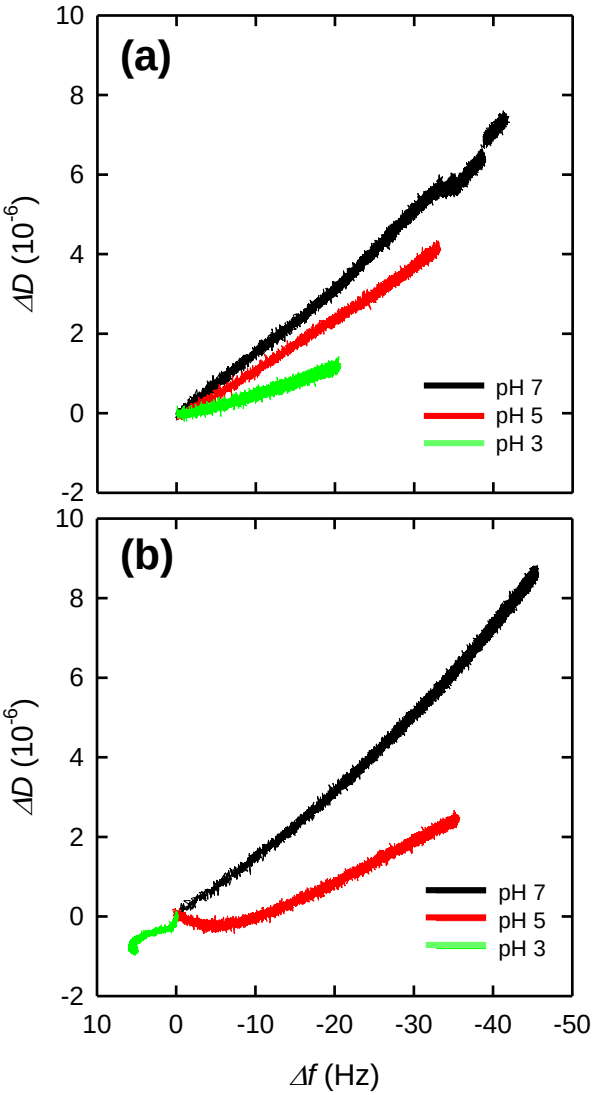

Figure 4.7. Change in dissipation (ΔD) as function of change in frequency (Δf) for (a) hemicellulose-rich and (b) carboxylate-rich NFC films immersed in 10 mM buffers at pH 3, 5, and 7 (f_0 = 5 MHz, n = 3, f_3/n, t = 120 min).

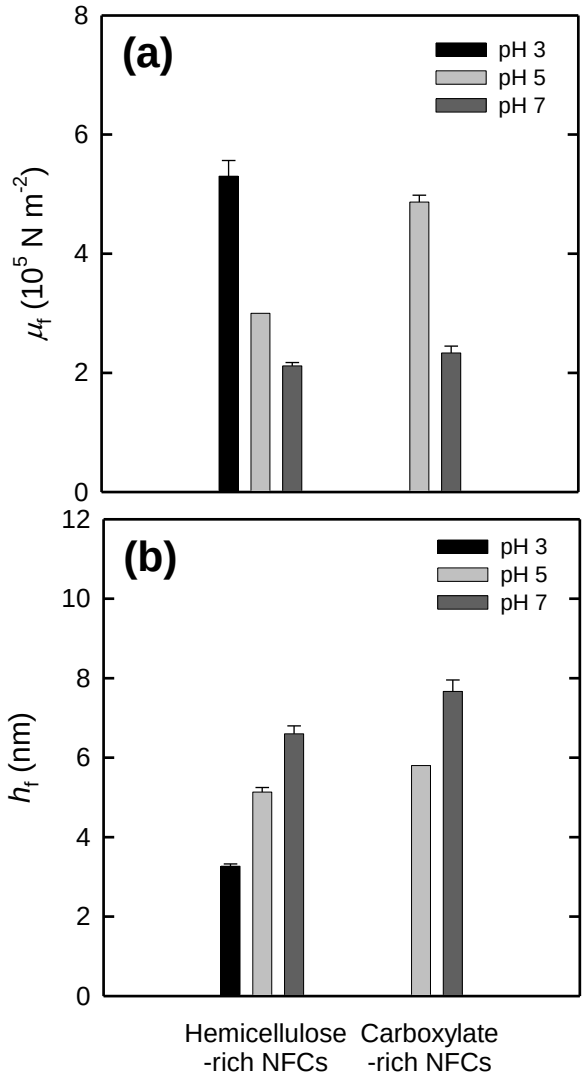

Figure 4.8. (a) Shear moduli μ_f and (b) hydrodynamic thicknesses h_f of wet NFC films immersed in 10 mM buffers at pH 3, 5, and 7, at end of measurements (Voigt model, assumed ρ_f = 1200 kg m^{-3}).

4.4. Conclusions

The viscoelastic properties of core–shell-structured, hemicellulose-rich NFC dispersions and their wet films were investigated as functions of solid concentration, salt concentration, and pH value, and compared with those of carboxylate-rich NFC dispersions and their wet films. Although the G_p' values of both NFC dispersions showed strong power-law dependences on their solid concentrations ($G_p' \propto c^{\alpha}$), the α value for the hemicellulose-rich NFC (2.7) was slightly smaller than that for the carboxylate-rich NFC (3.0), showing lower interfibrillar interactions in the hemicellulose-rich NFC. The changes in G' and τ_a as a

function of salt concentration showed loose flocculation of the hemicellulose-rich NFC dispersion even at high salt concentrations. The viscoelastic properties of their wet films, evaluated using QCM-D, indicated the same tendency; the hemicellulose-rich NFC films were swollen and soft at high salt concentrations, whereas the carboxylate-rich NFC films became rigid. When the pH of the dispersions was decreased to 2, the resulting hemicellulose-rich NFC gel was less stiff than the carboxylate-rich NFC gel. At pH 10, the hemicellulose-rich NFC flocculated, probably because of alkali-induced gelation of the glucomannan fraction. The QCM-D measurements as a function of pH showed that the wet films of the hemicellulose-rich NFC were swollen even at pH 3, whereas the carboxylate-rich NFC films became highly elastic and rigid. All these results show that the surface hemicelluloses in core–shell-structured, hemicellulose-rich NFCs make substantial contributions to the viscoelastic properties of their dispersions and wet films.

4.5. Appendix

4.5.1. Strain sweep measurement of NFC dispersions

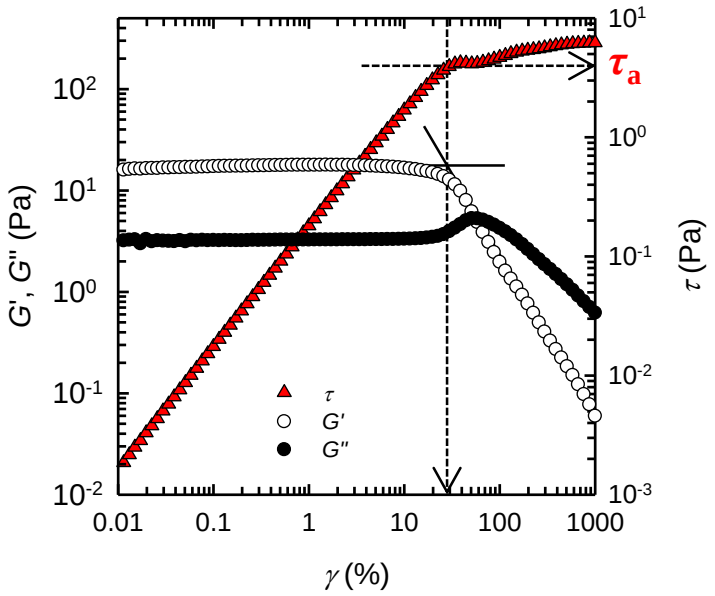

Figure 4.A1. Typical plots of storage modulus G', loss modulus G'', and shear stress τ of NFC dispersion as function of strain γ. Apparent yield stress τ_a of NFC dispersion was determined as stress at which G' and G'' values begin to transition from linear to nonlinear viscoelastic region.

4.5.2. AFM observation of NFC-coated QCM-D sensor surfaces

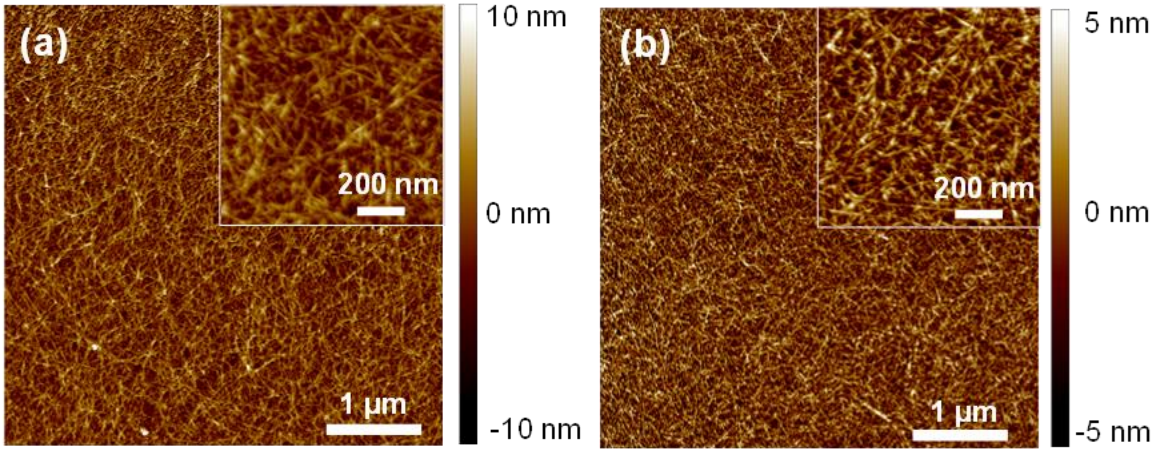

Figure 4.A2. AFM images of the QCM-D sensor surfaces coated with thin hemicellulose-rich (a) and carboxylate-rich (b) NFC films.

4.5.3. XRD pattern of NFCs

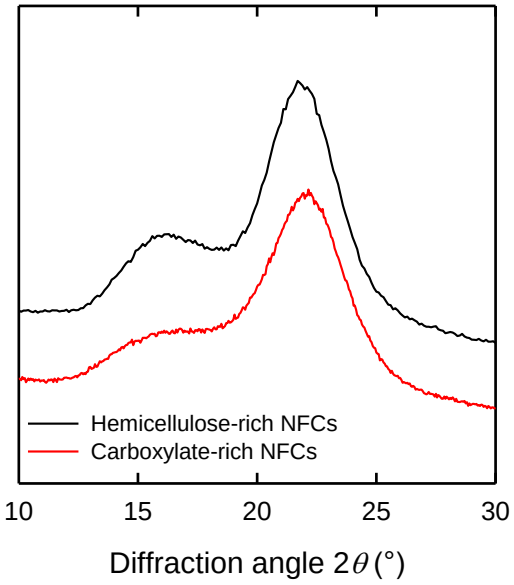

Figure 4.A3. XRD pattern of NFCs.

4.5.4. Neutral sugar composition analysis

Table 4.A1. Neutral sugar composition of the NFCs.

	Glucose (%)	Galactose (%)	Mannose (%)	Arabinose (%)	Xylose (%)	Rhamnose (%)	Total (%)	Others[a] (%)
Hemicelulose-rich NFCs	58.0	7.3	3.1	1.6	10.5	0.9	81.3	18.7
Carboxylate-rich NFCs	59.3	0	1.6	0	5.7	0	66.6	33.4

[a] Others include uronates.

4.5.5. Storage modulus *G*' and loss modulus *G*" of 0.25–1.4% w/w NFC dispersions across entire angular frequency range

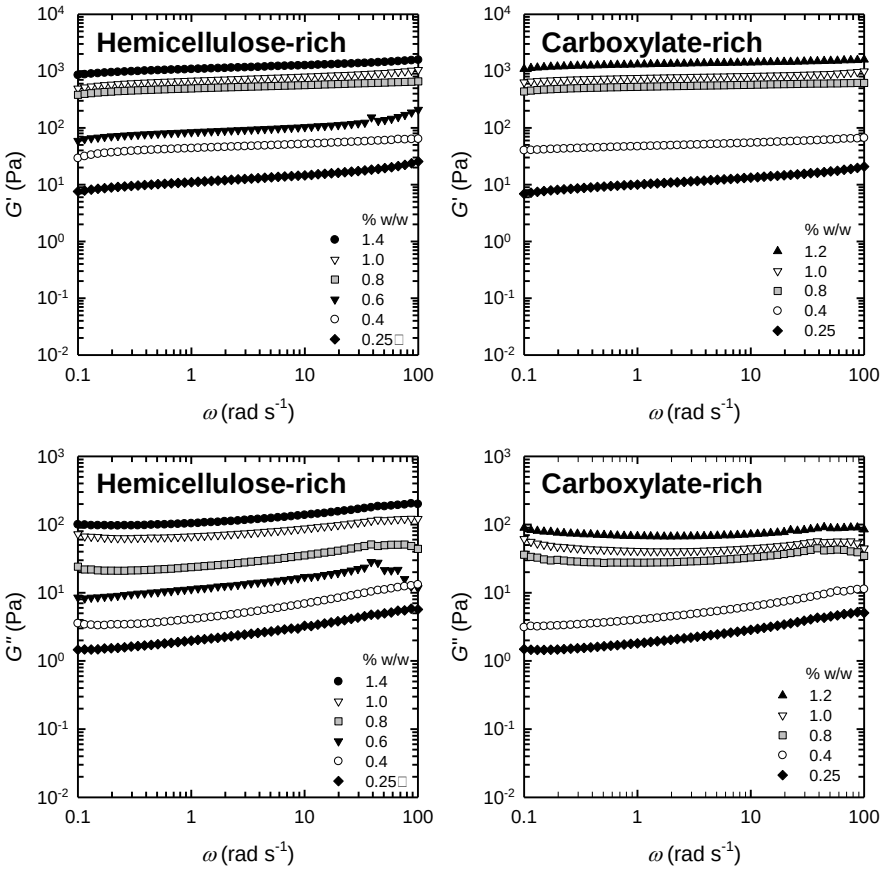

Figure 4.A4. *G*' and *G*" values of 0.25–1.4% w/w NFC dispersions as function of ω.

4.5.6. Storage modulus *G*' and loss modulus *G*" of 0.25% w/w NFC dispersions with 0–100 mM NaCl across entire angular frequency range

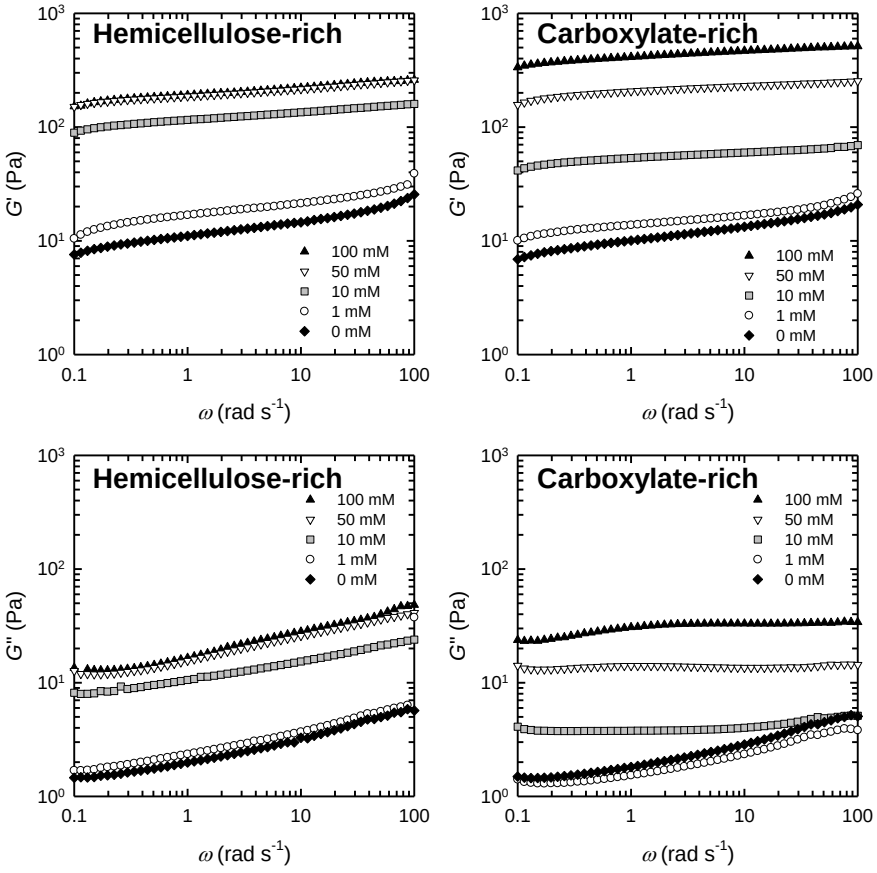

Figure 4.A5. *G*' and *G*" values of 0.25% w/w NFC dispersions with 0–100 mM NaCl as function of ω.

4.5.7. Change in frequency Δ*f* and change in dissipation Δ*D* curves for hemicellulose-rich NFC films in 10 mM pH 3–10 buffers as a function of time

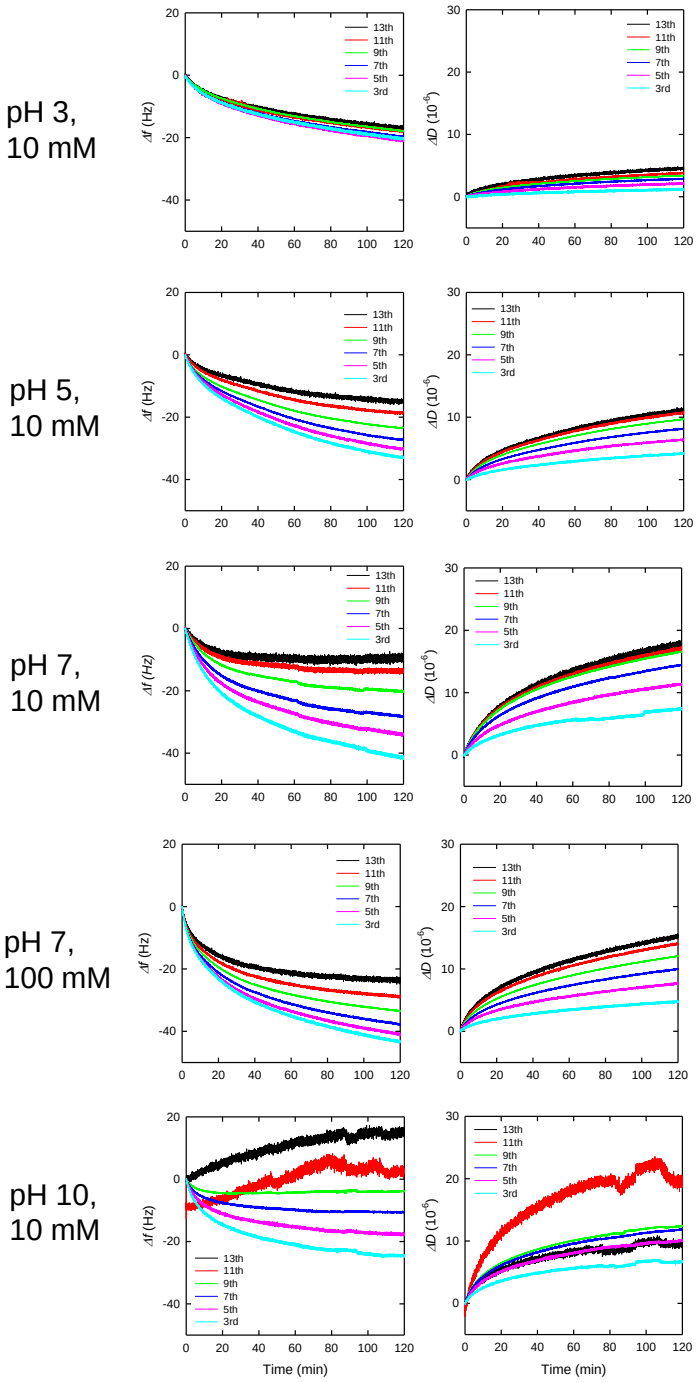

Figure 4.A6. Δ*f* and Δ*D* curves for hemicellulose-rich NFC films immersed in 10 or 100 mM buffers at pH 3–10 (*n* = 3, 5, 7, 9, 11, 13).

4.5.8. Change in frequency Δ*f* and change in dissipation Δ*D* curves for carboxylate-rich NFC films in 10 mM pH 3–10 buffers as a function of time

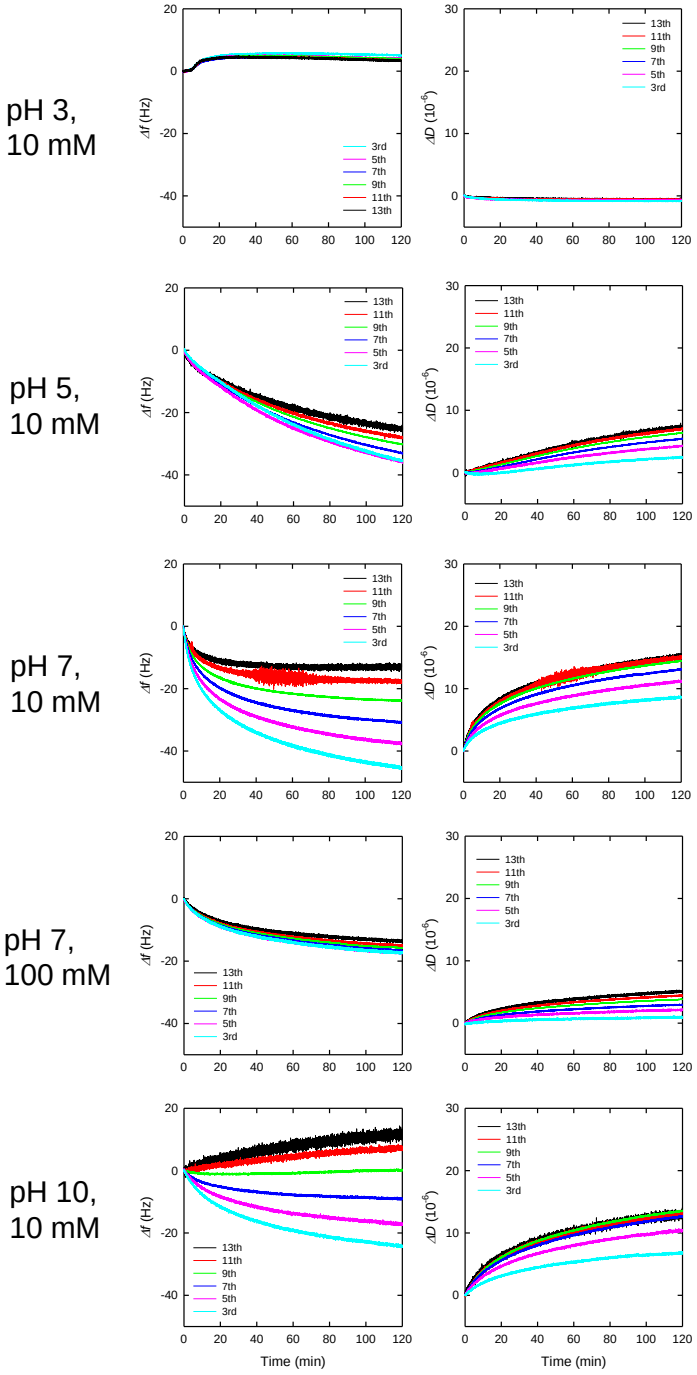

Figure 4.A7. Δ*f* and Δ*D* curves for carboxylate-rich NFC films immersed in 10 or 100 mM buffers at pH 3–10 (*n* = 3, 5, 7, 9, 11, 13).

4.5.9. Storage modulus *G*' and loss modulus *G*" of 0.25% w/w NFC dispersions at pH 2–10 across entire angular frequency range

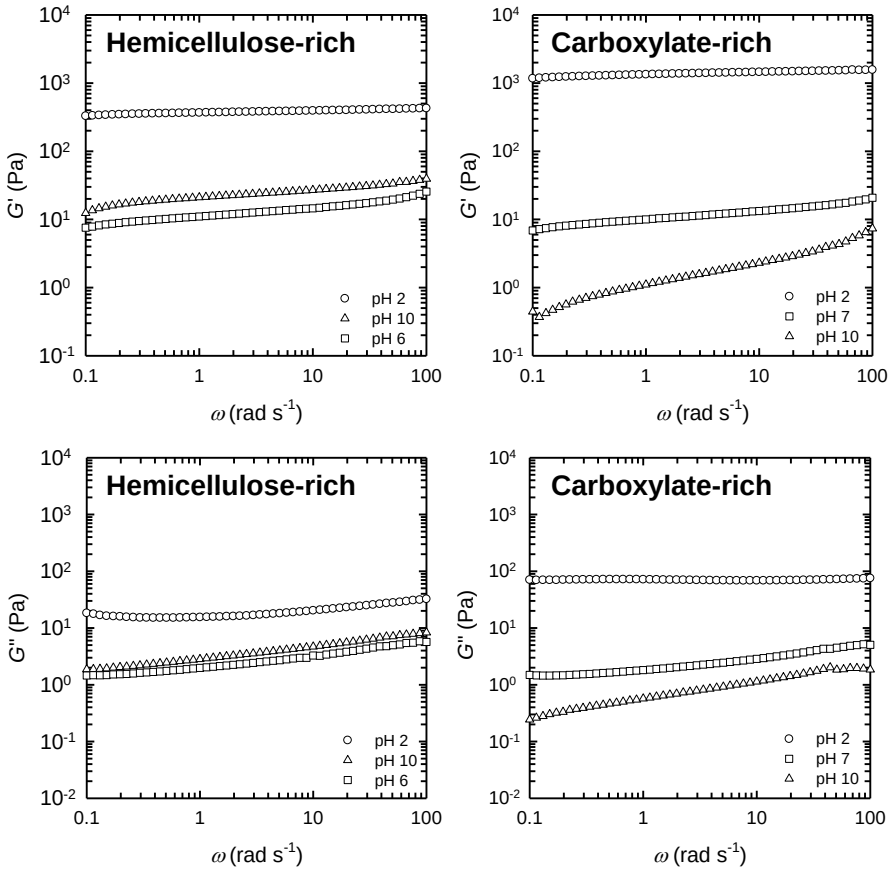

Figure 4.A8. *G*' and *G*" values of 0.25% w/w NFC dispersions at pH 2–10 as function of ω.

4.5.10. Turbidity of 0.25% w/w NFC dispersions at pH 2–10

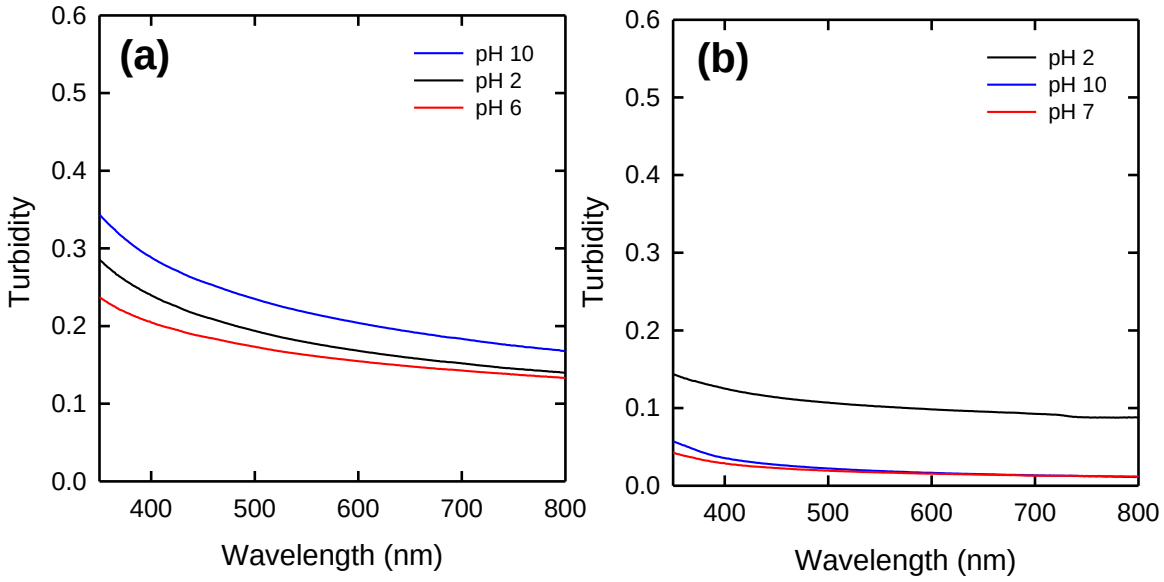

Figure 4.A9. Turbidities of the (a) hemicellulose-rich and (b) carboxylate-rich NFC dispersions at pH 2–10.

4.6. References

1) Larsson, P.; Berglund, L.; Wågberg, L. Highly ductile fibres and sheets by core-shell structuring of the cellulose nanofibrils. *Cellulose* **2014**, *21*, 323–333.

2) Larsson, P. A.; Berglund, L. A.; Wågberg, L. Ductile all-cellulose nanocomposite films fabricated from core–shell structured cellulose nanofibrils. *Biomacromolecules* **2014**, *15*, 2218–2223.

3) Prakobna, K.; Terenzi, C.; Zhou, Q.; Furó, I.; Berglund, L. A. Core–shell cellulose nanofibers for biocomposites–Nanostructural effects in hydrated state. *Carbohydr. Polym.* **2015**, *125*, 92–102.

4) Prakobna, K.; Kisonen, V.; Xu, C.; Berglund, L. A. Strong reinforcing effects from galactoglucomannan hemicellulose on mechanical behavior of wet cellulose nanofiber gels. *J. Mater. Sci.* **2015**, *50*, 7413–7423.

5) Galland, S.; Berthold, F.; Prakobna, K.; Berglund, L. A. Holocellulose nanofibers of high molar mass and small diameter for high-strength nanopaper. *Biomacromolecules* **2015**, *16*, 2427–2435.

6) Prakobna, K.; Galland, S.; Berglund, L. A. High-performance and moisture-stable cellulose–starch nanocomposites based on bioinspired core–shell nanofibers. *Biomacromolecules* **2015**, *16*, 904–912.

7) Sehaqui, H.; Zhou, Q.; Berglund, L. A. Nanostructured biocomposites of high toughness—a wood cellulose nanofiber network in ductile hydroxyethylcellulose matrix. *Soft Matter* **2011**, *7*, 7342–7350.

8) Olszewska, A.; Valle-Delgado, J. J.; Nikinmaa, M.; Laine, J.; Österberg, M. Direct measurements of non-ionic attraction and nanoscaled lubrication in biomimetic composites from nanofibrillated cellulose and modified carboxymethylated cellulose. *Nanoscale* **2013**, *5*, 11837–11844.

9) Olszewska, A.; Junka, K.; Nordgren, N.; Laine, J.; Rutland, M. W.; Österberg, M. Non-ionic assembly of nanofibrillated cellulose and polyethylene glycol grafted carboxymethyl cellulose and the effect of aqueous lubrication in nanocomposite formation. *Soft Matter* **2013**, *9*, 7448–7457.

10) Tatsumi, D.; Ishioka, S.; Matsumoto, T. Effect of fiber concentration and axial ratio on the rheological properties of cellulose fiber suspensions. *Nihon Reoroji Gakk.* **2002**, *30*, 27–32.

11) Tanaka, R.; Saito, T.; Ishii, D.; Isogai, A. Determination of nanocellulose fibril length by shear viscosity measurement. *Cellulose* **2014**, *21*, 1581–1589.

12) Tanaka, R.; Saito, T.; Hondo, H.; Isogai, A. Influence of flexibility and dimensions of nanocelluloses on the flow properties of their aqueous dispersions. *Biomacromolecules* **2015**, *16*, 2127–2131.

13) Naderi, A.; Lindström, T.; Sundström, J. Repeated homogenization, a route for decreasing the energy consumption in the manufacturing process of carboxymethylated nanofibrillated cellulose? *Cellulose* **2015**, *22*, 1147–1157.

14) Lasseuguette, E.; Roux, D.; Nishiyama, Y. Rheological properties of microfibrillar suspension of TEMPO-oxidized pulp. *Cellulose* **2008**, *15*, 425–433.

15) Pääkkö, M.; Ankerfors, M.; Kosonen, H.; Nykänen, A.; Ahola, S.; Österberg, M.; Ruokolainen, J.; Laine, J.; Larsson, P. T.; Ikkala, O.; Lindström, T. Enzymatic Hydrolysis Combined with mechanical shearing and high-pressure homogenization for nanoscale cellulose fibrils and strong gels. *Biomacromolecules* **2007**, *8*, 1934–1941.

16) Naderi, A.; Lindström, T.; Sundström, J. Carboxymethylated nanofibrillated cellulose: rheological studies. *Cellulose* **2014**, *21*, 1561–1571.

17) Agoda-Tandjawa, G.; Durand, S.; Berot, S.; Blassel, C.; Gaillard, C.; Garnier, C.; Doublier, J.-L. Rheological characterization of microfibrillated cellulose suspensions after freezing. *Carbohydr. Polym.* **2010**, *80*, 677–686.

18) Naderi, A.; Lindström, T.; Pettersson, T. The state of carboxymethylated nanofibrils after homogenization-aided dilution from concentrated suspensions: a rheological perspective. *Cellulose* **2014**, *21*, 2357–2368.

19) Jowkarderis, L.; van de Ven, T. G. Rheology of semi-dilute suspensions of carboxylated cellulose nanofibrils. *Carbohydr. Polym.* **2015**, *123*, 416–423.

20) Li, M.; Wu, Q.; Song, K.; Lee, S.; Qing, Y.; Wu, Y. Cellulose Nanoparticles: structure-morphology-rheology relationship. *ACS Sustainable Chem. Eng.* **2015**, *3*, 821–832.

21) Saito, T.; Uematsu, T.; Kimura, S.; Enomae, T.; Isogai, A. Self-aligned integration of native cellulose nanofibrils towards producing diverse bulk materials. *Soft Matter* **2011**, *7*, 8804–8809.

22) Nechyporchuk, O.; Belgacem, M. N.; Pignon, F. Rheological properties of micro-/nanofibrillated cellulose suspensions: Wall-slip and shear banding phenomena. *Carbohydr. Polym.* **2014**, *112*, 432–439.

23) Tatsumi, D.; Ishioka, S.; Matsumoto, T. Effect of Particle and Salt concentrations on the rheological properties of cellulose fibrous suspensions. *Nihon Reoroji Gakk.* **1999**, *27*, 243–248.

24) Sim, K.; Lee, J.; Lee, H.; Youn, H. Flocculation behavior of cellulose nanofibrils under different salt conditions and its impact on network strength and dewatering ability. *Cellulose* **2015**, *22*, 3689–3700.

25) Lowys, M. P.; Desbrières, J.; Rinaudo, M. Rheological characterization of cellulosic microfibril suspensions. Role of polymeric additives. *Food Hydrocolloids* **2001**, *15*, 25–32.

26) Jowkarderis, L.; van de Ven, T. G. Intrinsic viscosity of aqueous suspensions of cellulose nanofibrils. *Cellulose* **2014**, *21*, 2511–2517.

27) Way, A. E.; Hsu, L.; Shanmuganathan, K.; Weder, C.; Rowan, S. J. pH-Responsive cellulose nanocrystal gels and nanocomposites. *ACS Macro Lett.* **2012**, *1*, 1001–1006.

28) Iotti, M.; Gregersen, Ø. W.; Moe, S.; Lenes, M. Rheological studies of microfibrillar cellulose water dispersions. *J. Polym. Environ.* **2011**, *19*, 137–145.

29) Arola, S.; Malho, J. -M.; Laaksonen, P.; Lille, M.; Linder, M. B. The role of hemicellulose in nanofibrillated cellulose networks. *Soft Matter* **2013**, *9*, 1319–1326.

30) Ahola, S.; Salmi, J.; Johansson, L.-S.; Laine, J.; Österberg, M. Model films from native cellulose nanofibrils. Preparation, swelling, and surface interactions. *Biomacromolecules* **2008**, *9*, 1273–1282.

31) Fält, S.; Wågberg, L.; Vesterlind, E.-L. Swelling of model films of cellulose having different charge densities and comparison to the swelling behavior of corresponding Fibers. *Langmuir* **2003**, *19*, 7895–7903.

32) Tammelin, T.; Merta, J.; Johansson, L.-S.; Stenius, P. Viscoelastic properties of cationic starch adsorbed on quartz studied by QCM-D. *Langmuir* **2004**, *20*, 10900–10909.

33) Tammelin, T.; Paananen, A.; Österberg, M., *Hemicelluloses at interfaces: Some aspects of the interactions;* Wiley-Blackwell Publishing Ltd, Chichester: 2009.

34) Joye, D.; Luzio, G. Process for selective extraction of pectins from plant material by differential pH. *Carbohydr. Polym.* **2000**, *43*, 337–342.

35) Wise, L. E.; Murphy, M.; D'Adieco, A. A. A chlorite holocellulose, its fractionation and bearing on summative wood analysis and studies on the hemicelluloses. *Paper Trade J.* **1946**, *122*, 35–43.

36) Tanaka, R.; Saito, T.; Isogai, A. Cellulose nanofibrils prepared from softwood cellulose by TEMPO/NaClO/$NaClO_2$ systems in water at pH 4.8 or 6.8. *Int. J. Biol. Macromol.* **2012**, *51*, 228–234.

37) Rodahl, K.; Höök, F.; Krozer, A.; Brezezinski, P.; Kasemo, B. Quartz crystal microbalance setup for frequency and Q-factor measurements in gaseous and liquid environments. *Rev. Sci. Instrum.* **1995**, *66*, 3924–3930.

38) Höök, F.; Rodahl, M.; Brzezinski, P.; Kasemo, B. Energy dissipation kinetics for protein and antibody-antigen adsorption under shear oscillation on a quartz crystal microbalance. *Langmuir*, **1998**,*14*, 729–734.

39) Tammelin, T.; Saarinen, T.; Österberg, M.; Laine, J. Preparation of Langmuir/Blodgett-cellulose surfaces by using horizontal dipping procedure. Application for polyelectrolyte adsorption studies

performed with QCM-D. Cellulose **2006**, 13, 519–535.

40) Eronen, P.; Laine, J.; Ruokolainen, J.; Österberg, M. Comparison of multilayer formation between different cellulose nanofibrils and cationic polymers. *J. Colloid Interface Sci.* **2012**, *373*, 84–93.

41) Voinova, M. V.; Rodahl, M.; Jonson, M.; Kasemo, B. Viscoelastic acoustic response of layered polymer films at fluid-solid interfaces: continuum mechanics approach. *Phys. Scr.* **1999**, *59*, 391–396.

42) Liu, Z.; Choi, H.; Gatenholm, P.; Esker, A. R. Quartz crystal microbalance with dissipation monitoring and surface plasmon resonance studies of carboxymethyl cellulose adsorption onto regenerated cellulose surfaces. *Langmuir* **2011**, *27*, 8718–8728.

43) Saito, T.; Isogai, A. TEMPO-mediated oxidation of native cellulose. The effect of oxidation conditions on chemical and crystal structures of the water-insoluble fractions. *Biomacromolecules* **2004**, *5*, 1983–1989.

44) Saito, T.; Kuramae, R.; Wohlert, J.; Berglund, L. A.; Isogai, A. An ultrastrong nanofibrillar biomaterial: the strength of single cellulose nanofibrils revealed via sonication-induced fragmentation. *Biomacromolecules* **2013**, *14*, 248–253.

45) Shi, Z.; Yang, Q.; Ono, Y.; Funahashi, R.; Saito, T.; Isogai, A. Creation of a new material stream from Japanese cedar resources to cellulose nanofibrils. *React. Funct. Polym.* **2015**, *95*, 19–24.

46) Patterson, A. The Scherrer formula for X-ray particle size determination. *Phys. Rev.* **1939**, *56*, 978–982.

47) Fall, A. B.; Lindström, S. B.; Sundman, O.; Ödberg, L.; Wågberg, L. Colloidal stability of aqueous nanofibrillated cellulose dispersions. *Langmuir* **2011**, *27*, 11332–11338.

48) Iwamoto, S.; Abe, K.; Yano, H. The effect of hemicelluloses on wood pulp nanofibrillation and nanofiber network characteristics. *Biomacromolecules* **2008**, *9*, 1022–1026.

49) Rodionova, G.; Lenes, M.; Eriksen, Ø.; Gregersen, Ø. Surface chemical modification of microfibrillated cellulose: improvement of barrier properties for packaging applications. *Cellulose* **2011**, *18*, 127–134.

50) Swerin, A.; Powell, R.; Ödberg, L. Linear and nonlinear dynamic viscoelasticity of pulp fiber suspensions. *Nord. Pulp Pap. Res. J.* **1992**, *7*, 126–133.

51) Horvath, A. E.; Lindström, T. The influence of colloidal interactions on fiber network strength. *J. Colloid Interface Sci.* **2007**, *309*, 511–517.

52) Yanez, J. A.; Shikata, T.; Lange, F. F.; Pearson, D. S. Shear modulus and yield stress measurements of attractive alumina particle networks in aqueous slurries. *J. Am. Chem. Soc.* **1996**, *79*, 2917–2917.

53) Tenhunen, T.-M.; Peresin, M. S.; Penttilä, P. A.; Pere, J.; Serimaa, R.; Tammelin, T. Significance of xylan on the stability and water interactions of cellulosic nanofibrils. *React. Funct. Polym.* **2014**, *85*, 157–166.

54) Doliška, A.; Ribitsch, V.; Kleinschek, K. S.; Strnad, S. Viscoelastic properties of fibrinogen adsorbed onto poly (ethylene terephthalate) surfaces by QCM-D. *Carbohydr. Polym.* **2013**, *93*, 246–255.

55) Zhang, H.; Yoshimura, M.; Nishinari, K.; Williams, M.; Foster, T.; Norton, I. Gelation behaviour of konjac glucomannan with different molecular weights. *Biopolymers* **2001**, *59*, 38–50.
56) Luo, X.; He, P.; Lin, X. The mechanism of sodium hydroxide solution promoting the gelation of Konjac glucomannan (KGM). *Food Hydrocolloids* **2013**, *30*, 92–99.

Chapter 5

Summary

Rheological properties of individualized NFC dispersions were comprehensively investigated. First, the influences of the fibril lengths and the surface charge densities on flow properties of their dilute dispersions were examined. The individualized NFCs consisting of ~3 nm-wide and surface-carboxylated fibrils with the weighted mean lengths L_w of 270–980 nm were prepared by TEMPO-mediated oxidation. The critical concentrations c^* of these NFC dispersions were given by $c^* = 18/p^2$ using their aspect ratios p, which defines their dilute regions. The maximum relaxation times τ of these dilute NFC dispersions were independent of the thickness of the electric double layer, and thus were irrespective of the carboxylate content or surface charge density. The viscosity-average lengths L_{vsic} of the NFCs, which were calculated by applying their maximum relaxation times τ to the theoretical equation for rotational motions of rigid polymers, had a linear relationship to the L_w values, which was described as $L_{visc} = 1.764 \times L_w + 764$. However, the resulting L_{vsic} values (1,100–2,500 nm) were much larger than the L_w values (270–980 nm) determined by microscopy. This discrepancy is likely to be caused by the flexibility of NFCs in water. Furthermore, the theoretical equation is defined assuming rigid polymer chains dissolved in liquid, and the volume of solid rods or fibrils are thus not taken into account, which might also cause the discrepancy.

The influences of the flexibility and dimensions of the NFCs on the flow properties of their dilute dispersions were thus investigated. Rod-like NCCs with different average widths were used as the reference samples. The dimensions, or the widths and length distributions of these NFCs and NCCs, had significant influences on the τ values of their dispersions, explaining the fact that the theoretical τ values calculated for the individualized NFCs and NCCs assuming monodisperse rigid polymers, are different from their experimental τ values. Meanwhile, the experimental intrinsic viscosities $[\eta]$ of the low-aspect-ratio NFCs and NCCs were in good agreement with their theoretical $[\eta]$ values calculated assuming solid rigid rods. However, the experimental $[\eta]$ values for high-aspect-ratio NFCs were still

larger than their theoretical ones; this is likely to arise from the flexibility of NFC fibrils. When the $[\eta]$ *vs.* p values were plotted, the experimental $[\eta]$ values of the NFC and NCC dispersions were expressed as $\rho[\eta] = 0.15 \times p^{1.9}$ using the density of nanocellulose ρ, where the flexibility of the NFCs and NCCs should be taken into account by the exponent 1.9; in fact, as the aspect ratios of the fibrils increase, they become more flexible and their intrinsic viscosities exponentially increase. In a practical sense, the average lengths of both individualized NFCs and NCCs can be determined by applying the experimental $[\eta]$ values of their dispersions to this empirical equation.

The viscoelastic properties of individualized NFC dispersions and their wet films were investigated by dynamic viscoelastic measurements and quartz crystal microbalance with dissipation (QCM-D) measurements, respectively, in terms of solid concentration, salt concentration, and pH. Here, a hemicellulose-rich NFC with a low carboxylate content, purified from Japanese persimmons, was used to assess the influences of their surface-adsorbed hemicelluloses in comparison with a carboxylate-rich NFC with a low hemicellulose content, or the TEMPO-oxidized NFC prepared from a bleached softwood kraft pulp. The results for the solid-concentration c dependences of the plateau moduli G_p' indicated that the hemicellulose-rich NFC had weaker interfibrillar interactions than the carboxylate-rich NFC. At high salt concentrations or low pH values, both the hemicellulose-rich and carboxylate-rich NFCs were agglomerated. However, the agglomerates of the hemicellulose-rich NFC were significantly looser than those of the carboxylate-rich one. Their wet films denoted the same tendency of the dispersions; the hemicellulose-rich NFC films were swollen and soft even at the high salt concentrations or low pH values, whereas the carboxylate-rich NFC films became rigid. These results demonstrate that the surface-adsorbed hemicelluloses in the hemicellulose-rich NFC substantially contribute to the viscoelastic properties of their water dispersions and wet films.

The fundamental and essential aspects of the flow and viscoelastic properties of NFC/water dispersions have been revealed by using the individualized NFCs prepared via TEMPO-mediated oxidation. These findings from the present study would surely contribute to not only the promotion of the

nanocellulose utilization at the industrial level but also the understanding of cellulose microfibrils biosynthesized in water.

Publications

Peer-reviewed journal articles

1) **Reina Tanaka**, Tsuguyuki Saito, Akira Isogai. “Cellulose nanofibrils prepared from softwood cellulose by TEMPO/NaClO/$NaClO_2$ systems in water at pH 4.8 or 6.8”, *International Journal of Biological Macromolecules*, **2012**, *51*(3), 228–234.

2) **Reina Tanaka**, Tsuguyuki Saito, Daisuke Ishii, Akira Isogai. “Determination of nanocellulose fibril length by shear viscosity measurement”, *Cellulose*, **2014**, *21*(3), 1581–1589.

3) **Reina Tanaka**, Tsuguyuki Saito, Hiromasa Hondo, Akira Isogai. “Influences of flexibility and dimensions of nanocelluloses on the flow properties of their aqueous dispersions", *Biomacromolecules*, **2015**, *16* (7), 2127–2131.

4) **Reina Tanaka**, Tsuguyuki Saito, Tuomas Hänninen, Yuko Ono, Minna Hakalahti, Tekla Tammelin, Akira Isogai. “Viscoelastic properties of core–shell-structured, hemicellulose-rich nanofibrillated cellulose in dispersions and wet film states”, *submitted to Biomacromolecules.*

5) Hayaka Fukuzumi, **Reina Tanaka**, Tsuguyuki Saito, Akira Isogai. “Dispersion stability and aggregation behavior of TEMPO-oxidized cellulose nanofibrils in water as a function of salt addition”, *Cellulose*, **2014**, *21*(3), 1553–1559.

6) Satoshi Takaichi, Tsuguyuki Saito, **Reina Tanaka**, Akira Isogai. “Improvement of nanodispersibility of oven-dried TEMPO-oxidized celluloses in water”, *Cellulose*, **2014**, *21*(6), 4093–4103.

7) Yuko Ono, **Reina Tanaka**, Ryunosuke Funahashi, Miyuki Takeuchi , Tsuguyuki Saito, Akira Isogai. “SEC-MALLS analysis of ethylene diamine-pretreated native celluloses in LiCl/DMAc: softwood kraft pulp and highly crystalline bacterial, tunicate and algal celluloses”, *submitted to Cellulose.*

8) 田仲玲奈・橋本禅・星野敏・九鬼康彰　「生ごみ利活用の環境配慮行動メカニズム」、農村計画学会誌、**2011**、*30*、351–356.

International Conference

Oral presentation

1) **Reina Tanaka**, Tsuguyuki Saito, Daisuke Ishii, Akira Isogai. “Length evaluation of nanocelluloses using shear viscosity measurement”, 247th ACS National Meeting, CELL-11, Dallas, March, 2014

2) **Reina Tanaka**, Hiromasa Hondo, Tsuguyuki Saito, Akira Isogai. “Influences of rigidity of cellulose nanofibrils on length evaluation using shear viscosity measurement”, IAWPS2015, 4CA2-12, Tokyo, March, 2015

3) **Reina Tanaka**, Tsuguyuki Saito, Akira Isogai. “Comprehensive investigation of rheological properties of nanocellulose dispersions”, Marcus Wallenberg Prize Young Researchers’ Challenge 2015, Stockholm, September, 2015

Poster presentation

1) **Reina Tanaka,** Tsuguyuki Saito, Daisuke Ishii, Akira Isogai. ”Rheological evaluation of lengths of cellulose nanofibrils prepared by TEMPO-mediated oxidation”, ICC2012, PB12, Sapporo, October, 2012

2) **Reina Tanaka**, Tsuguyuki Saito, Daisuke Ishii, Akira Isogai. “Determination of average lengths of TEMPO-oxidized cellulose nanofibrils (TOCNs) dispersed in water by rheological method”, 245th ACS National Meeting, CELL-50, New Orleans, April, 2013

3) **Reina Tanaka**, Hiromasa Hondo, Tsuguyuki Saito, Akira Isogai. “Length evaluation of rigid cellulose nanofibrils based on shear viscosity measurement”, Japanese-European Workshop “Cellulose and functional polysaccharides”, Berlin, October, 2014

4) **Reina Tanaka**, Hiromasa Hondo, Tsuguyuki Saito, Akira Isogai. “Length evaluation of rigid TEMPO-oxidized cellulose nanofibrils using shear viscosity measurement”, Recent advances in cellulose nanotechnology research, Trondheim, October, 2014

Domestic conference

Oral presentation

1) **田仲玲奈**、齋藤継之、磯貝明 「TEMPO/NaClO/$NaClO_2$系システムによる天然セルロースの酸化」、第62回日本木材学会年次大会、K16-06-1500 （札幌、2012年3月）

2) **田仲玲奈**、齋藤継之、石井大輔、磯貝明 「TEMPO 酸化セルロースナノフィブリル分散液のレオロジー特性と長さ評価」、平成 25 年度繊維学会年次大会、2H01 (東京、2013 年 6 月)

3) 平沖怜也、**田仲玲奈**、小野祐子、齋藤継之、磯貝明 「ナノセルロースの分子量及び長さ分布評価法の検討」、第82回紙パルプ研究発表会、21 （東京、2015年6月）

4) **田仲玲奈**、齋藤継之、本土広雅、磯貝明 「ナノセルロース分散液の流動特性：屈曲性とサイズが及ぼす影響」、セルロース学会第22回年次大会、K17 （札幌、2015年7月）

Poster presentation

1) **田仲玲奈**, 齋藤継之, 磯貝　明　「TEMPO/NaClO/$NaClO_2$系システムにより調製したセルロースナノフィブリルの解析」、セルロース学会第19回年次大会、P8 （名古屋、2012年7月）

2) **田仲玲奈**、齋藤継之、石井大輔、磯貝明　「ずり粘度測定による TEMPO 酸化セルロースナノフィブリルの長さ評価」、セルロース学会第 20 回年次大会、P73 (京都、2013 年 7 月)

3) 福住早花、**田仲玲奈**、磯貝明　「TEMPO 酸化セルロースナノフィブリルの分散安定性評価」、セルロース学会第 20 回年次大会、P76 (京都、2013 年 7 月)

4) **田仲玲奈**、齋藤継之、石井大輔、磯貝明　「ずり粘度測定による木材セルロースナノフィブリルの長さ評価」、第 44 回繊維学会夏季セミナー、P9　(桐生、2013 年 8 月)

5) **田仲玲奈**、齋藤継之、石井大輔、磯貝明　「ずり粘度測定による木材ナノセルロースの長さ測定」、レオロジー学会第 41 回年次大会、P1 (東京、2014 年 5 月)

6) **田仲玲奈**、齋藤継之、磯貝明　「セルロースナノフィブリルの剛直性とレオロジー特性の関係」セルロース学会第 21 回年次大会、P39 (鹿児島、2014 年 7 月)

Awards

1) 2013 年 7 月　セルロース学会第 20 回年次大会　ポスター賞

2) 2013 年 8 月　第 44 回繊維学会夏季セミナー　ポスター賞

Acknowledgement

本論文は、筆者が東京大学　大学院農学生命科学研究科　生物材料科学専攻　製紙科学研究室において行った研究を博士論文として編纂したものです。本研究を進めるにあたり、大変多くの方から御指導、御鞭撻、御協力を賜り、博士論文の完成に至りました。この場を借りて厚く御礼申し上げます。

指導教員の磯貝明教授に、心より厚く御礼申し上げます。大学での研究分野が異なる私を快く受け入れて下さり、それより五年間、日々御指導、御鞭撻を賜りました。木村実特任教授には、研究だけでなく、日常生活においても沢山の貴重なアドバイスを頂戴しました。齋藤継之准教授には、実際の実験を進めるにあたり、多くの御指導を頂戴しました。また、論文審査を賜りました井上正志教授（大阪大学大学院理学研究科）、岩田忠久教授（東京大学大学院農学生命科学研究科）、巽大輔准教授（九州大学大学院農学研究院）に、心より御礼申し上げます。

レオロジーの研究を進めるにあたり、多くの方々に御指導・御協力をいただきました。花王株式会社の植松武彦博士には、レオロジーの基礎を一から教えていただきました。東京大学高分子材料学研究室の石井大輔特任助教には、論文作成の際に多くの御協力をいただきました。株式会社アントンパール・ジャパンの平野尚也様、宮本圭介様、渡邉多津子様、佐藤翼様には、レオメーター導入時から測定手法の確立・改良に至るまで、大変お世話になりました。心より感謝申し上げます。

研究を進めるにあたり御協力下さいました製紙科学研究室の皆様に、御礼申し上げます。特に、竹内美由紀特任助教、福住早花博士、藤澤秀次博士には、具体的な実験の仕方を教えていただきました。Nathalie Lavoine 博士には、博士論文執筆の際に御助言いただきました。小野祐子氏には、SEC-MALLS 測定・構成糖分析等、多くの実験に於いて御協力いただきました。そして、普段から様々に支えていただいた現研究室メンバー各位にも感謝申し上げます。

博士課程二年次後期には、フィンランドの VTT Technical Research Centre of Finland にて、研究を進めました。受入をご許可下さいました研究エリア長の Pia Qvintus 氏、御指導下さいました Tekla Tammelin 博士と Tuomas Hänninen 博士に感謝いたします。また、実験にご協力くださいました Minna Hakalahti 氏、Kari Kammiovirta 氏、Marie Gestranius 氏、Katja Pettersson 氏、Vuokko Liukkonen 氏、そして High performance fibre products チームの皆様に感謝申し上げます。

透過型電子顕微鏡観察を行うにあたり、御指導下さいました東京大学生物素材科学研究室の木村聡元助教、小川悠博士（現フランス国立科学研究センター植物高分子研究所所属）、そして東京大学農学生命科学研究科技術基盤センターの石綱史子博士に御礼申し上げます。

最後に、博士課程への進学を快諾し、長い学生生活を支えてくれた家族に、心より感謝申し上げます。

田仲玲奈